UNIVERSIDADE DE SÃO PAULO
INSTITUTO DE FÍSICA DE SÃO CARLOS

FRANCIELE RENATA HENRIQUE

Optical nonlinearities in microstructures produced by ultrashort laser pulses

São Carlos
2021

FRANCIELE RENATA HENRIQUE

Optical nonlinearities in microstructures produced by ultrashort laser pulses

Thesis presented to the Graduate Program in Physics at the Instituto de Física de São Carlos, Universidade de São Paulo to obtain the degree of Doctor of Science.

Concentration area: Basic Physics

Advisor:
Prof. Dr. Cleber Renato Mendonça

Corrected Version
(original version available on the Program Unit)

São Carlos
2021

Henrique, Franciele Renata
Optical nonlinearities in microstructures produced by ultrashort laser pulses / Franciele Renata Henrique; advisor Cleber Renato Mendonça - corrected version -- São Carlos 2021.
100 p.

Thesis (Doctorate - Graduate Program in Basic Physics) -- Instituto de Física de São Carlos, Universidade de São Paulo - Brasil , 2021.

1. Direct laser writing. 2. Glass waveguides. 3. Nonlinear refractive index. 4. Gorilla Glass. 5. Eagle Glass. I. Mendonça, Cleber Renato, advisor. II. Title.

ACKNOWLEDGEMENTS

First of all, I would like to thank Prof. Cleber Renato Mendonça for mentoring me since my Master's. His dedication, creativity and problem-solving abilities have been a big inspiration to me. He always respected the search for my own identity as a researcher, encouraged my ideas and gave me space to grow. His support during tough times was crucial to get me here. I will be forever grateful for his confidence in me.

I am thankful for the advice and support from the Photonics Group professors: Lino, Tchê and Zílio. The many discussions and tips around the lab are greatly appreciated. To Lino and Tchê, I also thank their encouragement and excitement as Student Chapter supervisors.

I would like to thank the staff members of the Photonics Group, André Romero, Daniel and Marcão, for the technical support over the years. A special thanks to André for the always helpful presence in the lab and for teaching me so much about electronic instrumentation and coding.

Thanks to my fellow members of the Photonics Group for their support in the lab, feedback and always cheerful presence. From the old age: Nathália, Henry, Ruben, Nó, Emerson, Gustavo, Jonathas, Oriana, Juliana, Vinicius, PH, Otuka, Chico, Renato, Jessica, Sabrina, Kelly, Link and Lucas Sciuti. And from the new age: Lucas Konaka, Kauê, Dany, Rafael, André Pelosi, Filipe, Luís and Beatriz.

A special thanks to the Photonics Group members who were directly involved in the work presented here: Gustavo, Jonathas, Renato and PH. I am very grateful for the time they've spent helping me, the great moments in the lab and for all the fruitful discussions. I've learned so much from them.

Another special thanks to the members of the famous office 48, Nathália, Lucas and Henry, for their friendship, for bringing so much joy to stressful times and always being there for me when I needed, with advice, support, great humor, daily lab updates and peculiar Google searches.

I am deeply grateful for the opportunity to work with Prof. Dr. Rachel Grange during my research internship abroad at ETH Zurich. Her empathetic and generous leadership, and ability to gracefully manage a very talented and diverse team will forever be an example and inspiration to me. I am deeply grateful for the opportunities she gave me and the trust she put in me.

I am also deeply thankful to the Optical Nanomaterial members for their generosity, advice, support and friendship. My deepest gratitude to Marc, David, Fabian, Andreas, Wentao, Han, Sissi, Andrea, Romolo, Jollanda, Helena, Felix, Viola, Flavia, Artemis, Greg, Maria and Eric. Also a big thank you to Sara for her always efficient administrative work.

I would like to thank every member of the USP-IFSC OSA Student Chapter, past and present, for their restless dedication to projects, for supporting my ideas and for their friendship. It was truly amazing to work with them and be able to share my passion for science outreach and education. Hopefully we were able to make a difference in our community.

I am very grateful to the staff of the São Carlos Institute of Physics, specially Ricardo and Silvio for always being very helpful and efficient with the administrative issues. A special thanks to Neusa for the formatting corrections to this thesis.

Many thanks to the friends that I've made along the years that helped me during difficult times and made life brighter. Many of them were already cited here. A big thank you to my friend Gabriléo, the most knowledgeable person to ever live, yet the least wise. His intense personality and curious mind made me feel that I was never alone and kept me (almost) sane in troubled times.

I am very thankful to my parents, Márcia and Jucemar, who taught me that the most valuable things in life don't come easy; they take hard work and dedication. I am very grateful for all the sacrifice they've made so that I could get a good education. I know they always believed that the girl from Vila Ivete could accomplish great things.

I am deeply grateful to my partner in life, Ramon, for supporting me through the years and filling my life with love, care and joy. He always inspired me to be a better professional and person, to take care of myself and to fearlessly follow my dreams. With Ramon I've always had a place to call home and his support got me this far. I thank him for pushing me out of my comfort zone with his little big adventures. "Above us, only the front wheel", as he says.

Finally, I would like to express my deepest gratitude to the funding agencies that supported this work, allowing my exclusive dedication to it: CAPES, CNPq and FAPESP. **This PhD project was funded by grant #2015/22392-3, São Paulo Research Foundation (FAPESP). The research internship abroad was partially funded by grant #2019/13673-0, São Paulo Research Foundation (FAPESP).**

“Nothing in life is to be feared, it is only to be understood.
Now is the time to understand more, so that we may fear less.”
Marie Curie

ABSTRACT

HENRIQUE, F. R. **Optical nonlinearities in microstructures produced by ultrashort laser pulses**. 2021. 100 p. Thesis (Doctor in Science) - Instituto de Física de São Carlos, Universidade de São Paulo, São Carlos, 2021.

Direct laser writing (DLW) techniques with ultrashort laser pulses have been extensively used for materials processing. The nonlinear nature of the interaction between ultrashort pulses and matter confers high spatial localization to these techniques and allows the fabrication of compact devices in a single step with resolution in the micro/nanoscale. In this context, we can highlight the fabrication of microstructures in transparent materials, like polymers and glasses, since they allow for the realization of three-dimensional devices. For instance, high-quality direct laser-written waveguide circuits have been fabricated and applied to different fields, such as telecommunications, quantum optics, sensors, etc. As photonic circuits often guide high light intensity, the characterization of the nonlinear optical properties of these structures becomes essential to direct their technological application. In this work, we realized the third-order nonlinear optical characterization of fs-laser written waveguides, which were fabricated in special glasses: Corning® Gorilla® and Eagle XG® Glass. The nonlinear characterization was performed through the Dispersive-scan (D-scan) technique, the temporal analog of Z-scan that can be applied to waveguides. The results obtained for the Gorilla® Glass waveguides indicate that the fs-laser writing process is responsible for reducing the magnitude of the nonlinear refractive index, when compared to the bulk material. This effect depends on the writing parameters, and the reduction is stronger when higher energy pulses are employed. Raman spectroscopy measurements revealed that this reduction could be related to the generation of non-bridging oxygen hole centers (NBOHCs) upon fs-laser irradiation. The characterization of Eagle XG® Glass waveguides, fabricated in different writing regimes (repetitive and cumulative), confirms the reduction of the nonlinear refractive index in the repetitive regime. However, it also revealed that little to no modification occurs when the cumulative regime is used, meaning that heat accumulation can be responsible for erasing NBOHCs and restoring the optical nonlinearities. Our results bring new light to what is currently known about the light-matter interaction when ultrashort pulses are involved. Furthermore, they can help

tailor the application of fs-laser written glass waveguides, according to the desire for high or low optical nonlinearities.

Keywords: Direct laser writing. Glass waveguides. Nonlinear refractive index. Gorilla Glass. Eagle Glass.

RESUMO

HENRIQUE, F. R. **Não linearidades ópticas em microestruturas produzidas por pulsos ultracurtos**. 2021. 100 p. Tese (Doutorado em Ciências) - Instituto de Física de São Carlos, Universidade de São Paulo, São Carlos, 2021.

Técnicas de escrita direta a laser (DLW) com pulsos ultracurtos têm sido extensivamente usadas no processamento de materiais. A natureza não linear da interação entre pulsos ultracurtos e matéria confere alto resolução espacial a essas técnicas e permite a fabricação de dispositivos compactos num único passo e com resolução em escala micro/nanométrica. Nesse contexto, podemos destacar a fabricação de microestruturas em materiais transparentes, como polímeros e vidros, pois ela permite a realização de dispositivos tridimensionais. Circuitos fotônicos contendo guias de onda de alta qualidade e produzidas por escrita direta a laser têm sido fabricados e aplicados em diferentes campos, como telecomunicações, óptica quântica, sensores, etc. Como circuitos fotônicos frequentemente guiam altas intensidades luminosas, a caracterização das propriedades ópticas não lineares destas estruturas se torna essencial para a sua aplicação tecnológica. Nesse trabalho, realizamos a caracterização das propriedades não lineares de terceira ordem de guias de onda produzidas por escrita direta a laser com pulsos de femtossegundos em vidros especiais: *Corning*® *Gorilla*® e *Eagle XG*® *Glass*. A caracterização não linear foi realizada através da técnica de Varredura da Dispersão (D-scan), a análoga temporal da técnica de Z-scan que pode ser aplicada a guias de onda. Os resultados obtidos para as guias produzidas em *Gorilla*® *Glass* indicaram que o processo de escrita a laser foi responsável por reduzir a magnitude do índice de refração não linear quando comparado com o material *bulk*. Esse efeito depende dos parâmetros de escrita e a redução é maior quando pulsos de mais alta energia são empregados. Medidas de Espectroscopia Raman revelaram que essa redução pode estar associada à geração de centros com deficiência de átomos de oxigênio não ligante (*non-bridging oxygen hole centers* – NBOHCs) ao se irradiar o vidro com pulsos de femtossegundos. Os resultados obtidos para as guias em *Eagle XG*® *Glass*, fabricadas em diferentes regimes (repetitivo e cumulativo), confirmaram a redução do índice de refração não linear no regime repetitivo. No entanto, eles também revelaram que quase nenhuma modificação ocorre quando o regime

cumulativo é empregado, o que indica que o acúmulo de calor pode corrigir os defeitos NBOHCs e restaurar as propriedades não lineares do material. Nossos resultados trazem nova luz para o que se sabe atualmente sobre a interação de pulsos ultracurtos com a matéria. Além disso, eles podem dirigir a aplicação das guias produzidas em vidros por escrita direta a laser com pulsos de femtossegundos, de acordo com o desejo por altas ou baixas não linearidades ópticas.

Palavras-chave: Escrita direta a laser. Guias de onda em vidros. Índice de refração não linear. Gorilla Glass. Eagle Glass.

LIST OF FIGURES

LIST OF ABREVIATIONS AND ACRONYMS

2PA	Two-Photon Absorption
2PP	Two-Photon Polymerization
BO	Bridging Oxygen
DLW	Direct Laser Writing
FROG	Frequency Resolved Optical Gating
FSPC	Femtosecond Pulse Compressor
FT	Fourier Transform
GDD	Group Delay Dispersion
GVD	Group Velocity Dispersion
NBO	Non-Bridging Oxygen
NBOHC	Non-Bridging Oxygen Hole Center

LIST OF SYMBOLS

$\mathcal{E}$	electric field
P	polarization
ϵ_0	vacuum permittivity
$\chi^{(n)}$	*n*-order electric susceptibility
I	light intensity
$\tilde{n}$	complex refractive index
n	real part of the complex refractive index
n_0	linear refractive index
n_2	nonlinear refractive index associated to $\chi^{(3)}$
κ	imaginary part of the complex refractive index
α	absorption coefficient
α_0	linear absorption coefficient
β	nonlinear absorption coefficient associated to $\chi^{(3)}$
k	wave vector amplitude
τ	temporal width of the light pulse
L	length of the nonlinear medium
ω	instantaneous frequency
$\delta\omega$	frequency shift
φ	temporal phase of the ultrashort pulse
ϕ	spectral phase of the ultrashort pulse
τ_{gr}	group delay
λ	wavelength
σ	spectral width (standard deviation)
$\phi^{(2)}$	second-order dispersion or GDD
β_2	group velocity dispersion or GVD
γ	nonlinear coefficient for optical fibers
A_{eff}	effective mode area
E	pulse energy
μ	attenuation coefficient
λ_0	central wavelength
$\Delta\lambda$	bandwidth (FWHM)

d	mode diameter
N	number of pulses per spot
v	laser writing speed
f	laser repetition rate
w_0	beam waist

CONTENTS

1 INTRODUCTION

Ultrashort laser pulses are the denomination given to light pulses with duration in the order of picoseconds, femtoseconds, or less. Commonly generated in mode-locked oscillators, for example, ultrashort pulses are characterized by their broad spectrum and high peak intensity.[1–3] In the past decades, they have become an important tool to study the dynamics of molecular and atomic systems at short time scales, prompting the field of femtochemistry.[4] Furthermore, their high peak intensity has allowed advances in the fields of nonlinear optics[5] and materials processing,[6-7] especially after the development of chirped pulse amplification.[8]

In recent years, direct laser writing (DLW) techniques that use ultrashort laser pulses have gained a lot of attention as important tools for the fabrication of devices in micro/nanoscale,[6-7] since they allow for quick production of compact devices in a single step process. DLW with ultrashort laser pulses has become an interesting alternative to other micro/nanofabrication techniques, like UV or e-beam lithography,[9] which require cleanroom facilities and several fabrication steps. In DLW techniques, structures are fabricated by either localized removal of material or modification of its physical properties, and they can be applied to absorptive or transparent materials. The interaction between ultrashort laser pulses and matter is often mediated by nonlinear processes, which grants high resolution to the writing techniques, since nonlinear excitation is confined to the focal volume.[10] In this context, microfabrication in transparent materials, which is often the case of polymers and glasses, is particularly interesting, because excitation can be performed inside the volume of the material, allowing for the production of three-dimensional structures and complex devices.[11]

In polymeric materials, DLW is used to produce microstructures by two-photon polymerization (2PP).[12-13] The beam of an ultrashort pulses laser is scanned through the volume of a liquid photoresist, promoting localized polymerization in the focal volume and allowing the fabrication of three-dimensional micro/nanostructures. The unpolymerized material is then removed with the proper developer, leaving only the fabricated structures attached to the substrate. This technique allows for the fabrication of complex structures with high resolution,[14–16] being explored for microfluidics,[17] mechanical microdevices,[18] photonic structures and biological applications, like micro needles for drug delivery and scaffolds for cell growth.[19]

When it comes to photonic applications, structures like microresonators, interferometers and waveguides,[20–22] microlenses,[23] fiber-to-chip couplers,[24] photonic crystals,[25] among others have been fabricated. Another great advantage of DLW in polymeric materials is the ease of incorporation of different doping materials to the polymeric matrices, like organic dyes,[26–28] metal nanoparticles and quantum dots,[29] graphene-based materials,[30-31] etc. This feature allows the modification of the material physical properties, allowing for the fabrication of devices with specific properties. In recent years, a great deal of attention has been given to the fabrication of polymeric devices with interesting linear optical properties, such as fluorescent structures to be used as light sources in microscale[28,32] or microlasers,[27] birefringent structures,[33] etc. However, studies related to nonlinear optical properties of polymeric micro/nanostructures fabricated by DLW are still scarce.

Just like polymers, glassy materials have great prominence in the Photonics field. They can be fabricated in different shapes and sizes, from nanoparticles and thin films, to glass slides with dimensions on the meter scale and optical fibers with kilometers of length.[34-35] Furthermore, their physical properties can be tailored by modifying the glass matrix composition, by the addition of dopants,[36] and by thermal/chemical treatments.[37] For instance, glasses with interesting features like photoluminescence,[38-39] magneto-optical effect[40] and high nonlinear optical properties[41-42] have already been realized. The DLW technique with ultrashort laser pulses has been vastly applied to the fabrication of photonic devices in glassy materials.[43] Waveguides with interesting features, like good guided mode quality, low propagation losses and length greater than ten centimeters have been demonstrated.[44] This way, DLW allows for the fabrication of complex structures inside bulk glass, like directional couplers,[45-46] Mach-Zender interferometers,[47-48] wavelength demultiplexers,[49] resonators,[50-51] fiber Bragg gratings,[52-53] etc. Active fs-laser written devices in glass have already been demonstrated, showing tunable lasing properties and even mode-locking.[54-55] This way, in recent years, the application of photonic devices written by ultrashort laser pulses has been prompted in different fields, such as quantum optics,[56] communications,[43] microfluidics,[57] sensing,[58] among others. In Fig. 1.1 we can observe some examples of these fs-laser written waveguide devices.

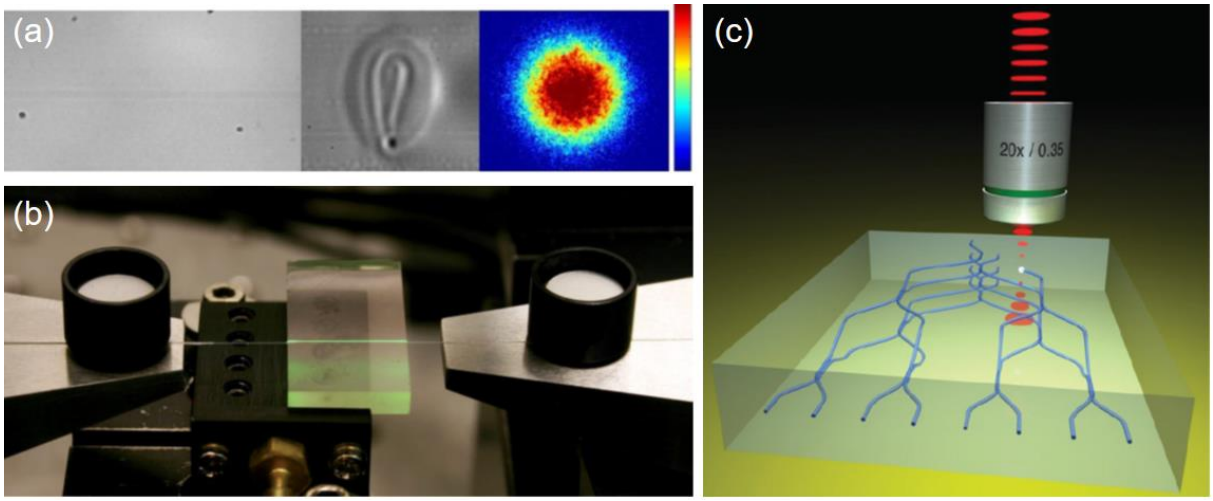

Figure 1.1 - (a) Top view, cross-section and mode profile of a fs-laser written waveguide in Gorilla® Glass. (b) Active fs-laser written device fabricated in Kigre QX glass, presenting green fluorescence along a waveguide amplifier. (c) Conceptual illustration of 3D waveguide circuits written in the volume of glass.
Source: (a) Adapted from LAPOINTE *et al*.;[44] (b) AMS *et al*.;[55] (c) MEANY *et al*.[56]

With the advent of Integrated Photonics, nonlinear optical effects can be efficiently induced with moderate power levels via on-chip platforms.[59] This is possible due to strong light confinement in small areas, often through long distances, generating high intensity and long interaction length. This way, the nonlinear characterization of fs-laser written structures becomes crucial to their technological application in integrated devices, especially since the interaction of ultrashort pulses with matter is still not completely understood and can deeply affect materials chemical structure,[60] possibly changing their nonlinear properties. A great deal of attention has been given recently to modeling the linear refractive index changes in glasses upon fs-laser irradiation.[61] However, similar studies related to nonlinear properties are still scarce. This way, in this thesis we aim to answer a few questions: “Does fs-laser irradiation change the nonlinear optical properties of a material?”, “If yes, how are these changes affected by laser writing parameters?”, and “What are the structural modifications that lead to changes in nonlinear properties?”.

In order to answer these questions, we performed the third-order nonlinear characterization of fs-laser written waveguides, fabricated in Corning® special display glasses: Gorilla® and Eagle XG® Glass. The nonlinear characterization of structures in microscale is a challenge on its own, since it cannot be performed with standard techniques for bulk materials, like the Z-scan technique.[62] It is usually performed by complex pump-probe and interferometry techniques.[63–65] This way, we initially implemented, for the first time in our lab at the Photonics Group, the

Dispersive-scan technique (D-scan),[66–68] which is known as the temporal analog to Z-scan that can be applied to waveguides. When compared to other techniques, D-scan has the advantage of using only a single beam, and both the refractive and absorptive nonlinearities can be studied with the same experimental apparatus. In Chapter 2, we present the theoretical basis needed to understand the D-scan technique and related nonlinear phenomena. In Chapter 3, we present the D-scan technique itself and our instrumental developments. In Chapter 4, we present the studies related to the characterization of Gorilla® Glass waveguides and, finally, in Chapter 5, we present the studies performed in Eagle XG® Glass waveguides.

We believe that the answers to the questions that we explore in this thesis can help to further understand the mechanisms of light-mater interaction during DLW, as well as tailor the application of fs-laser written structures. For instance, waveguides with high refractive nonlinearities can be interesting for applications in optical switching,[69] supercontinuum generation,[70] and frequency combs.[71] Waveguides with high absorptive nonlinearities can be interesting for active applications, like lasing.[55] On the other hand, waveguides with low refractive and absorptive nonlinearities are interesting for telecommunications, where these effects are usually undesirable, because they can add noise and losses to the guided signal.

2 THEORETICAL BASIS

2.1 Introduction to Nonlinear Optics

Nonlinear Optics is the study of phenomena that occur when a material, under a high intensity electric field, responds nonlinearly to this field.[5] Typically, these phenomena manifest when the applied electric field reaches intensity comparable to the interatomic electric field, that is of the order of $10^8\ V/m$. This way, it was only after the advent of laser by Maiman in 1960[72] that these high intensities could be reached, and the field of Nonlinear Optics started to develop. Nowadays, ultrashort laser pulses, which have temporal width equal to or below picoseconds, are the main excitation sources used to observe nonlinear phenomena, due to their high peak intensities. Among the many nonlinear optical effects, we can highlight: second harmonic generation,[73] Kerr Effect,[74-75] two-photon absorption (2PA),[76-77] etc.

Considering a medium that responds instantly to an applied electric field ($\mathcal{E}(t)$), its polarization ($P(t)$) can be written as

$$P(t) = \epsilon_0 \chi \mathcal{E}(t), \tag{2.1}$$

where ϵ_0 is the vacuum permittivity and χ is the medium susceptibility. However, this expression is just a particular case, since the medium polarization can be expanded in a power series of the electric field as

$$\begin{aligned} P(t) = & \ \epsilon_0\left[\chi^{(1)}\mathcal{E}(t) + \chi^{(2)}\mathcal{E}^2(t) + \chi^{(3)}\mathcal{E}^3(t) + \cdots\right] \\ & \equiv P^{(1)}(t) + P^{(2)}(t) + P^{(3)}(t) + \cdots, \end{aligned} \tag{2.2}$$

where $\chi^{(1)}$ is the linear susceptibility and $\chi^{(2)}$ and $\chi^{(3)}$ are the second and third-order susceptibilities, respectively.

For the case of centrosymmetric media, those that present inversion symmetry, the susceptibilities of even-order are equal to zero. This way, the polarization expression becomes

$$P(t) = \epsilon_0\left[\chi^{(1)}\mathcal{E}(t) + \chi^{(3)}\mathcal{E}^3(t) + \cdots\right]$$

$$\cong \epsilon_0\left[\chi^{(1)} + \chi^{(3)}I\right]\mathcal{E}(t), \tag{2.3}$$

where I is the intensity of the electric field that is equal to $\mathcal{E}(t)^2$. Here we can define the effective susceptibility of the medium

$$\chi_{ef} = \chi^{(1)} + \chi^{(3)}I. \tag{2.4}$$

The complex refractive index of the medium can then be written as

$$\tilde{n} = \sqrt{1 + \chi_{ef}} = \sqrt{1 + (\chi^{(1)} + \chi^{(3)}I)}. \tag{2.5}$$

For media with low optical density, the square root can be expanded and simplified to

$$\tilde{n} \approx 1 + \frac{1}{2}\left(\chi^{(1)} + \chi^{(3)}I\right) = n + i\kappa\,. \tag{2.6}$$

Taking the real part of this expression, we have the effective refractive index

$$\begin{aligned} n &= 1 + \frac{1}{2}Re\left[\chi^{(1)}\right] + \frac{1}{2}Re\left[\chi^{(3)}\right]I \\ &= n_0 + n_2 I, \end{aligned} \tag{2.7}$$

where n_0 is the linear refractive index and n_2 is the nonlinear refractive index associated to $\chi^{(3)}$. n_2 is responsible for nonlinear refraction effects, like self-focusing and self-phase modulation, i. e. the Optical Kerr Effect.[74-75]

Now taking the imaginary part of the complex refractive index, we have

$$\kappa = \frac{1}{2}Im\left[\chi^{(1)}\right] + \frac{1}{2}Im\left[\chi^{(3)}\right]I. \tag{2.8}$$

κ is the extinction coefficient that is proportional to the absorption coefficient

$$\alpha = \alpha_0 + \beta I \,, \tag{2.9}$$

where α_0 is the linear absorption coefficient and β is the nonlinear absorption coefficient associated to $\chi^{(3)}$, that describes the phenomenon of two-photon absorption.[76-77]

2.2 The Optical Kerr Effect

The dependence of the refractive index of a medium with the applied electric field, as described in Eq. 2.7, is known as The Optical Kerr Effect[74-75] or nonlinear refraction. Between the consequences of this effect, we can highlight self-focusing and self-phase modulation phenomena.

The self-focusing phenomenon is related to the spatial modulation of the refractive index of a medium. If, for instance, a high intensity laser with a Gaussian transversal profile is shone into a nonlinear medium with positive n_2, the effective refractive index is higher where the beam intensity is higher, that is in the central region of the Gaussian profile. This effect leads to the self-focusing of the beam, phenomenon also known as Kerr lens.

Similar to the self-focusing effect, self-phase modulation happens when there is a modulation of the refractive index but in the time domain. If a high intensity laser pulse propagates through a medium, the light intensity in a point in space first increases and then decreases as time passes. This way, the Optical Kerr Effect induces a time-dependent refractive index that can be written as

$$n(t) = n_0 + n_2 I(t). \tag{2.10}$$

Now we consider a light pulse propagating in the x direction and defined by the electric field expression:

$$\mathcal{E}(x,t) = \mathcal{E}_0 \exp(i(\omega_0 t - kx)), \tag{2.10}$$

where $\mathcal{E}_0$ is the amplitude of the electric field, ω_0 is the pulse frequency and k is the wave vector. This pulse presents a Gaussian intensity profile in the time domain with width τ and given by

$$I(t) = I_0 \exp\left(-\frac{t^2}{\tau^2}\right). \tag{2.11}$$

The wave vector k is defined by

$$k = \frac{\omega_0}{c} n(t), \tag{2.12}$$

where $n(t)$ is the time-varying refractive index.

After propagating through a medium for a distance L, the pulse phase can be written as

$$\Phi(t) = \omega_0 t - kL = \omega_0 t - \frac{\omega_0}{c} n(t) L. \tag{2.13}$$

When the nonlinear effect takes place we have

$$\Phi(t) = \omega_o t - \frac{\omega_0}{c} n_0 L - \frac{\omega_0}{c} n_2 L \times I(t). \tag{2.14}$$

The pulse instantaneous frequency is defined by the derivative in time of the phase

$$\omega(t) = \frac{d\Phi(t)}{dt} = \omega_0 - \frac{\omega_0}{c} n_2 L \frac{dI(t)}{dt}. \tag{2.15}$$

This way, after propagation through the nonlinear medium, the pulse acquires a time-dependent frequency shift given by

$$\delta\omega(t) = -\frac{\omega_0}{c} n_2 L \frac{dI(t)}{dt}, \tag{2.16}$$

which leads to the generation of new frequencies in the pulse spectrum. For a material with positive n_2, the instantaneous frequency shift is proportional to $-\frac{dI(t)}{dt}$. This means that, when the pulse presents a Gaussian profile in the time domain, as illustrated in Fig. 2.1 (a), while the pulse intensity increases $\left(\frac{dI(t)}{dt} > 0\right)$ there is the generation of new frequencies lower than ω_0. On the other hand, when the pulse intensity decreases $\left(\frac{dI(t)}{dt} < 0\right)$ there is the generation of frequencies higher than ω_0. This effect can be observed in Fig. 2.1 (b), where the Gaussian pulse frequency shift is represented for a material with positive n_2. We can conclude that, in this situation, the self-phase modulation effect leads to broadening of the pulse spectrum as it propagates through the nonlinear medium, since there is the generation of new frequencies lower and higher than ω_0.

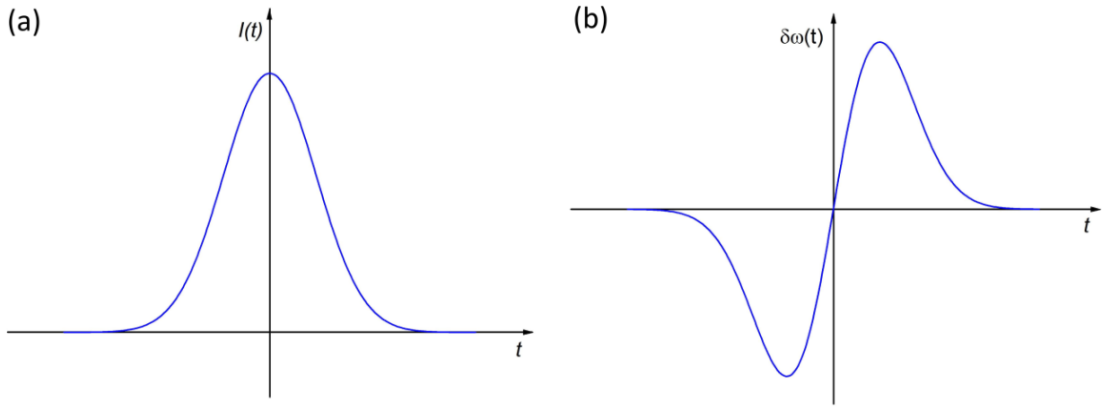

Figure 2.1 - (a) Temporal intensity profile of a Gaussian pulse. (b) Variation of the pulse instantaneous frequency in time for a material of positive n_2.
Source: By the author

2.3 Ultrashort laser pulses

As previously mentioned, ultrashort laser pulses are defined as electromagnetic pulses that present temporal width in the order of or inferior to picoseconds.[78] These pulses can be generated, for instance, by mode-locked oscillators, in which pulses with femtosecond duration can be realized. Ultrashort pulses are characterized by their large spectral bandwidth and high peak intensity, making them ideal for the study of nonlinear optical phenomena. In Fig. 2.2 we can

observe the representation of the electric field (blue line) of a femtosecond laser pulse with Gaussian envelope profile (red line).

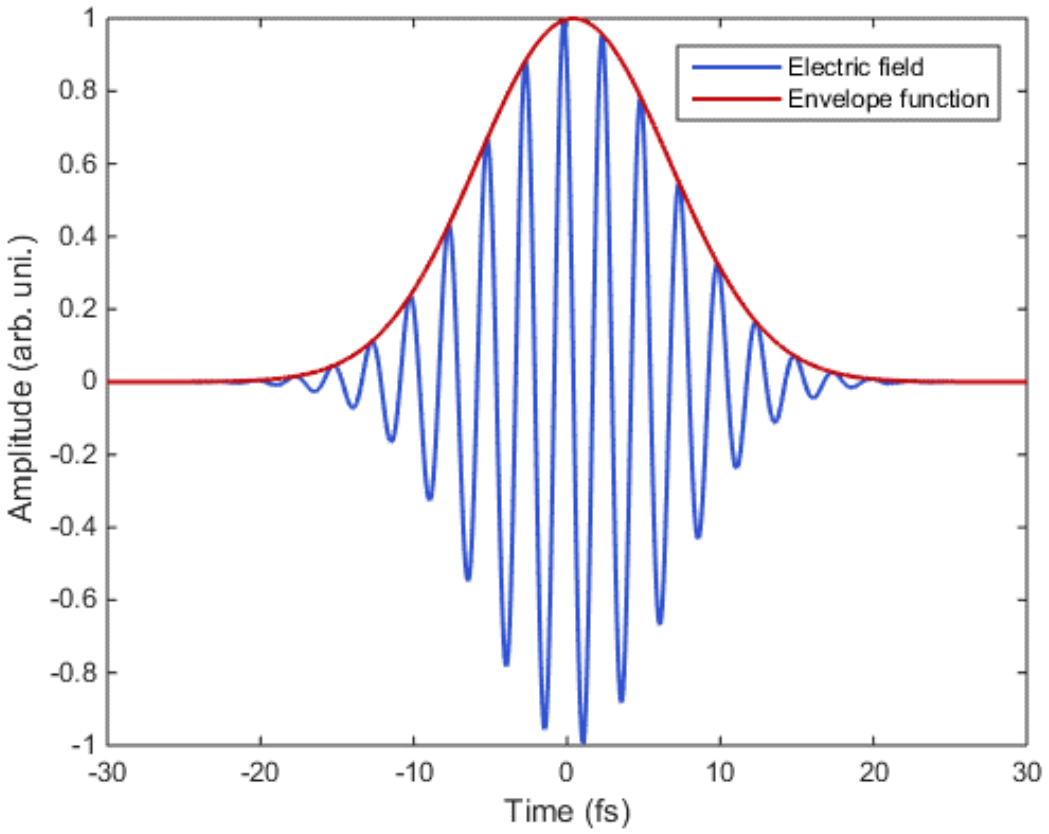

Figure 2.2 - Representation of the electric field (blue line) of an ultrashort laser pulse and its envelope function (red line).
Source: By the author

2.3.1 Dispersion in ultrashort laser pulses

The electric field of an ultrashort pulse can be defined by the expression

$$\mathcal{E}(t) = \frac{1}{2}\sqrt{I(t)}\exp[i(\omega_0 t - \varphi(t))] + c.c., \tag{2.17}$$

where $I(t)$ is the pulse intensity profile, ω_0 is its central frequency and $\varphi(t)$ is the temporal phase. In frequency domain, the pulse is described by the Fourier Transform

$$\hat{\mathcal{E}}(\omega) = \int_{-\infty}^{\infty} \mathcal{E}(t) \exp(-i\omega t)\, dt \;\equiv\; \sqrt{S(\omega)} \exp(-i\phi(\omega)), \tag{2.18}$$

where $S(\omega)$ represents the spectral distribution and $\phi\,(\omega)$ is its spectral phase.

The temporal phase $\varphi(t)$ of an ultrashort laser pulse carries information about frequency vs. time. This way, the instantaneous frequency can be defined as

$$\omega_{inst}(t) \equiv \omega_0 - \frac{d\varphi(t)}{dt}. \tag{2.19}$$

Similarly, the spectral phase $\phi(\omega)$ carries information about time vs. frequency and the group delay is defined as

$$\tau_{gr}(\omega) = \frac{d\phi(\omega)}{d\omega}. \tag{2.20}$$

The phase acquired by a pulse as it propagates through a dispersive medium can be expressed as a Taylor expansion around the central frequency ω_0

$$\phi(\omega) = \phi(\omega_0) + \left.\frac{d\phi}{d\omega}\right|_{\omega=\omega_0} \times (\omega - \omega_0) + \left.\frac{1}{2}\frac{d^2\phi}{d\omega^2}\right|_{\omega=\omega_0} \times (\omega - \omega_0)^2 + \\ + \left.\frac{1}{6}\frac{d^3\phi}{d\omega^3}\right|_{\omega=\omega_0} \times (\omega - \omega_0)^3 + \cdots \tag{2.21}$$

This way, the group delay can also be written as

$$\tau_{gr} = \frac{d\phi(\omega)}{d\omega} = \left.\frac{d\phi}{d\omega}\right|_{\omega=\omega_0} + \left.\frac{d^2\phi}{d\omega^2}\right|_{\omega=\omega_0} \times (\omega - \omega_0) + \\ + \left.\frac{1}{2}\frac{d^3\phi}{d\omega^3}\right|_{\omega=\omega_0} \times (\omega - \omega_0)^2 + \cdots \tag{2.22}$$

The first term of Eq. 2.23 represents a temporal delay in pulse propagation. The second term represents a linear variation of the group delay with frequency,

known as linear chirp. The coefficient $\frac{d^2\phi}{d\omega^2}\Big|_{\omega=\omega_0}$ is known as second-order dispersion or group delay dispersion (GDD), and can be represented as $\phi^{(2)}$. When, for instance, the coefficient $\frac{d^2\phi}{d\omega^2}\Big|_{\omega=\omega_0}$ is positive, lower frequencies acquire a lower delay than higher frequencies. This results in a temporal distribution of frequencies, leading to the temporal broadening of the ultrashort pulse.

A pulse that presents a constant phase across all its frequency components has the minimum duration possible for its spectral bandwidth; it is called Bandwidth-limited or Fourier-Transform-limited (FT-limited). In Fig. 2.3 (a), we can observe the temporal profile of a FT-limited pulse, showing the electric field oscillation (a - blue line) and their envelope function (a – black line). In Fig. 2.3 (b), we can observe its spectral profile (b – black line) and constant spectral phase $\phi(\omega)$ (b – red line). We can also observe the electric field oscillation for a positively (c) and negatively (e) chirped pulse, showing how the oscillation frequency increases and decreases over time, respectively. We can also observe how that the introduction of chirp leads to the temporal broadening of the pulse. In Fig. 2.3 (d) and (f), we can see how this frequency sweep, i.e., a linear group delay, translates to a parabolic spectral phase with positive and negative concavity, respectively.

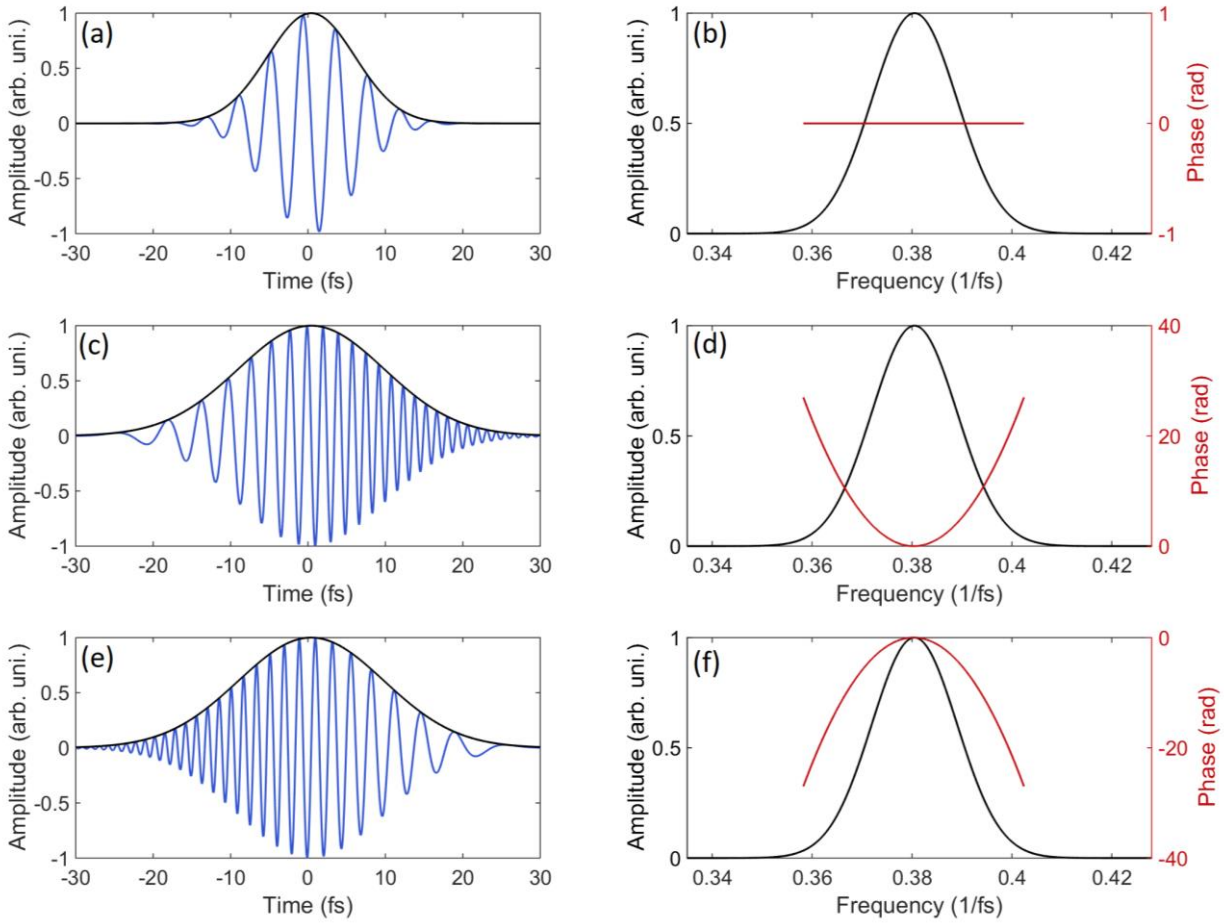

Figure 2.3 - Temporal profile of an ultrashort pulse showing the electric field (blue line - left) and the envelope function (black line - left), and their frequency spectrum (black line - right) and spectral phase (red line – right) for the case of a FT-limited (*a* and *b*), positively chirped (*c* and *d*) and negatively chirped pulse (*e* and *f*).
Source: By the author

2.3.2 Self-phase modulation and dispersion in ultrashort laser pulses

As discussed in Section 2.2, the Optical Kerr Effect leads to the generation of new frequencies in the spectrum of an ultrashort laser pulse as it propagates through a nonlinear material. Besides that, for a material of positive n_2 for example, the instantaneous frequency shift $\delta\omega$ is proportional to the derivative expression: $-\frac{dI(t)}{dt}$. As we can observe in Fig. 2.1, for a pulse with a Gaussian temporal profile, frequencies higher and lower than ω_0 will be generated, according to the derivative of each slope of the Gaussian curve. This phenomenon leads to a broadening effect in the spectrum of the ultrashort laser pulse. In the discussion presented in Section 2.2, we considered a FT-limited pulse, i.e. a pulse that does not present group delay dispersion, in which we can consider that all frequencies are equally distributed in

time and the pulse can be described by its central frequency ω_0. A similar discussion can be done for pulses with group delay dispersion or linear chirp.

In Fig. 2.4 (a) and Fig. 2.5 (a) we can observe the representation of the electric field $\mathcal{E}(t)$ (colored line) and its Gaussian envelope $\sqrt{I(t)}$ (black line) of an ultrashort pulse with positive and negative chirp, respectively. When n_2 is positive, frequency components that are in the front slope of the Gaussian envelope, i.e. where the derivative $\frac{dI(t)}{dt}$ is positive, will be shifted to lower frequencies after self-phase modulation, as demonstrated in Eq. 2.16. On the other hand, frequency components that are in the back slope of the Gaussian envelope, i.e. where the derivative $\frac{dI(t)}{dt}$ is negative, will be shifted to higher frequencies.

In the case of a positively chirped pulse, lower frequencies are ahead of higher frequencies in time. This way, for a positively chirped pulse, self-phase modulation leads to the shift of lower frequency components to even lower frequencies, and the higher frequency components are shifted to even higher ones. This means that the ultrashort pulse spectrum will be broadened after crossing the nonlinear medium, just as FT-limited pulses. For energy conservation reasons, the pulse spectral broadening is followed by the reduction of the peak intensity, as showed in Fig. 2.4 (b).

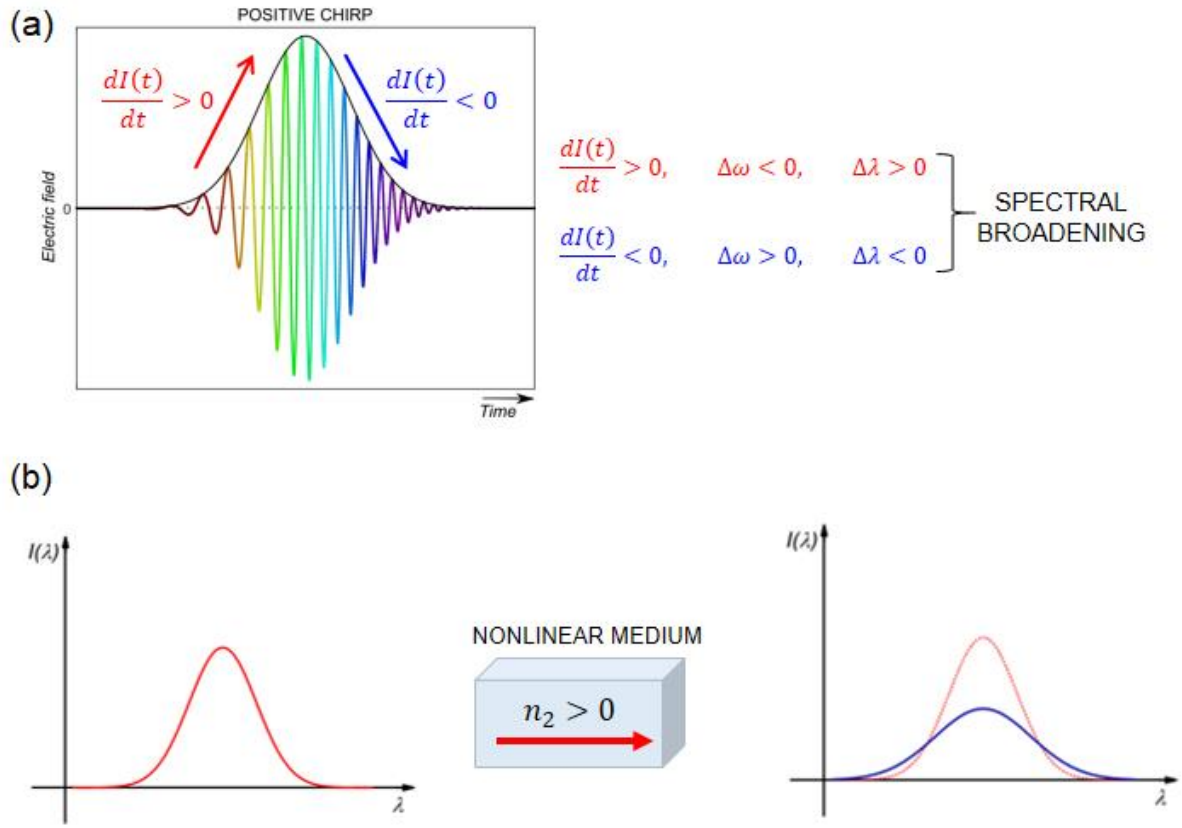

Figure 2.4 - (a) Electric field amplitude and Gaussian envelope of a positively chirped pulse, showing how low frequency components are red-shifted and high frequency components are blue-shifted due to self-phase modulation in a medium with positive n_2. (b) Scheme of the spectral broadening phenomenon in a positively chirped pulse, showing how the spectrum $I(\lambda)$ is broadened after passing through the nonlinear medium.
Source: By the author

For negatively chirped pulses, higher frequencies are ahead of lower frequencies in time. This way, self-phase modulation leads to a negative shift in higher frequency components, as well as a positive shift for lower frequency components. This means that new frequency generation will occur mainly in the central region of the spectrum, leading to its compression. The spectral compression phenomenon is followed by an increase in the peak intensity. It is important to notice that, when the pulse second-order dispersion is too high, regardless if it is positively or negatively chirped, the pulse becomes too broad in time and, when it crosses the nonlinear material, its energy might not be enough to cause self-phase modulation, so no spectral modifications would be observed.

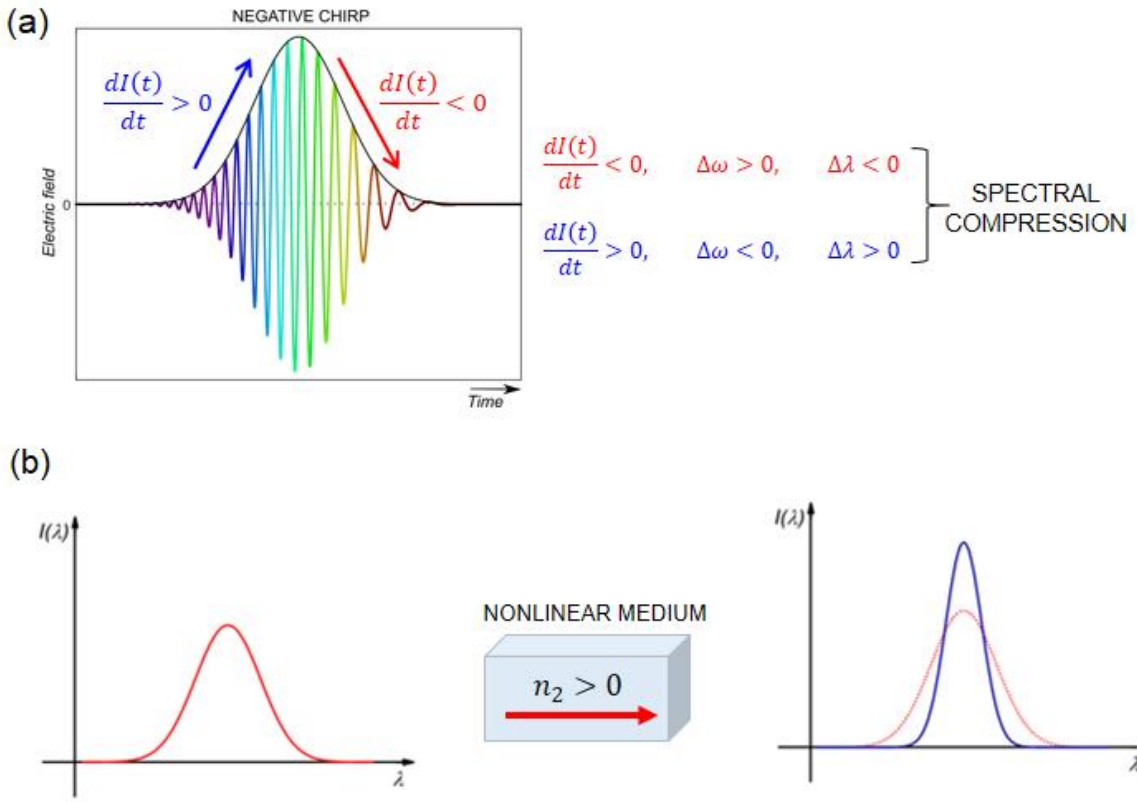

Figure 2.5 - Electric field amplitude and Gaussian envelope of a negatively chirped pulse, showing how low frequency components are blue-shifted and high frequency components are red-shifted due to self-phase modulation in a medium with positive $\boldsymbol{n_2}$. (b) Scheme of the spectral compression phenomenon in a negatively chirped pulse, showing how the spectrum $\boldsymbol{I(\lambda)}$ is compressed after passing through the nonlinear medium.
Source: By the author

In the case of a nonlinear medium with negative n_2, the process is similar to the previously described, but self-phase modulation leads to spectral broadening for negatively chirped pulses and spectral compression for positively chirped pulses. FT-limited pulses are compressed as well.

3 THE DISPERSIVE-SCAN TECHNIQUE

3.1 Introduction

Among the different techniques available to evaluate third-order optical nonlinearities, the Z-scan technique[62] is one of the most popular, due to its high sensitivity and ability to characterize both the nonlinear refraction and nonlinear absorption of the studied material. The nonlinear refractive index n_2 is determined by the closed-aperture form of the technique. The investigated sample is irradiated by a focused beam and the nonlinear refraction acts as an additional lens, changing how the beam is transmitted through an aperture placed at the far-field. The sample position is scanned through the focal length, in *z* direction, and the power transmitted through the aperture is recorded. Since the focusing power of the additional lens depends on the nonlinear refractive index, the n_2 magnitude is determined by the *z*-dependent transmitted signal. This way, the Z-scan technique is mainly used for the characterization of macroscopic samples, since the variation of intensity at the sample is performed by scanning it around the focus point for several millimeters or more. Other techniques can be used to investigate the nonlinearities in structures of microscopic dimensions, like interferometry methods and pump-probe.[63–65] Each one of these techniques has advantages and disadvantages, associated with their intrinsic experimental challenges and sensitivity.

An alternative for the study of optical nonlinearities in micrometric systems is the Dispersive-scan technique (D-scan)[66–68], the time-analogue of Z-scan, in which the variation of intensity at the sample is performed by introducing dispersion to the probing pulsed laser beam. The value of n_2 is determined through the spectral modifications due to self-phase modulation, according to the input dispersion. In this technique, the optical nonlinearities of microscopic structures, waveguides and optical fibers can be investigated, since the sample remains fixed, and it has the advantage of requiring only a single beam. The D-scan technique was initially proposed by Louradour *et al.*[66] in 1999. In their experimental setup, a Ti:Sapphire laser emitting femtosecond pulses is used. The beam passes through a dispersive delay line before reaching the sample. The dispersive line is composed of two movable prisms and mirrors. The dispersion of the femtosecond pulses is varied by moving the prims in such a way that the optical path through them is varied without

deflecting the beam. When passing through the dispersive line, the pulses acquire a second-order spectral phase, which has the same signal as the introduced dispersion. In the case of an optical fiber, the beam is then coupled to the fiber by an objective lens. The transmitted signal is collected by another objective lens. The output spectrum is then analyzed by an OSA (Optical Spectrum Analyzer). The evolution of the spectrum of the output signal, when the input beam dispersion is varied from negative to positive values, provides a way to measure the third-order complex susceptibility of the investigated material.

3.2 Working principle

In the Dispersive-scan technique, the second-order dispersion of incident ultrashort pulses is varied from negative to positive values, and the evolution of the spectral width and/or peak intensity is evaluated after crossing a nonlinear medium. In Fig. 3.1, we can observe typical D-scan curves for the spectral width σ (Fig. 3.1 - top) and peak intensity I_{peak} (Fig 3.1 – bottom).These curves were simulated with a code in *LabVIEW*, using the add-on *Lab2 – A virtual femtosecond laser lab*.[79] In the case of a material with positive nonlinear refractive index, when the dispersion of the incident beam is scanned from negative to positive values, the output spectrum width passes through a plateau, where self-phase modulation cannot be observed, followed by a valley that corresponds to spectral compression, then a spectral broadening peak, and finally it returns to the plateau, as observed in Fig. 3.1 (top). In Fig 3.1 (bottom), we can observe the D-scan curve for spectral peak intensity that behaves in a mirrored way to the width curve and there is a peak for spectral compression and a valley for spectral broadening. The Dispersive-scan curves behave very similarly to the Z-scan signature curves.[62]

When the nonlinear refractive index n_2 is negative, the curves represented in Fig. 3.1 are also mirrored; that is, when dispersion is varied from negative to positive values, initially spectral broadening is observed, followed by spectral compression. This way, the sign of the nonlinearity can be determined by the shape of the D-scan curve.

The D-scan curve asymmetry that can be observed in Fig. 3.1, is explained by the resulting effect of linear dispersion and the acquired nonlinear phase. When the input dispersion and the nonlinear phase have opposite signs, as in the case of

negative dispersion and positive n_2, the acquired positive phase adds to the negative input parabolic phase, reducing the magnitude of the pulse dispersion, and thus suppressing the compression effect. In the D-scan curve, this means that the spectral compression valley will be less prominent than the spectral broadening peak.

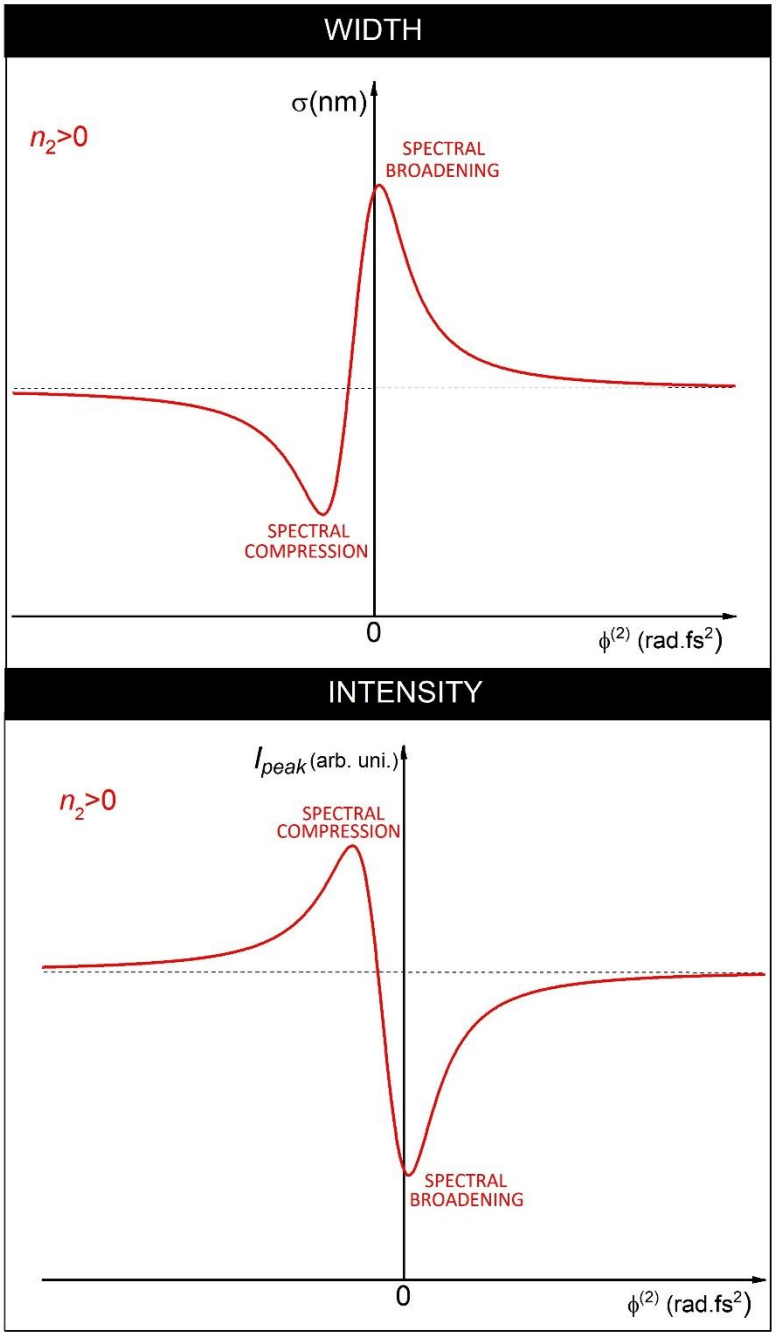

Figure 3.1 - Simulation of typical D-scan curves for the spectral width (top) and peak intensity (bottom) as function of the second-order dispersion $\boldsymbol{\phi^{(2)}}$.
Source: By the author

The magnitude of the nonlinear refractive index n_2 can be obtained through the fit of the D-scan curve and it is proportional to the peak-to-valley amplitude $\Delta\sigma_{pv}$ or ΔI_{pv}. Lopez-Lago *et al*.[67] found a relation between the amplitude ΔI_{pv} and the nonlinear phase $\Delta\phi_{NL}$ acquired through self-phase modulation when an ultrashort pulse propagates in a waveguide:

$$\Delta I_{pv} = 0.418\,\Delta\phi_{NL} = 0.418\frac{2\pi}{\lambda}n_2 IL, \tag{3.1}$$

where λ is the central wavelength of the laser spectral band, I is the light intensity coupled to the waveguide and L its length. It is important to note that the authors obtained this expression through numerical simulations, without taking into account the material dispersion. Nevertheless, this expression can be useful for the estimation of the nonlinear refractive index of samples with low dispersion, like common glasses.

3.3 Experimental methods

3.3.1 Dispersive-scan setup

A simplified scheme of the experimental apparatus that was implemented for the Dispersive-scan technique is shown in Fig. 3.2. An amplified Ti:Sapphire laser (*Dragon – KM Labs*) was used, emitting pulses of 50 fs, centered at 785 nm and at a repetition rate of 1 kHz. The beam passes through a dispersive line consisting of a *Thorlabs* femtosecond pulse compressor (*Thorlabs FSPC*). The pulse compressor is composed of a pair of prisms, such that one of them is mounted on top of a translation stage, allowing its motion. The ultrashort pulses dispersion is varied by moving the prism and inserting more or less material into the optical path. The output beam from the pulse compressor is then directed to a coupling system and to a *Grenouille* (*Swamp Optics*), where spectral phase characterization is realized through the FROG (Frequency Resolved Optical Gating) technique.[80] In the coupling system, the beam is coupled to the waveguide/fiber sample by an objective lens. The output signal is collected by another objective lens. Both objectives and the sample are positioned on three-dimensional translation stages with micrometric precision to allow

coupling optimization. The transmitted signal is directed to a spectrometer (*HR4000 Ocean Optics*) by a multimode optical fiber. A power meter is also positioned after the output lens, allowing the determination of the guided power. An aperture is also positioned right after the output lens so that only the guided mode is transmitted, minimizing light that was eventually scattered through the sample and that can affect the power and spectral measurements. To observe the guided mode, an image of the waveguide output surface can be projected on a CCD camera placed after the output lens.

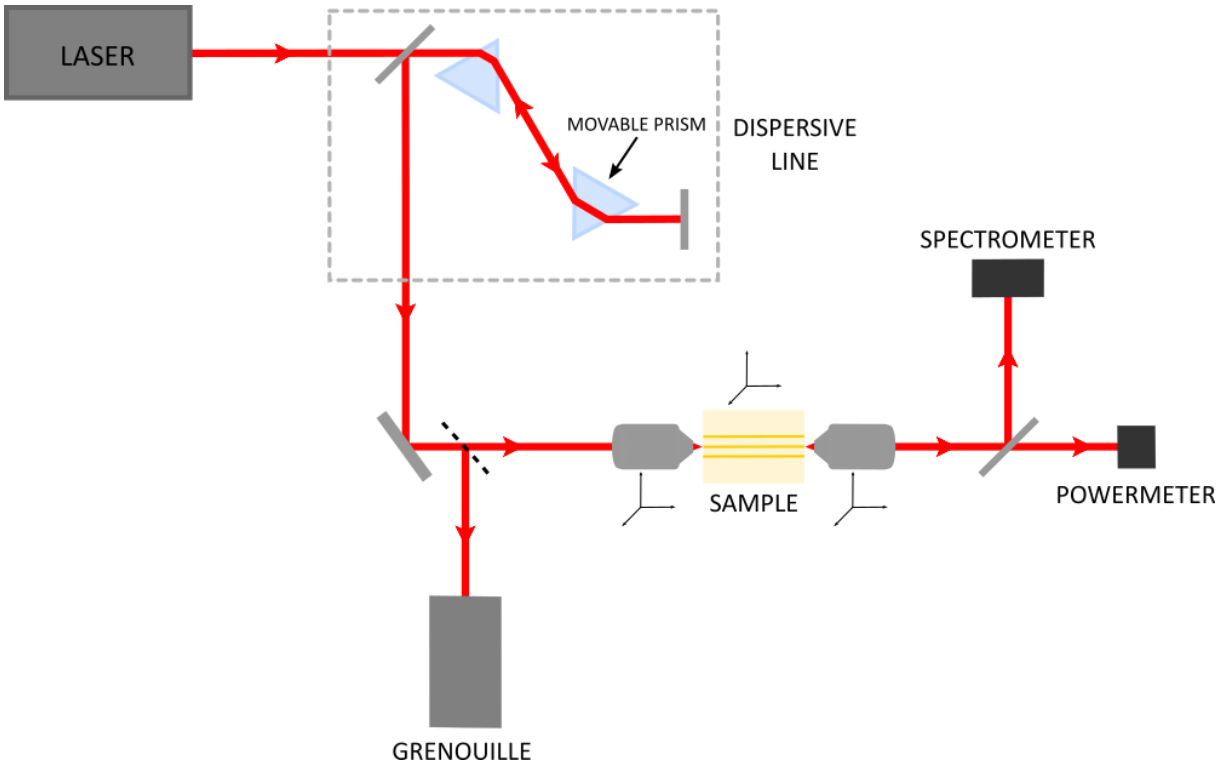

Figure 3.2 - Scheme of the experimental setup implemented for the Dispersive-scan technique.
Source: By the author

3.3.2 Dispersion compensation

In general, in the visible and near-infrared region of the electromagnetic spectrum, positive second-order dispersion is introduced to ultrashort pulses when propagating through a medium. As previously discussed, dispersion leads to the temporal broadening of the pulse, an undesirable phenomenon when it comes to the observation of nonlinear optical phenomena. The positive dispersion accumulated by a pulse when crossing a material can be compensated through devices that are able to introduce negative dispersion. This can be performed by geometric dispersion in

pulse compression systems, usually composed by pairs of prisms or diffraction gratings.[81] We can take as an example our *Thorlabs* pulse compressor composed of a pair of prisms, as illustrated in Fig. 3.3. If we consider only the dispersion provided by the material of the prisms, a pulse would acquire a positive chirp when crossing both prisms. However, the prisms are positioned in such a way that higher frequency components will travel through a longer optical path than the lower frequency components, compensating the positive dispersion acquired through pulse propagation in material media, by means of geometrically engineered negative dispersion.[81] When the amount of prism material inserted into the optical path is varied, the dispersion introduced to the ultrashort pulse is changed, being possible to scan it from negative to positive values. Pulse compression devices are usually employed in high sensitivity spectroscopy and microscopy techniques, where the dispersion introduced by optical components is compensated in order to achieve FT-limited pulses at the sample, increasing the intensity applied.[82]

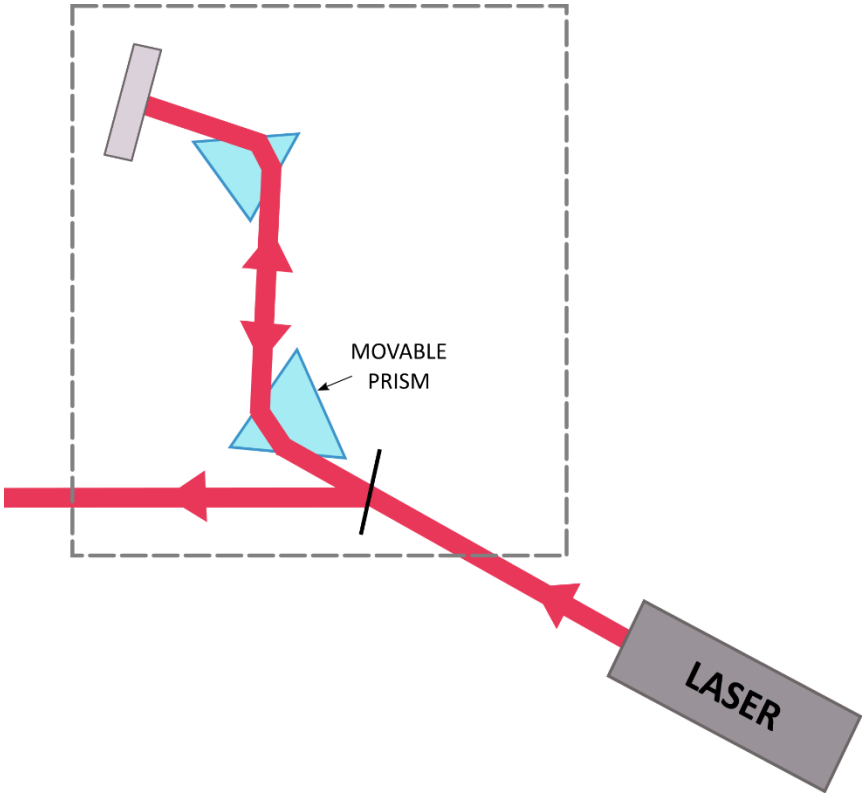

Figure 3.3 - Scheme of the experimental setup of a pulse compressor composed of a pair of prisms, where one of them is movable.
Source: By the author

3.3.3 Automation of the experimental setup

To optimize the Dispersive-scan measurements, we realized the automation of the experimental setup. In Fig. 3.4 we can observe a simplified scheme of it, including the automation components. A step motor was connected to the pulse compressor translation stage, where there is a knob to control the prism movement. The step motor is computer-controlled using a data acquisition board (DAQ) from *National Instruments.* Two digital output ports from the board are used to control the motor movement; one to control the movement direction (clockwise or counter-clockwise) and the other to control the number of steps applied. The digital signal provided by the DAQ has low voltage (5 volts) and must pass through a current driver, where the signal is amplified and enough current can be provided to the step motor. Furthermore, in the current driver, an integrated circuit generates the right signal sequence required to drive the step motor coils, allowing its movement.

A *LabVIEW* code was written to control the motor motion and synchronize it to the spectra acquisition in the *HR4000* (*Ocean Optics*) spectrometer. This way, we are able to realize the dispersion scan by moving the prism and collect the output spectra in pre-determined positions. The prism insertion length is given by a display on the pulse compressor that provides a DC output that is acquired by the DAQ system. The DC output was calibrated according to the display reading. We can now move the prism, record its exact position and save the spectrum automatically, meaning that several scans can be performed in a practical manner.

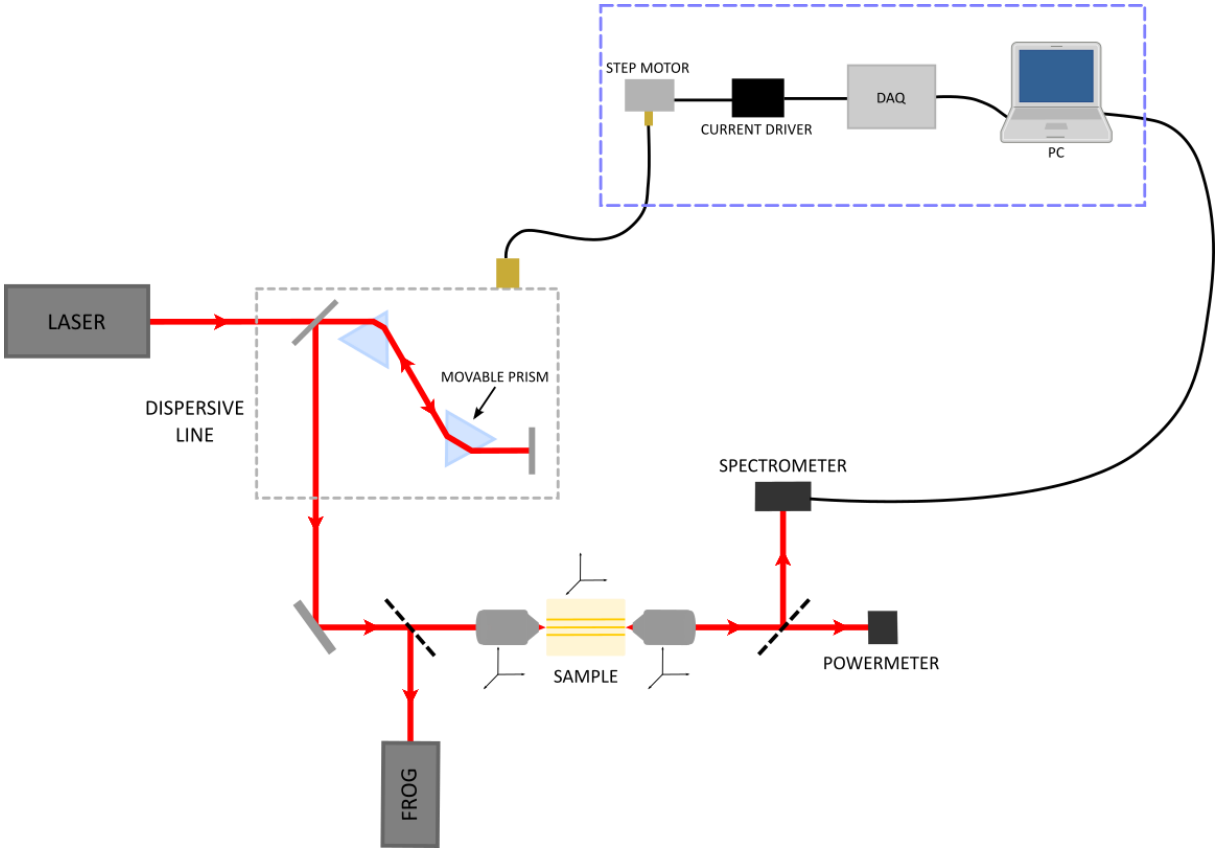

Figure 3.4 - Scheme of the experimental setup of the Dispersive-scan technique, modified to include the automation components.
Source: By the author

3.3.4 Characterization of the dispersive line

In order to build the Dispersive-scan curve, it is necessary to characterize the dispersion of the input ultrashort pulses for different positions of the movable prism. As shown in Section 3.3.1, part of the incident beam is directed to a *Grenouille*, where the pulses FROG trace is obtained.[80] A retrieval algorithm is applied to the experimental FROG traces, so the temporal and spectral properties of the pulses are determined. Among these properties, the second-order spectral phase coefficient $\phi^{(2)}$, i.e. the second-order dispersion, can be obtained. Fig. 3.5 features an example of a retrieved FROG trace (a), as well as its spectral phase (b). In this example, the ultrashort pulse presents a spectral phase of second-order that can be fitted by a second-order polynomial $ax^2 + bx + c$, where a is proportional to the phase coefficient $\phi^{(2)}$.

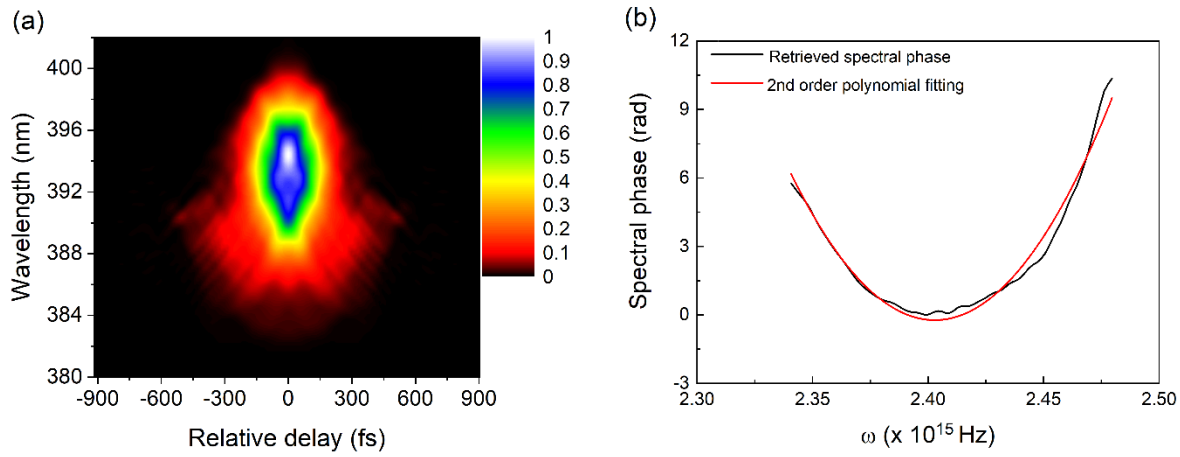

Figure 3.5 – (a) Example of a retrieved FROG trace of an ultrashort pulse from a Ti:Sapphire laser. (b) Corresponding retrieved spectral phase (black line) and fitting with a second-order polynomial (red line).
Source: By the author

This way, we characterized the pulse's FROG trace for different positions of the movable prism, determining the second-order coefficient $\phi^{(2)}$. In Fig. 3.6, we can observe an example of a calibration curve, showing the pulse dispersion according to the amount of prism D inserted to the optical path, which is the value shown in the display of the *Thorlabs* pulse compressor. We can conclude that our pulse compressor provides an approximate dispersion range of -3000 to +3000 rad.fs^2. Dispersion varies linearly with prism insertion and the calibration curve slope is different for positive and negative dispersion.

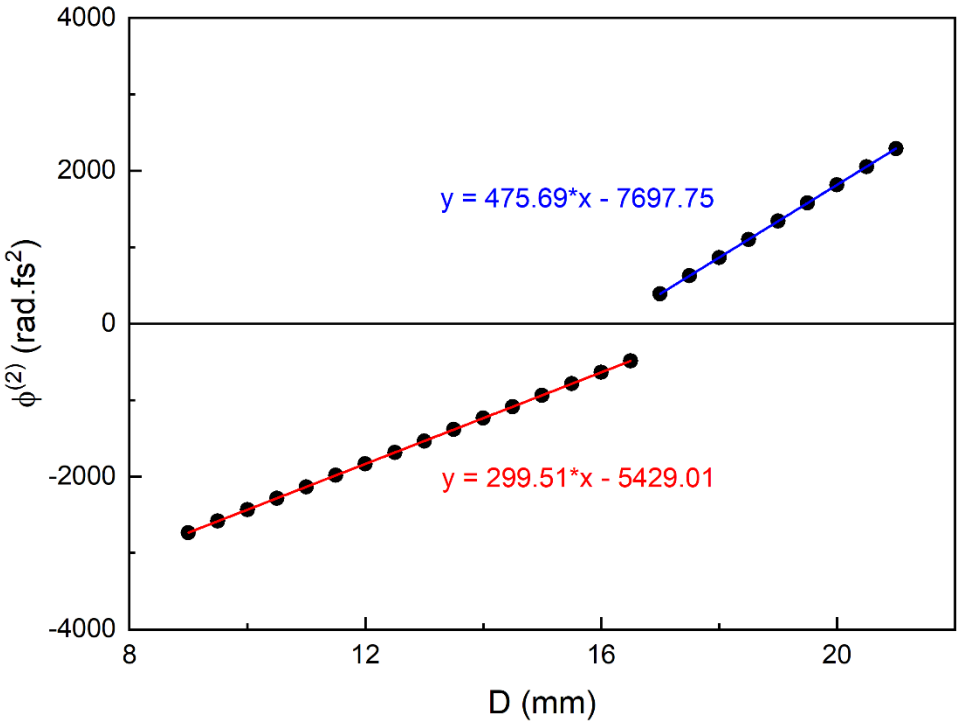

Figure 3.6 – Example of a calibration curve for the dispersive line, showing the spectral phase $\boldsymbol{\phi}^{(2)}$ as a function of the movable prism insertion D.
Source: By the author

3.4 Data analysis

3.4.1 Post-processing of collected spectra

When the nonlinear phase induced to an ultrashort pulse by self-phase modulation is moderated, the pulse spectrum suffers mildly modifications, such as spectral broadening or spectral narrowing in the case of a Gaussian input spectrum, for instance. However, as the nonlinear phase increases, the spectrum of the traveling pulse becomes more complex, even including sidebands.[83] In this case, the spectral features, like width and peak intensity, cannot be determined by a Gaussian fit. However, the spectral width can be easily determined if we consider the spectrum as a wavelength distribution and calculate its standard deviation σ. This way, we created a *Matlab* code that is able to numerically determine the spectral width, regardless of the spectrum shape.

Initially, the spectrum is normalized by the integral of the intensity $y(x)$, which is equivalent to normalizing the spectrum by the total power. Then we calculate

$$< x >= \int x.y(x)dx \tag{3.2}$$

and

$$< x^2 >= \int x^2.y(x)dx, \tag{3.3}$$

where x is the wavelength vector and $y(x)$ is the normalized intensity. The standard deviation, i.e. the spectral width, is then calculated by

$$\sigma = \sqrt{< x^2 > - < x >^2}. \tag{3.4}$$

This way, the spectral width can be obtained even for complex spectra and the experimental Dispersive-scan curves can be built.

3.4.2 Dispersive-scan numerical model

To determine the sample nonlinear properties from the experimental Dispersive-Scan data, numerical simulations were realized to fit the D-scan curve. A numerical model was built in *LabVIEW*, using the add-on *Lab2 – A virtual femtosecond laser lab*[79], a modular coding tool that allows for the simulation of femtosecond laser experiments in an intuitive manner. In our model, we inserted an ultrashort pulse with Gaussian spectral band, which features like energy, beam diameter, bandwidth and central wavelength are inserted by the user. The pulse passes through a pulse formatting modulus, where second-order dispersion is introduced and varied. Then the pulse passes through a nonlinear material of length L and nonlinear refractive index n_2, where the self-phase modulation process takes place. Finally, the output spectrum is analyzed and its width σ is recorded. When the second-order dispersion is varied from negative to positive values, the numerical D-scan curve is built.

In the nonlinear material, the self-phase modulation phenomenon is simulated numerically through an algorithm that uses the Split-Step Fourier Transform Method[83]

to solve the Nonlinear Schroedinger Equation that describes an ultrashort pulse propagation through a nonlinear medium. In general, this equation cannot be analytically solved and is given by[83]

$$i\frac{\partial U}{\partial z} - \frac{\beta_2}{2}\frac{\partial^2 U}{\partial t^2} + \gamma|U^2|U = 0. \tag{3.5}$$

U represents the pulse electric field propagating in z direction, β_2 is the material group velocity dispersion (GVD), i. e. the group delay dispersion (GDD) per unit length, and γ represents the material third-order refractive nonlinearity and it is written as

$$\gamma = \frac{2\pi n_2}{\lambda_0 A_{eff}} \tag{3.6}$$

n_2 is the medium nonlinear refractive index, λ_o is the input pulse central wavelength and A_{eff} is the laser mode effective area. For simulations in waveguides or optical fibers, A_{eff} corresponds to the effective area of the guided mode.

In the Split-Step Fourier Transform Method algorithm used in our model, the material is split into slices, and the linear and nonlinear parts of Eq. 3.7 are treated separately. Linear dispersion is solved in frequency domain, while nonlinear propagation is solved in time domain. Fourier transforms are used to change from one domain to the other. In the *Lab2* algorithm, the material is divided in several slices of length h, and each slice is divided in three regions. In the first region, the nonlinear term is ignored and the effect of half of the dispersion from the h slice is calculated. The resulting field is Fourier transformed and the effect of nonlinear propagation is calculated for the whole slice h, while the dispersion term is ignored. The resulting field is once again Fourier transformed and in the third region the effect of the other half of the dispersion is calculated. The same procedure is repeated for all slices of h length until the whole extension of the material is completed. The h length is dynamically adjusted so that the nonlinear phase for each slice is small and set to $\pi/20$. In Fig. 3.7, we can observe a visual representation of the Split-Step algorithm applied to a waveguide.

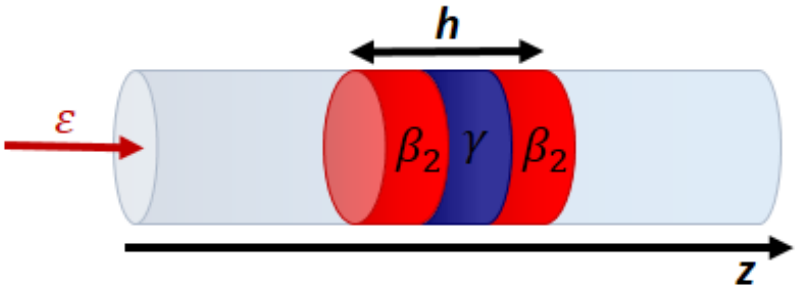

Figure 3.7 - Visual representation of the Split-Step Fourier Transform Method in a waveguide. The waveguide is divided in slices of length $\boldsymbol{h}$. Each slice is divided in three parts, where the effects of dispersion and self-phase modulation are calculated separately.
Source: By the author

The input parameters used in the simulations are carefully determined experimentally. The parameters λ_0 (central wavelength of input beam) and $\Delta\lambda$ (bandwidth of input beam) are obtained through the characterization of the input beam spectrum. The pulse energy E coupled to the waveguides is measured at their output with a power meter. For low-loss and short waveguides, we approximate the input pulse energy to the value measured at the output. Cases where attenuation through the waveguide cannot be ignored will be treated in Section 3.4.4. The beam diameter d, used to calculate the effective mode area, is determined through the analysis of pictures taken from the output of the waveguides with a CCD camera positioned after the output objective lens. The material group velocity dispersion (GVD) is chosen according to values found in the literature. The waveguide total length L can be easily determined by measuring the sample, for the case of straight waveguides. The nonlinear refractive index n_2 is a free parameter. Its value is manually changed so the numerical curve can best fit the experimental data. This way, we can determine the nonlinear refractive index of the studied waveguides.

3.4.3 Validation of the numerical model

In order to test our experimental model, we performed simulations to reproduce the Dispersive-scan experiments realized by Louradour *et al*.[66] in a single-mode silica fiber. In Fig. 3.8 (a), we can observe the experimental data and numerical curve realized by Louradour *et al.,*[66] and in Fig. 3.8 (b) we observe the curve reproduced by our model. The input parameters used in our model were extracted from the reference and are: $E = 0.13\,nJ$, $d = 3.3\,\mu m$, $\lambda_0 = 830\,nm$, $\Delta\lambda(FWHM) =$

$13\ nm$, $L = 5.35\ cm$ and GVD of silica material SQ1.[84] The nonlinear refractive index n_2 used to best reproduce the reference curve was $3.1 \times 10^{-20}\ m^2/W$, the same found by Louradour *et al.,*[66] which is also in accordance to values found in the literature for silica.[85]

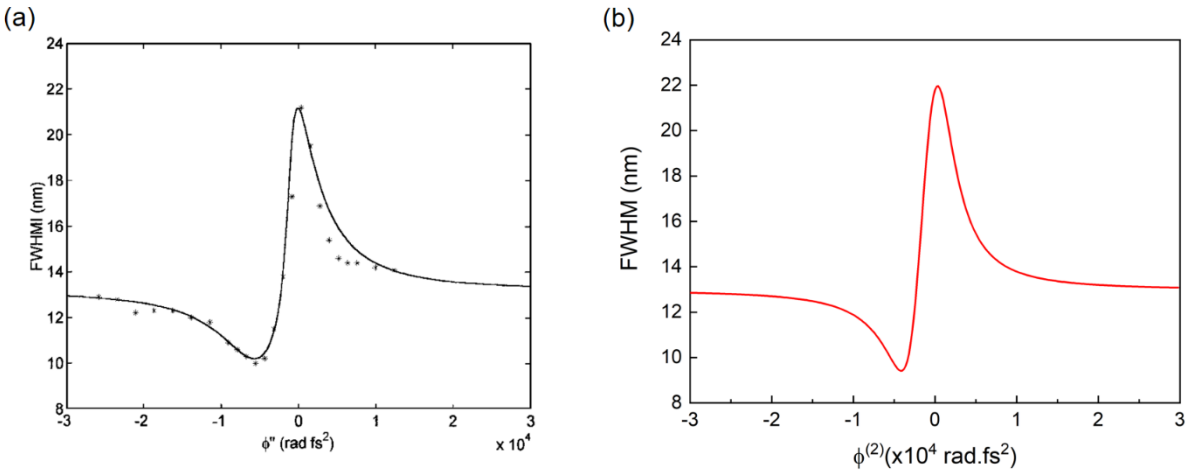

Figure 3.8 - (a) Experimental D-scan data and numerical curve for a measurement performed in a single mode silica fiber by Louradour *et al.*[66] (b) D-scan curve simulated with our numerical model with the same input parameters as (a).
Source: (a) LOURADOUR *et al.*;[66] (b) By the author

3.4.4 Modified Dispersive-Scan numerical model for lossy media

The developed numerical model presented in Section 3.4.2 does not take into account guiding losses, and it performs very well for low loss transparent waveguides and fibers, as shown in Fig. 3.8. However, for many waveguides and fibers absorption and scattering losses can play an important role, like doped semiconductor waveguides,[86] ion-doped glass waveguides,[87] chromophore-doped polymer waveguides,[88-89] nanoparticle-doped waveguides,[90-91] etc. This way, we developed a modified numerical model to include optical losses, so that it can be applied to a broader range of samples.

In the modified Dispersive-Scan numerical model, first the whole material length L is divided in smaller steps of length l, as demonstrated in Fig. 3.9. For each step the input energy is changed through the Beer-Lambert law:[92]

$$E_n = E_{n-1}\exp(-\mu l), \tag{3.7}$$

where E_n is the pulse energy in the n step, E_{n-1} is the pulse energy in the $n-1$ step and μ is the attenuation coefficient, given in dB per unit length.

Inside the n step, the Split-Step Fourier Transform Method is applied to solve nonlinear propagation as described in Section 3.4.2. The resulting electric field is used as input to the $n+1$ step, but with its pulse energy updated by the Beer-Lambert law. This double split-step process is repeated through the whole L extension. The length l is manually set by the user. A good value to get reliable results is chosen by decreasing the length l until the Dispersive-scan curve converges, i.e. stops changing with l length.

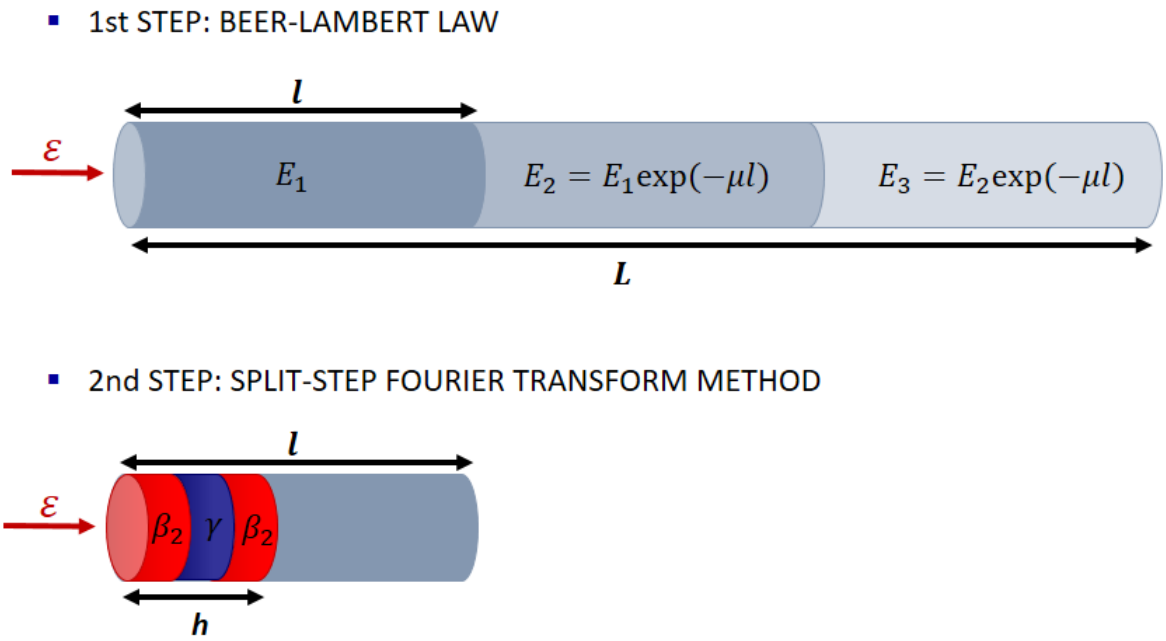

Figure 3.9 - Visual representation of the modified Split-Step Fourier Transform Method to include guiding losses. The material is first divided in steps of length $\boldsymbol{l}$, where the Beer-Lambert law is used to change the input pulse energy according to the losses. Then, inside each $\boldsymbol{l}$ step, the Split-Step Fourier Transform Method is applied.
Source: By the author

The attenuation coefficient μ can be determined in different ways, such as the cut-back method,[93] Fabry-Perot resonances contrast,[94] scattering images of the length of the waveguide, etc. When the pulse energy E coupled to the waveguide is measured at the output, this value needs to be corrected by the Beer-Lambert law for the whole extension L in order to determine the input pulse energy value to be used as parameter in our model.

3.5 Absorptive Dispersive-Scan technique

Among the many advantages of the Dispersive-Scan technique when compared to other methods to characterize the third-order nonlinearities of waveguides, we can highlight its sensitivity, that is only limited by the spectrometer resolution, and the fact that it is a single beam technique, which simplifies its experimental setup.[66] Another important advantage is the possibility to characterize both nonlinear refraction and absorption simultaneously.[95] By adding a power meter to the output of the waveguide, like it is shown in Fig. 3.2, and recording the transmitted power as a function of the input dispersion, two-photon absorption Dispersive-scan curves can be built.

The two-photon absorption phenomenon was first described by Maria Göppert-Mayer in her doctoral thesis in 1931.[76] In this phenomenon, an atom or molecule transitions from a lower energy state to a higher energy state by simultaneously absorbing two photons. Its first experimental observation was done by Kaiser et al.[77] in 1961, with the laser advent, and they observed the two-photon fluorescence of a $CaF_2{:}Eu^{2+}$ crystal.

In Fig. 3.10 we can observe images of the emission profile of a fluorescein solution when the chromophore is excited by one (a) and two-photon absorption (b). The energy diagrams show the molecular transition from ground state g to excited state n. In the case of two-photon absorption, the process is intermediated by the virtual state m and two photons with half of the energy of the photon in (a) are absorbed. This is an illustration of the degenerate two-photon absorption process. The non-degenerate case occurs when the two photons that are simultaneously absorbed don’t have the same energy.

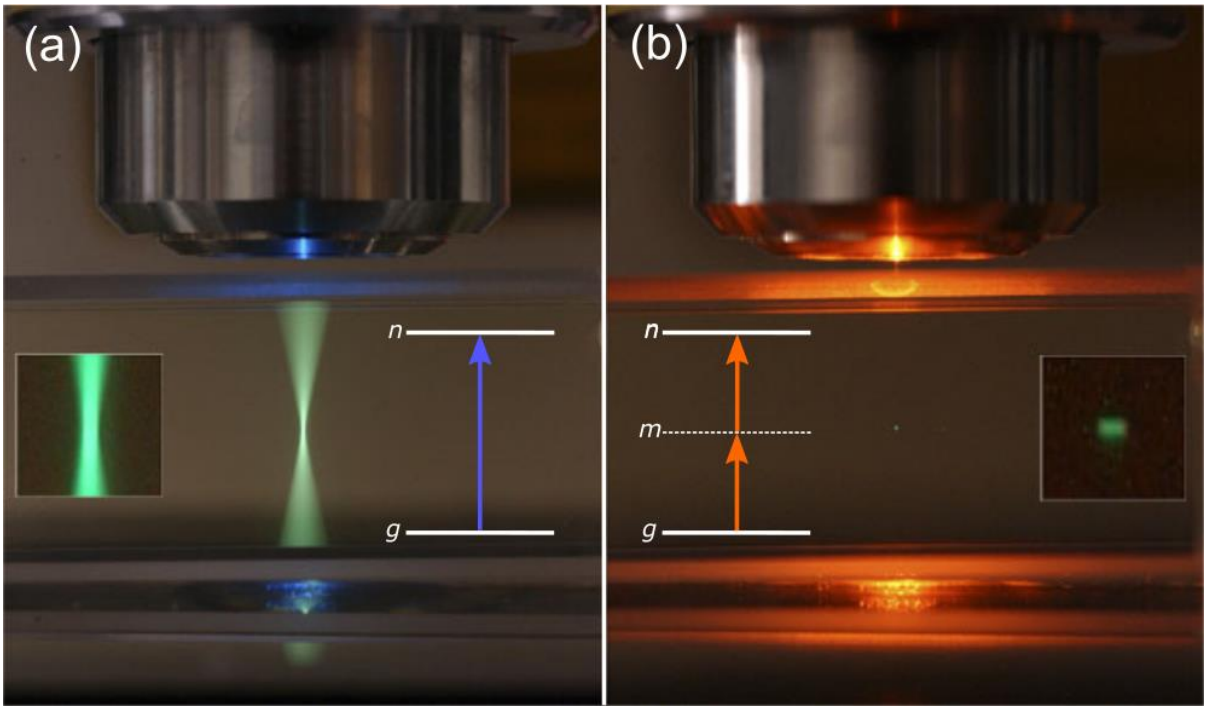

Figure 3.10 - Comparison between the emission profile of a fluorescein solution when excited by the absorption of one (a) and two photons (b) and their respective energy diagrams.
Source: Adapted from RUZIN; AARON[96]

In Fig. 3.10 we can observe how the emission profile differs from excitation with one and two-photon absorption. In the case of one-photon absorption, emission occurs through the whole optical path, while for two-photon absorption it is only observed in a small region around the focal spot. This can be explained by the dependence of two-photon absorption with intensity, as shown in Eq. 2.9. Considering the linear absorption coefficient as zero ($\alpha_0 = 0$), the Beer-Lambert law for two-photon absorption becomes:

$$\frac{dI}{dz} = -\alpha(I)I = -(\alpha_0 + \beta I)I = -\beta I^2, \tag{3.8}$$

where I is the light intensity. This way, Eq. 3.8 shows that the intensity of a beam propagating in z direction varies with rate proportional to the square of intensity I, when two-photon absorption is involved, conferring high spatial localization to the phenomenon.

To be able to characterize the two-photon absorption coefficient β in waveguides through the Dispersive-Scan technique, we performed further modifications to the developed numerical model. We once again implemented a

modified Split-Step Fourier Transform Method as described in Section 3.4.4. Equation 3.7 was modified to include two-photon absorption as follows:

$$E_n = E_{n-1} \exp(-(\mu + \beta \mathrm{I})l). \quad (3.9)$$

The sample is once again divided in several steps of length l and the pulse energy is updated for each l step according to Eq. 3.9. The Split-Step Fourier Transform Method is applied to each l step with the respective calculated energy.

In Fig. 3.11, we can observe absorptive Dispersive-Scan curves that were simulated with our model. The curves show the transmittance of an ultrashort pulses beam as function of the input dispersion for positive (a) and negative (b) two-photon absorption coefficient β. These curves are similar to the ones for open aperture Z-scan.[62] An effective negative two-photon absorption coefficient is used to describe the saturable absorption effect.[97-98]

This way, our numerical model is now able to simulate third-order nonlinear absorption, besides nonlinear refraction. This feature is particularly interesting to characterize semiconductor waveguides,[95] dye-doped polymer waveguides[88-89] or graphene-doped structures,[31,86] where nonlinear absorption plays an important role.

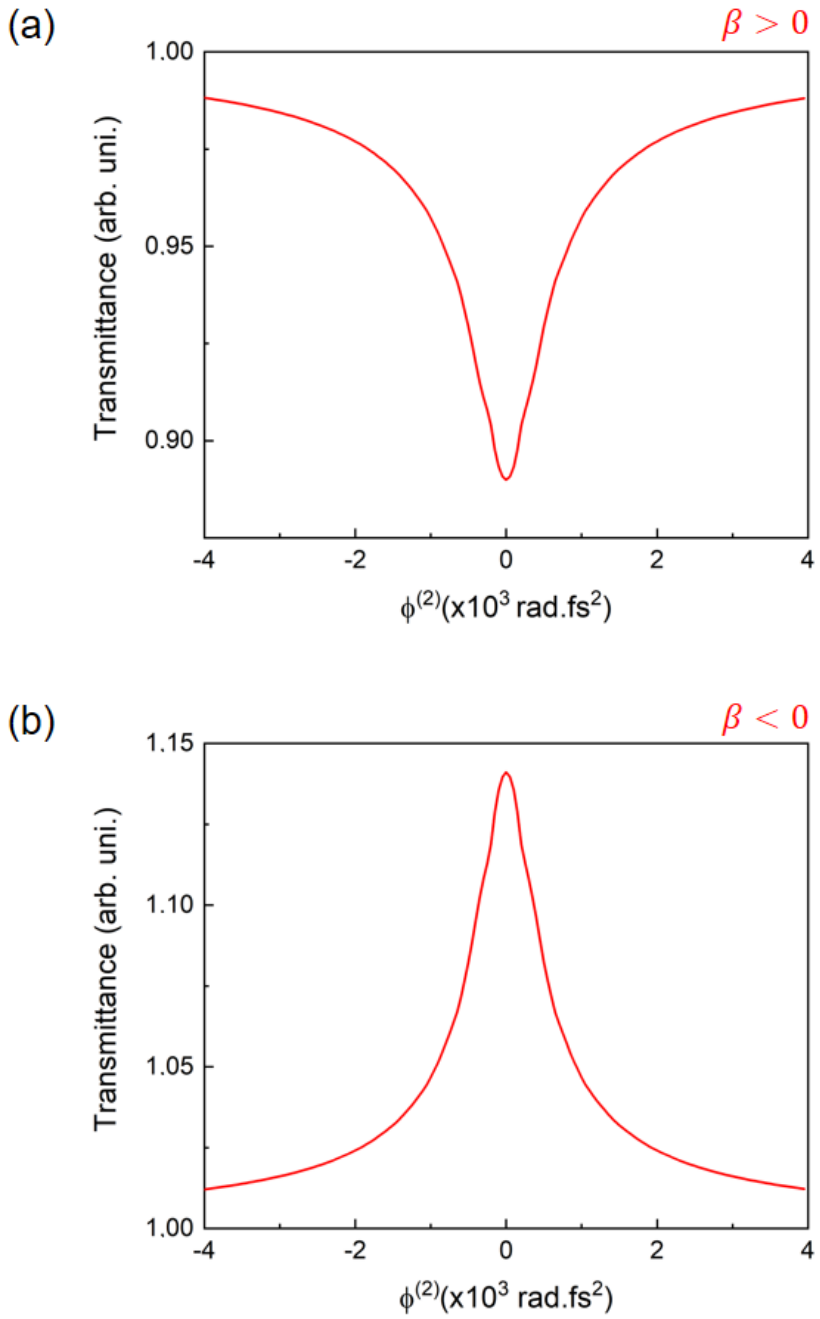

Figure 3.11 - Simulation of typical absorptive Dispersive-scan curves for (a) positive and (b) negative two-photon absorption coefficient $\boldsymbol{\beta}$, showing the transmition of an ultrashort pulse beam as function of the input dispersion $\boldsymbol{\phi}^{(2)}$.

Source: By the author

4 THIRD-ORDER NONLINEAR CHARACTERIZATION OF GORILLA® GLASS WAVEGUIDES

Corning® Gorilla® Glass is an alkali-aliminosilicate glass that is commonly used as protective screen in mobile devices such as notebooks, smartphones, and tablets.[99] This material goes through an ion exchange process,[37] in which the glass slide is submerged in a hot potassium bath at 400°C. During this process, sodium ions from the glass matrix are replaced by potassium ions from the bath, mainly in the region close to the surface. As potassium ions are bigger and more massive than sodium ions, this process creates a compression zone that can extend to approximately 200 µm below the glass surface. The compression zone is responsible for the modification of the material's mechanical properties, making it more resistant to drops and less prone to scratches. These features have prompt the application of Gorilla® Glass on large scale in the industry of mobile devices, with more than 8 billion devices fabricated.[100] In the past years, studies revealed that Gorilla® Glass is also an interesting material for direct laser writing with femtosecond pulses. Lapointe *et al.*[44] were the first to demonstrate the fabrication of ultra-long Gorilla® Glass waveguides close to the surface that presented single-mode guidance with high quality modes. The most interesting feature that they present is certainly the low propagation losses, below 0.03 dB/cm, which is the record achieved with the DLW technique. Due to the high light intensities often present in integrated photonic circuits, the characterization of the nonlinear optical properties of these waveguides becomes crucial in order to direct their application in different fields. This way, in this Chapter we will present our studies related to the third-order nonlinear characterization of Gorilla® Glass waveguides by the Dispersive-Scan technique.

4.1 Fabrication

The fs-laser written Gorilla® Glass waveguides used in this work were fabricated during the PhD project of Prof. Dr. Gustavo Foresto Brito de Almeida,[101] according to the experimental scheme showed in Fig. 4.1. An amplified Ti:Sapphire laser (*Clark-MXR*: 150 fs, 775 nm, 1 kHz) was focused approximately 70 µm below the glass surface by an objective lens of 0.65 NA. The sample was positioned on a

computer controlled movable platform, allowing the inscription of 15 mm-long waveguides at 200 µm/s.

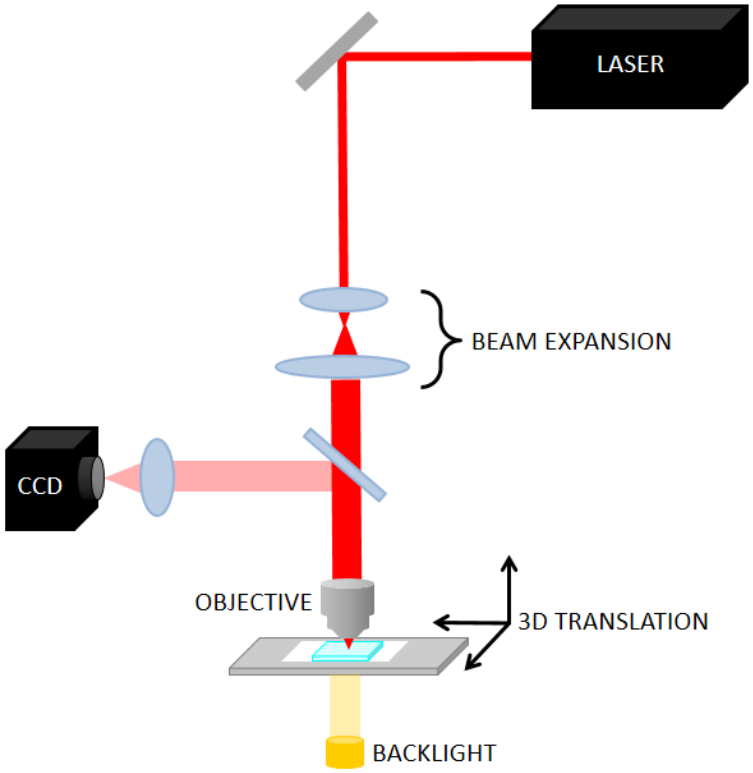

Figure 4.1 - Scheme of the experimental setup used for the inscription of the fs-laser written Gorilla® Glass waveguides.
Source: By the author

Different waveguides were fabricated varying the excitation pulse energy. We realized the third-order nonlinear characterization of waveguides that were fabricated by pulses of 250 nJ (type A) and 500 nJ (type B). These waveguides were chosen because they presented good mode profiles, as shown in Fig 4.2.

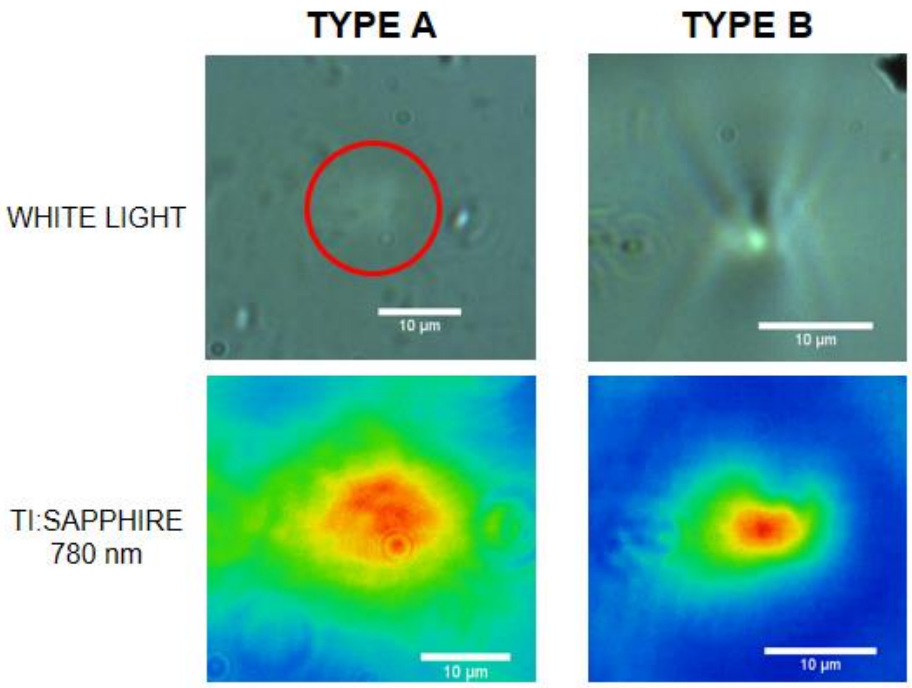

Figure 4.2 - Image of the transversal profile of the type A and type B waveguides when illuminated by white light (top) and transversal profile of the guided mode when the beam of a Ti:Sapphire laser centered at 780 nm is coupled to the waveguides.
Source: By the author.

4.2 Dispersive-scan measurements

4.2.1 Experimental Methods

A scheme of the experimental setup of the Dispersive-Scan technique is shown in Fig. 4.3. The beam of an amplified Ti:Sapphire laser (50 fs, 785 nm, 1 kHz) passes through a dispersive line that consists of a pulse compressor (*Thorlabs FSPC*) constituted of two prisms. One of the compressor's prisms is mounted on top of a translation stage. This way, the input pulse dispersion can be varied by changing the prism position, inserting more or less material into the optical path. After passing through the pulse compressor, part of the beam is directed to a *Grenouille* (*Swamp Optics*), in which the characterization of the spectral phase is realized through the beam FROG trace.[80] After passing through the dispersive line, the beam is coupled to the waveguide by an objective lens (0.25 NA). The transmitted signal is collected by another objective lens (0.40 NA) and directed to a spectrometer (*HR4000 Ocean Optics*) through a multimode optical fiber. The sample and the objective lenses are

mounted on 3D moving platforms, allowing the coupling process. A power meter is also placed after the output objective lens to measure the guided power.

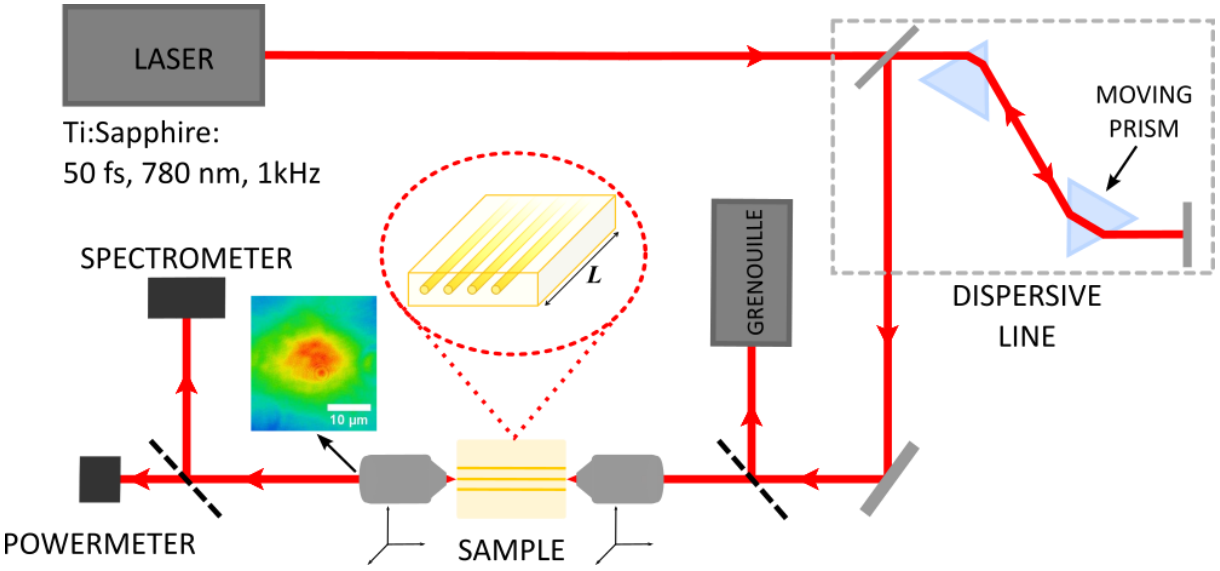

Figure 4.3 - Experimental setup for the Dispersive-Scan measurements in Gorilla® Glass waveguides
Source: Adapted from HENRIQUE *et al.*[102]

4.2.2 Results and Discussion

In Fig. 4.4 we can observe the transmitted spectra of the type A waveguide for different values of $\phi^{(2)}$, the second-order dispersion of the input ultrashort pulses, determined by the FROG technique. For the *Thorlabs* pulse compressor used as dispersive line in this work, the second-order dispersion can be varied from approximately -3000 fs^2 to +3000 fs^2 for a pulse centered at 780 nm. Observing Fig. 4.4, one can notice that, as the value of $\phi^{(2)}$ increases, getting close to zero from negative values, the spectrum peak intensity increases, and the peak becomes narrower, i.e. we observe spectral compression. Shortly after, the spectrum peak intensity drops and the peak becomes broader. The broadening effect decreases as $\phi^{(2)}$ increases until we reach a plateau where dispersion is too high, and the input pulse is too broad in time for nonlinear effects to be observed. This plateau is reached for large values of $\phi^{(2)}$ for both cases of negative and positive input pulse dispersion. If when varying the input dispersion from negative to positive values, the spectral compression is observed before the spectral broadening, we are dealing with a material of positive nonlinear refractive index.

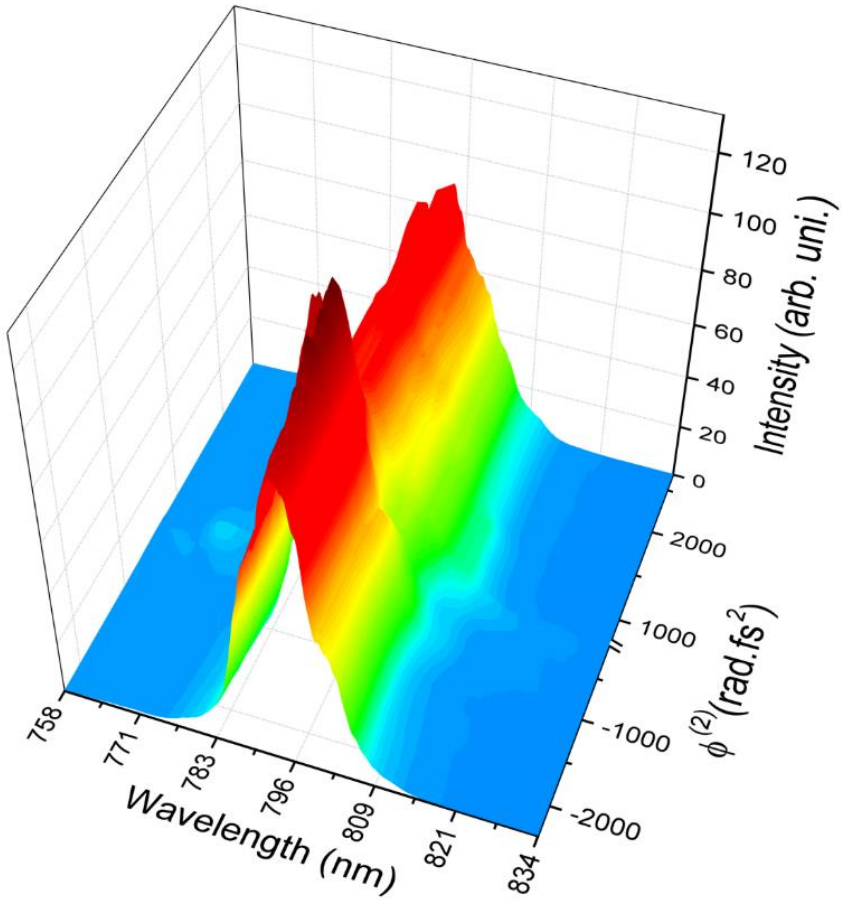

Figure 4.4 - Spectrum at the output of the type A waveguide as a function of the input beam second-order dispersion $\boldsymbol{\phi^{(2)}}$.
Source: Adapted from HENRIQUE *et al*. [102]

We realized the post-processing of the spectra shown in Fig. 4.4 to obtain the spectral width σ. The results are shown in Fig. 4.5, where we can observe the experimental D-scan curve (red dots). In order to obtain the nonlinear refractive index from the experimental data, we realized numerical simulations (black curve) as previously described in Section 3.4.2. The input ultrashort laser pulse features, as well as the waveguides features, were carefully determined experimentally and inserted into the simulation. For the data shown in Fig. 4.5, the following input parameters were used: $E = 20.5\,nJ$, $\lambda_0 = 785\,nm$, $\Delta\lambda = 20\,nm$, $L = 15\,mm$ and $d = 32.5\,\mu m$. By fitting the experimental data, we obtained $n_2 = (0.9 \pm 0.3) \times 10^{-20}\,m^2/W$.

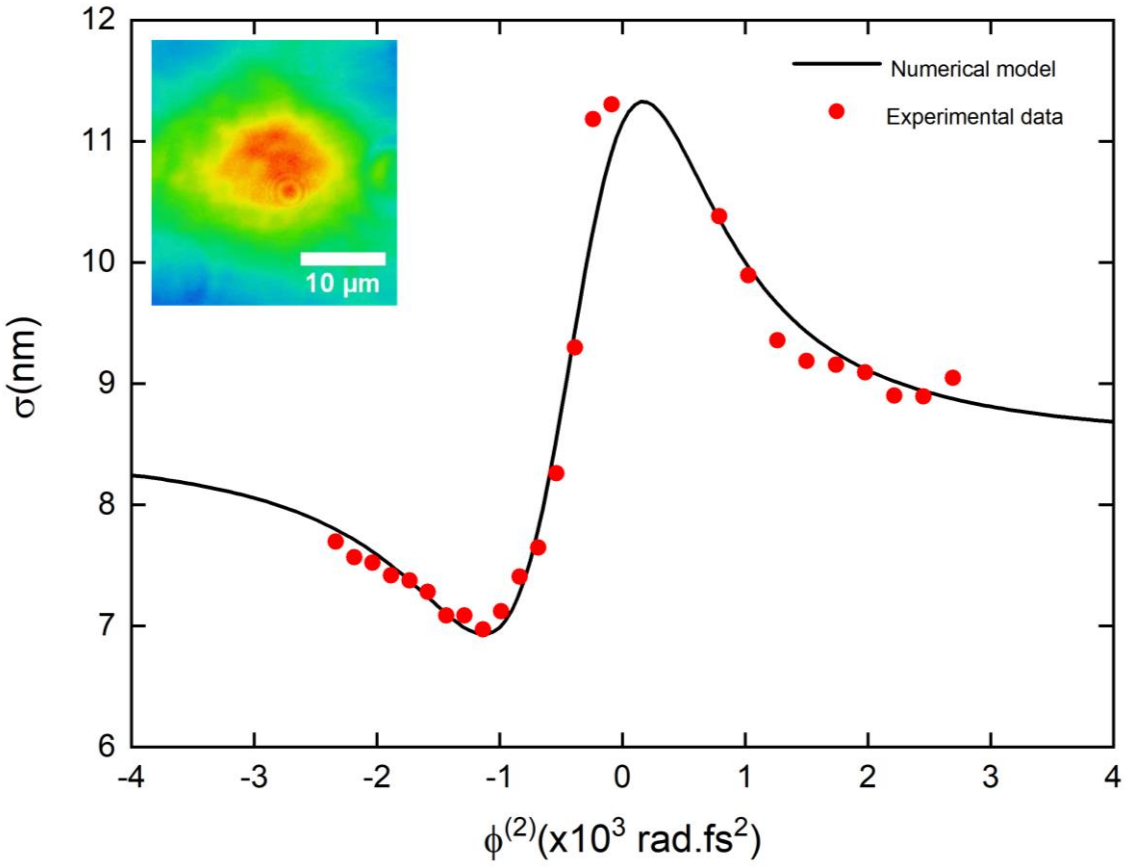

Figure 4.5 - D-scan measurement in the type A waveguide (red dots) and numerical model curve (black line) adjusted to the experimental data. The model input parameters used herein were: $\boldsymbol{E = 20.5\,nJ}$, $\boldsymbol{\lambda_0 = 785\,nm}$, $\boldsymbol{\Delta\lambda(FWHM) = 20\,nm}$, $\boldsymbol{d = 32.5\,\mu m}$ and $\boldsymbol{L = 15\,mm}$, resulting in $\boldsymbol{n_2 = (0.9 \pm 0.3) \times 10^{-20} m^2/W}$. Inset: guided mode for the type A waveguide.
Source: Adapted from HENRIQUE *et al.*[102]

We also realized D-scan measurements in the type B waveguide, that was fabricated with pulse energy of 500 nJ. The results are shown in Fig. 4.6. The input parameters used in the numerical model were: $E = 25.5\,nJ$, $\lambda_0 = 785\,nm$, $\Delta\lambda(FWHM) = 29.5\,nm$, $d = 19\,\mu m$ e $L = 15\,mm$, resulting in $n_2 = (0.07 \pm 0.02) \times 10^{-20} m^2/W$.

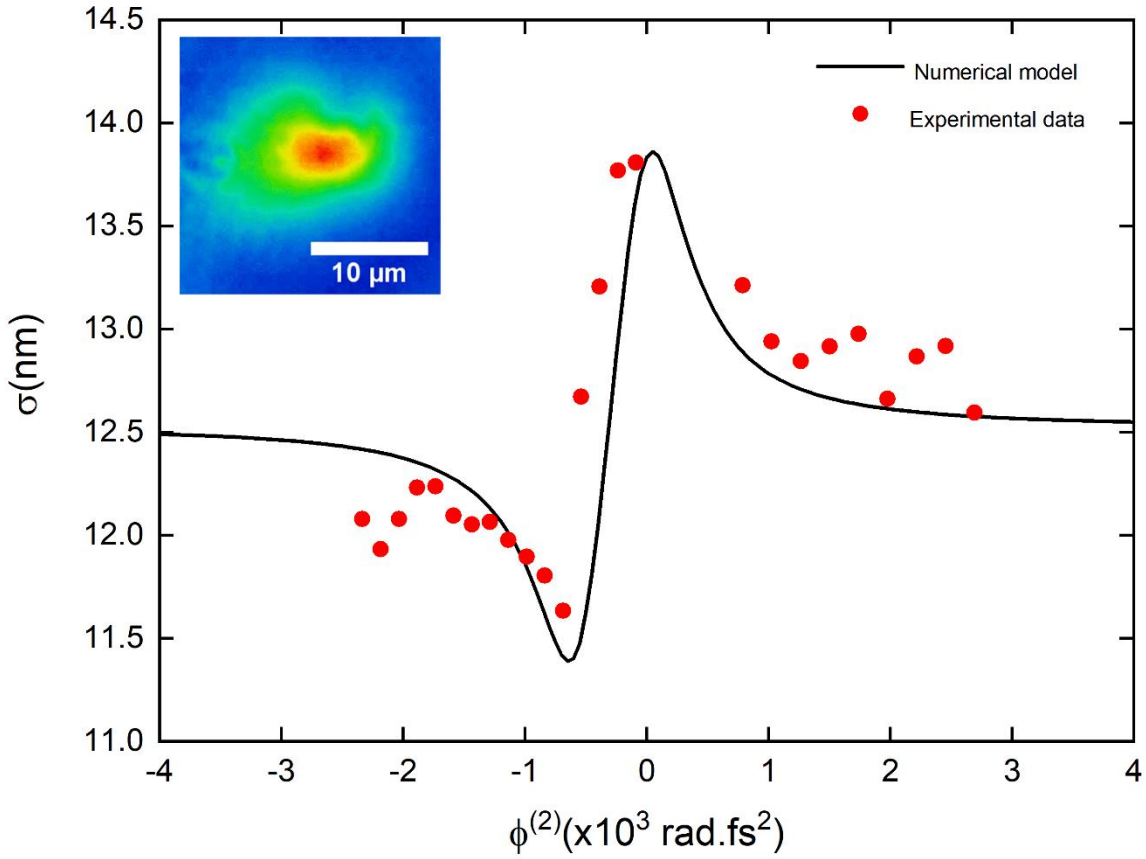

Figure 4.6 - D-scan measurement in the type B waveguide (red dots) and numerical model curve (black line) adjusted to the experimental data. The model input parameters used herein were: $\boldsymbol{E = 25.5\,nJ}$, $\boldsymbol{\lambda_0 = 785\,nm}$, $\boldsymbol{\Delta\lambda(FWHM) = 29.5\,nm}$, $\boldsymbol{d = 19\,\mu m}$ and $\boldsymbol{L = 15\,mm}$, resulting in $\boldsymbol{n_2 = (0.07 \pm 0.02) \times 10^{-20} m^2/W}$. Inset: guided mode for the type B waveguide.
Source: Adapted from HENRIQUE *et al.*[102]

According to Almeida *et al.*,[103] the nonlinear refractive index of bulk *Gorilla® Glass* is on average $(3.3 \pm 0.6) \times 10^{-20} m^2/W$ in the range between 490 nm and 1500 nm. For the type A waveguide, n_2 is more than 3 times lower than the value of the bulk material. And for the type B waveguide, n_2 is approximately 47 times lower. This way, we can conclude that the fs-laser writing process caused the reduction of the nonlinear refractive index of the material. Furthermore, the reduction was greater for waveguides fabricated with higher pulse energy. The reduction of the nonlinear refractive index in waveguides fabricated by fs-laser writing has been recently observed in the literature for different glassy materials. Blömer *et al.*[104] observed the reduction of the effective n_2 in waveguides fabricated in silica glass. Furthermore, the n_2 magnitude depended on the writing parameters. Waveguides fabricated with lower writing speed presented a larger reduction of n_2, being even 4 times lower than the value of the bulk material. Demetriou *et al.*[69] determined the n_2 of waveguides

fabricated in gallium lanthanum sulfide, a chalcogenide glass. They observed that the n_2 of the waveguides is 4 to 5 times lower than the value of the bulk material. *Royon et al*.[105] perfomed Third Harmonic Generation Microscopy in fs-laser irradiated silica glass and observed the reduction on the third-order susceptibility of the material when compared to the non-irradiated material. This way, we can conclude that the reduction of the nonlinear refractive index due to fs-laser irradiation is a common phenomenon in glassy materials. However, still very little is known about the structural modifications that can cause reduction of optical nonlinearities in fs-laser irradiated matter. To better understand this process, we realized Raman spectroscopy measurements in a type C waveguide, that was fabricated with pulses of $5\ \mu J$.

4.3 Raman spectroscopy measurements

4.3.1 Experimental Methods

Aiming to study the structural modifications created in Gorilla® Glass waveguides during the fs-laser writing process, we realized Raman Spectroscopy measurements[106] at the Center for Characterization of Mineral Species (CCEM) at the São Carlos Institute of Physics with Dr. Marcelo B. Andrade. The Raman spectra were recorded on a micro-Raman system (*LabRaman HR Evolution*) with a 532 nm laser that was focused in the sample by an objective lens (100x – 0.9 NA). The measurements were performed in a waveguide that was fabricated with pulses of 5 µJ, denominated type C waveguide. A simplified scheme of the Raman Spectroscopy measurements is shown in Fig. 4.7. This waveguide presents an elongated transversal profile, as seen in the inset of Fig. 4.7, that extends for approximately 30 µm inside the glass, due to the self-focusing phenomenon that occurs during the writing process. The center of the transversal profile is located at approximately 77 µm below the glass slide surface. To obtain the Raman spectra, the sample was positioned on an automated moving platform. Initially the laser beam was focused on the glass surface and then the sample was moved closer to the lens, so the laser could be focused deeper into the glass. This way, the focus position was swept from the glass surface (0 µm) to 120 µm of depth, and the Raman spectra were collected at every 2 µm.

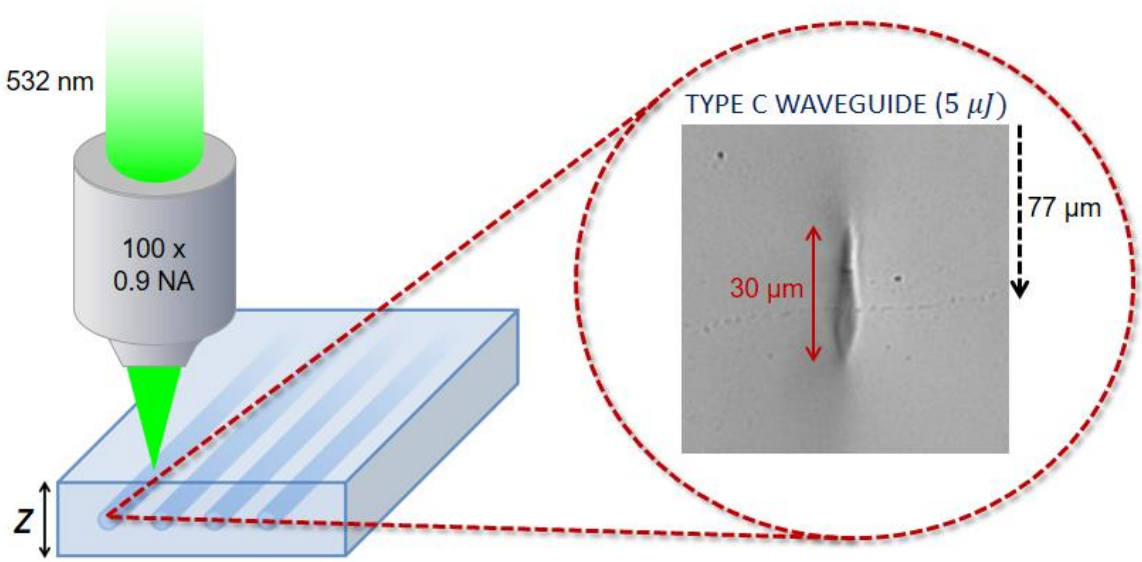

Figure 4.7 - Simplified scheme of the Raman Spectroscopy measurements. Inset: optical microscopy image of the transversal profile of the type C waveguide that has approximately 30 μm of height and is located at 77 μm below the glass surface.
Source: By the author

4.3.2 Results and Discussion

In Fig. 4.8 we present the Raman spectrum of Gorilla® Glass collected at 40 μm below the surface (black line), as well as the Raman spectrum of the irradiated material inside the type C waveguide at 76 μm below the surface (blue line). Both spectra present the typical shape for alkali aluminosilicate glasses.[107–109] Comparing the curves, we can notice a few visible differences. In this work, we focused our interest in two peaks of the low energy region, centered at $479\ cm^{-1}$ and $590\ cm^{-1}$, and in the high energy peak centered at $1078\ cm^{-1}$. These peaks are indicated by arrows in Fig. 4.8.

Raman spectra were collected at every 2 μm from the glass surface to 120 μm of depth, and passing through the irradiated region of the type C waveguide. They were post-processed and the baseline was extracted taking as reference the plateau region above $1400\ cm^{-1}$. After that, the Raman peaks were fitted by multiple Gaussian curves, and the regions of low $(400 - 600\ cm^{-1})$ and high $(900 - 1200\ cm^{-1})$ energy were adjusted separately after being normalized by their area.

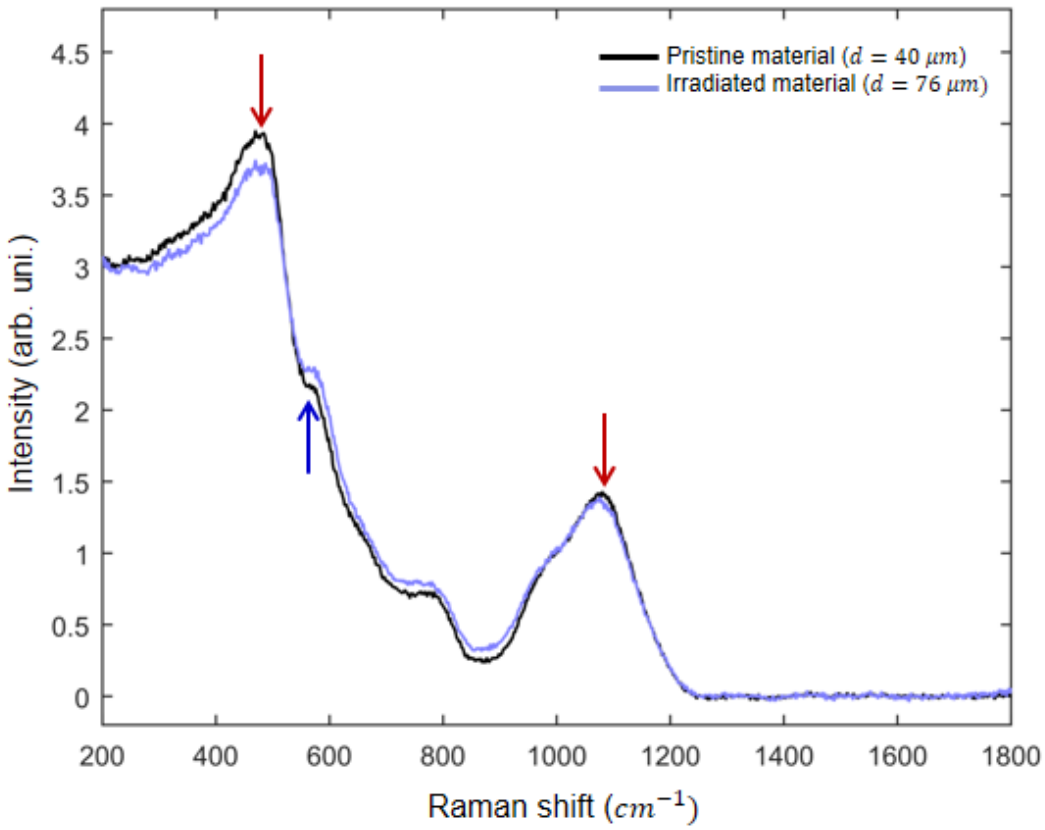

Figure 4.8 - Raman spectrum of pristine Gorilla® Glass collected from 40 µm below the surface (black line) and the spectrum of the type C waveguide collected from 76 µm below the surface (blue line). The arrows indicate the main peaks that presented modifications after the fs-laser writing process: $\mathbf{479}\ \boldsymbol{cm^{-1}}$, $\mathbf{590}\ \boldsymbol{cm^{-1}}$ and $\mathbf{1078}\ \boldsymbol{cm^{-1}}$.
Source: Adapted from HENRIQUE *et al.*[102]

Through the Gaussian fit we obtained the peaks intensity, width and position. In Fig. 4.9, we can observe how the low frequency peaks behave as function of the material depth. The intensity of the peak centered at $479\ cm^{-1}$ is decreased in the region centered at approximately 77 µm below the surface, which extends through more than 30 µm in depth. The size and position of this region correspond to the morphological features of the waveguide, as observed in the optical microscopy images (inset Fig. 4.7). This way, we can conclude that the observed spectral modifications are related to the fs-laser writing process. According to Fig. 4.9, there is also an intensity increase in the peak centered at $590\ cm^{-1}$, in the same region in which occurs the decrease in the peak centered at $479\ cm^{-1}$.

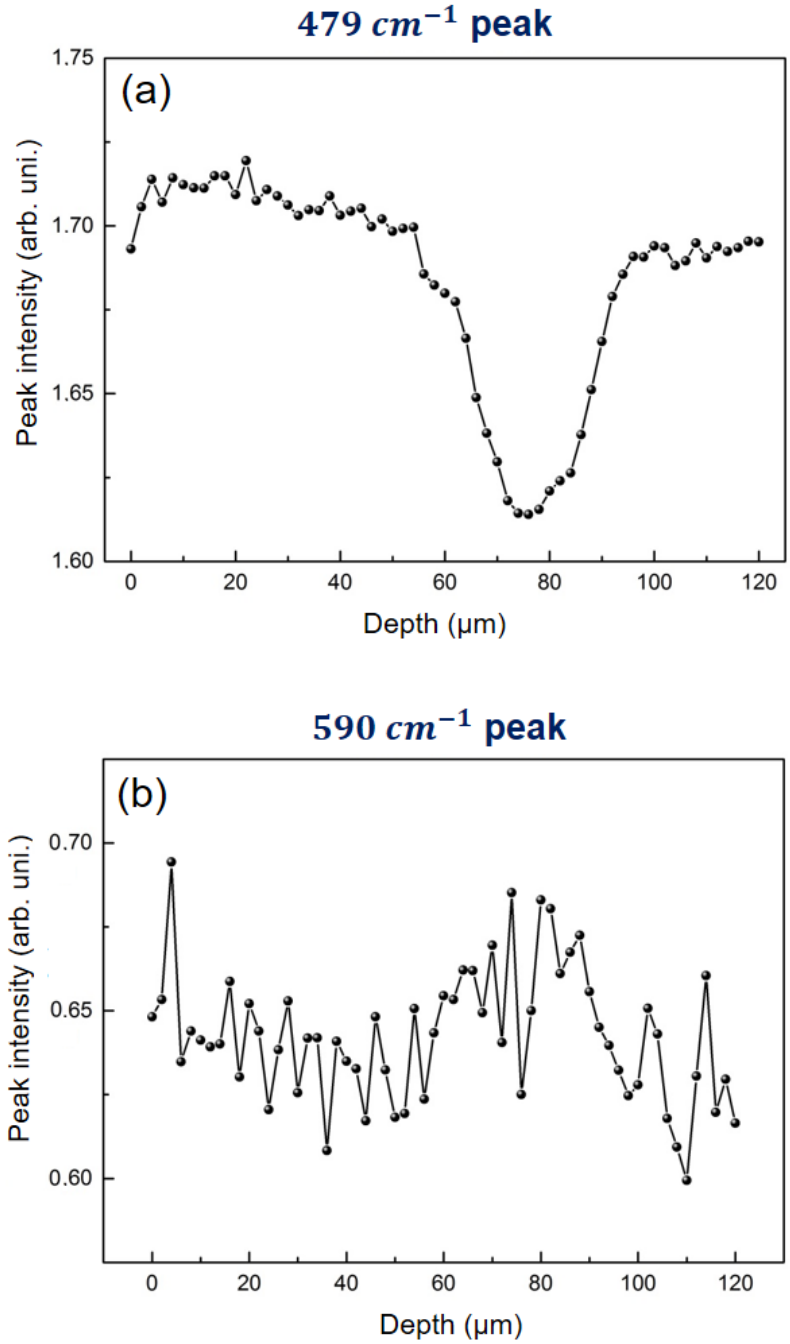

Figure 4.9 - Intensity of the peaks centered at (a) $\mathbf{479\ cm^{-1}}$ and (b) $\mathbf{590\ cm^{-1}}$ as function of the glass depth.
Source: (a) Adapted from HENRIQUE *et al.*;[102] (b) By the author

The fundamental structure of aluminosilicate glasses is constituted of TO_4 ($T = Si\ or\ Al$) tetrahedra,[106] known as network formers. They are represented in Fig. 4.10 (left). To build the glass matrix, the tetrahedral structures connect to each other through oxygen atoms. When an atom of oxygen connects two tetrahedra, it is classified as a bridging oxygen (BO). The oxygen atoms that do not connect

tetrahedra are classified as non-bridging oxygens (NBOs). A common way that the tetrahedra connect to form the glass matrix is in the form of ring-shaped structures. In Fig. 4.10 (right), we can observe a simplified representation of 3 and 4-membered ring structures. For the case of alkali-aluminosilicate glasses, the alkali ions, known as network modifiers, associate to the glass matrix through ionic bonds with the non-bridging oxygens.[110]

The bands centered at $479\ cm^{-1}$ and $590\ cm^{-1}$, known as D1 and D2 bands, are related to the 4 and 3-membered ring structures of TO_4 $(T = Si\ or\ Al)$, respectively.[109] Muniz *et al.*[111] performed the structural analysis of calcium-aluminosilicate glasses under high pressure. They observed that the densification process in silica-rich glasses leads to the creation of 3-membered ring structures, which corresponds to an increase in the D2 band. Bressel *et al.*[112] performed Raman Spectroscopy studies in germanate glasses that were irradiated by femtosecond laser pulses. The authors also observed an increase in the D2 band, as well as a decrease in the D1 band. These modifications were once again attributed to the densification of the material. This way, we can conclude that the results presented in Fig. 4.9, that point to the decrease of the D1 band and the increase of the D2 band in the irradiated material, are related to the densification process that takes places during the fs-laser writing process.

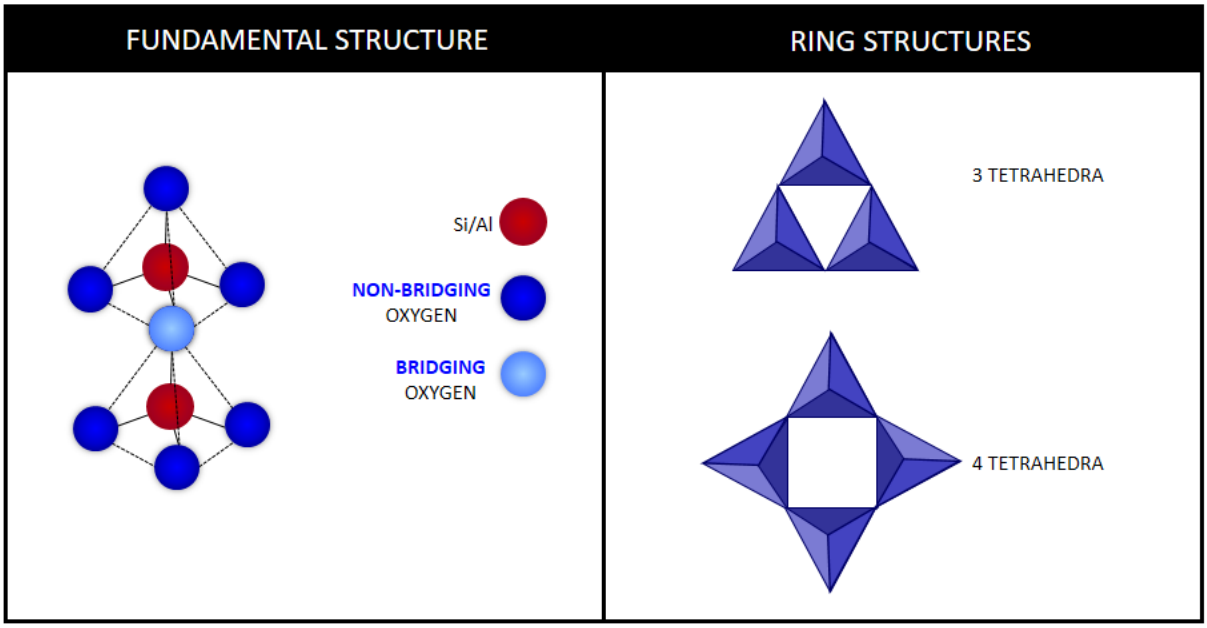

Figure 4.10 - Scheme of the structure of aluminosilicate glasses, with their fundamental structure (left) of silica or aluminum tetrahedra and common ring structures composed of 3 or 4 tetrahedra (right).
Source: By the author

In Fig. 4.11, we present the features of the high-frequency peak centered at $1078\ cm^{-1}$ as function of the glass depth. This band can be associated with the presence of non-bridging oxygens (NBOs) in the glass structure.[113–115] We can notice a gradual decrease in the peak intensity from the surface to the glass volume (Fig. 4.11-a). This is related to the ion exchange process that occurs mainly on the material surface and can extend through approximately 200 μm below. The decrease in this band is accentuated in the region around 75 μm of depth, where there is also a broadening effect to this band (Fig. 4.11-b). The decrease in the $1078\ cm^{-1}$ band indicates the reduction in the quantity of NBOs, i.e. the generation of non-bridging oxygen hole centers (NBOHCs), common structural defects generated by fs-laser irradiation.[116] The $1078\ cm^{-1}$ band broadening can be associated to an increased heterogeneity of the NBOs bonding angles. It is broadly known in the literature that NBOs are the main responsible for the optical nonlinearities in glasses,[117] as they are more polarizable than bridging oxygens (BOs). This way, our results indicate that the reduction in the quantity of NBOs, as well as a greater heterogeneity of their bonding angles, can be the responsible for the decrease of the nonlinear refractive index in the fs-laser written Gorilla® Glass waveguides.

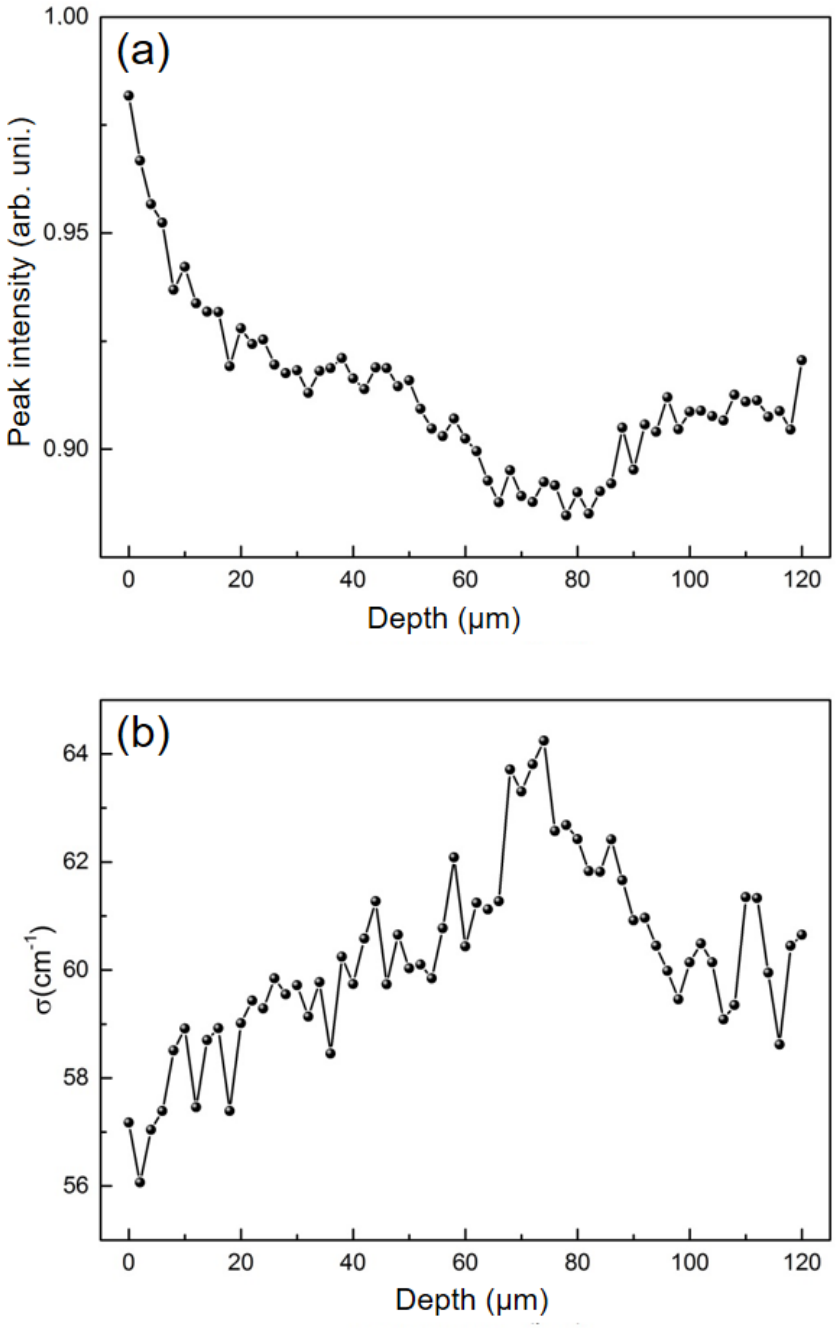

Figure 4.11 - (a) Intensity and (b) width of the peak centered at $\mathbf{1078}\ \boldsymbol{cm^{-1}}$ as function of the glass depth.
Source: (a) Adapted from HENRIQUE *et al*.;[102] (b) By the author

4.4 Partial conclusions

We performed the characterization of the nonlinear refractive index of fs-laser written Gorilla® Glass waveguides through the Dispersive-scan technique. Their nonlinear refractive index is lower than the one for the non-irradiated bulk material. For the type A waveguide, fabricated with pulses of 250 nJ, n_2 is 3 times lower, while

for the type B waveguide, fabricated with pulses of 500 nJ, n_2 is approximately 47 lower. Raman spectroscopy measurements in a type C waveguide, fabricated with pulses of 5 μJ, revealed the decrease and broadening of the high energy band related to non-bridging oxygens. This way, the interaction of fs-laser pulses with the glass material causes ionization and/or breaking of bonds that affects the quantity of NBOs as well as their bonding angles, ultimately leading to the reduction of the nonlinear refractive index in the irradiated region. This effect is stronger when the material is irradiated with higher energy pulses.

5 THIRD-ORDER NONLINEAR CHARACTERIZATION OF EAGLE XG® GLASS WAVEGUIDES

Eagle XG® Glass is an alkaline earth boro-aluminosilicate produced by Corning®. Its exceptionally smooth and flat surfaces, together with the possibility to be produced as really large and thin panels (down to 0.25 mm of thickness), makes Eagle XG® Glass an outstanding material for displays, covering the increasing demand for large TV screens, for example.[118] In 2019, Corning® had sold 25 billion square feet of Eagle XG® Glass, enough to cover 390 000 football fields. Furthermore, when launched in 2006, Eagle XG® was the first heavy-metal free display glass to be produced, paving the way for more environmentally friendly panels. In recent years, the impressive optical and mechanical features of Eagle XG® Glass has prompt its use in fs-laser direct writing for fabrication of high quality and low-loss waveguide circuits that can be applied to microfluidics, quantum photonics, sensors, etc.[119-120]

Advances in the industry of ultrashort lasers allowed the production of high-power lasers with high repetition rate, reaching the MHz range. This means that the fs-laser processing of transparent materials can be realized in different fabrication regimes, according to the excitation laser repetition rate, i.e. the repetitive and cumulative regimes.[11,121] In the repetitive fabrication regime, performed in kHz range, the time interval between two consecutive pulses is greater than the heat diffusion time, meaning that no heating accumulation takes place. This way, waveguide fabrication is performed through the generation of structural defects and can be realized with great resolution, since material modification stays localized at the focal spot. In the cumulative regime, performed in MHz range, heat accumulation takes place. Usually, heat diffusion expands the area modified by the fs-laser to regions around the focal spot.[122] In this Chapter, we present results related to the characterization of the nonlinear refractive index of fs-laser written Eagle XG® Glass waveguides fabricated in these two different regimes and explore how they can affect the material nonlinearities.

5.1 Fabrication

The waveguides studied here were fabricated by fs-laser direct writing in collaboration with Prof. Dr. Paulo Henrique Dias Ferreira (UFSCar) and Prof. Dr. Gustavo Foresto Brito de Almeida (UFU). Eagle XG® Glass slides were placed on an experimental apparatus as the one illustrated in Fig. 4.1. Straight waveguides were fabricated in two regimes, repetitive and cumulative, by using different laser sources. For fabrication in the repetitive regime, the beam of an amplified Ti:Sapphire laser (*Clark-MXR*: 150 fs, 775 nm, 1 kHz) was focused approximately 150 μm below the glass surface by an objective lens of 0.65 NA. Waveguides were fabricated with pulse energy of 250 nJ (type D waveguide) and 400 nJ (type E waveguide), and speed of 100 μm/s. In the cumulative regime, the beam of an extended cavity Ti:Sapphire oscillator (*Femtosource™ XL*), emitting 60 fs pulses centered at 800 nm with 5 MHz of repetition rate, was focused approximately 120 μm below the glass surface. The waveguides were fabricated with pulse energy of 40 nJ and speed of 1 mm/s (type F waveguides). It is important to note that, in both cases, fabrication was performed with pulse energy close to the material zero-damage threshold for each regime.

5.2 Dispersive-Scan measurements

5.2.1 Repetitive regime

Dispersive-Scan measurements were performed in the Eagle Glass waveguides with the same experimental methods described in Section 4.2.1. In Fig. 5.1 we can observe a D-scan curve obtained for a type D waveguide fabricated in the repetitive regime, using pulse energy of 250 nJ, 1 kHz of repetition rate and 100 μm/s of speed. The inset shows the guided mode image collected after the output objective, showing that it presents a Gaussian intensity profile. The input parameters used in the numerical model (black line) to fit the experimental data (red dots) were**:** $E = 7.7\,nJ$, $d = 6.0\,\mu m$, $\lambda_0 = 785.2\,nm$, $\Delta\lambda = 25.6\,nm$, $L = 14.40\,mm$, resulting in the nonlinear refractive index value of $n_2 = (0.08 \pm 0.02) \times 10^{-20}\ m^2/W$.

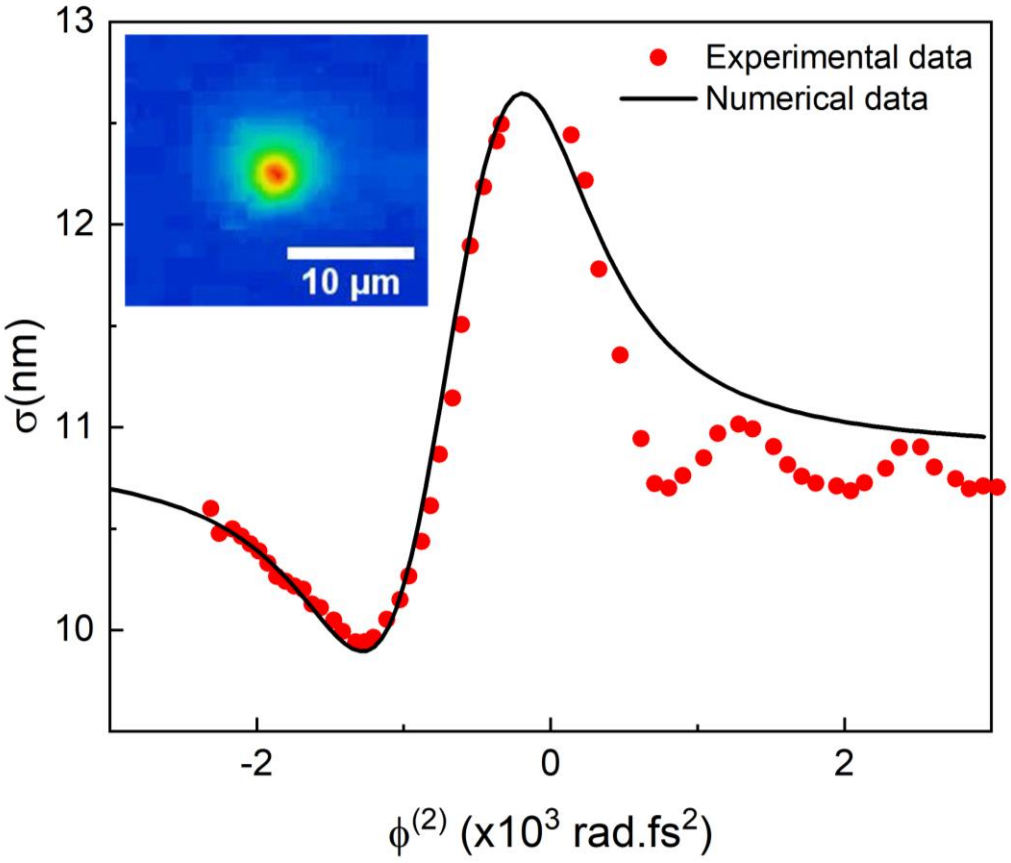

Figure 5.1 - D-scan measurement in type D Eagle Glass waveguide fabricated in the repetitive regime (250 nJ, 100 µm/s, 1 kHz). The parameters used in the numerical model were: *E = 7.7 nJ, d = 6.0 µm,* $\boldsymbol{\lambda_0}$ *=785.2 nm, Δλ = 25.6 nm, L=14.40 mm* and $\boldsymbol{n_2 = 0.08 \times 10^{-20}\ m^2/W}$. Inset: Image of the guided mode collected after the output objective lens.
Source: By the author

In Fig. 5.2 we can observe the D-scan measurement of a type E waveguide fabricated in the repetitive regime with higher pulse energy than the type D. The fabrication parameters were: 400 nJ, 1 kHz and 100 µm/s. In the inset, we can once again observe the intensity profile of the approximately Gaussian guided mode. The parameters used in the numerical model (black line) to adjust the experimental data (red dots) were: $E = 14.9\,nJ$, $d = 5.4\,\mu m$, $\lambda_0 = 785.2\,nm$, $\Delta\lambda = 26.8\,nm$, $L = 14.40\,mm$ e $n_2 = (0.025 \pm 0.007) \times 10^{-20}\ m^2/W$.

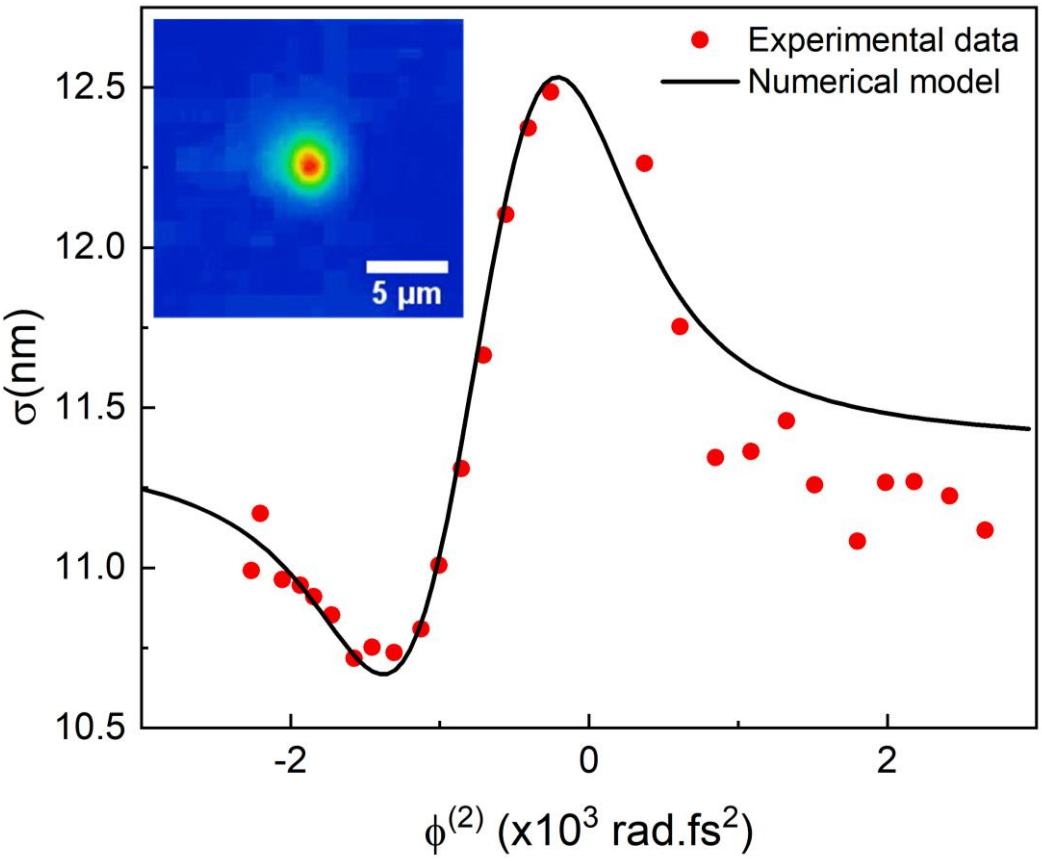

Figure 5.2 - D-scan measurement in a type E Eagle Glass waveguide fabricated in the repetitive regime (400 nJ, 100 µm/s, 1 kHz). The parameters used in the numerical model were: *E = 14.9 nJ, d = 5.4 µm,* λ_0 *=785.2 nm, Δλ = 26.8 nm, L=14.40 mm* and $\boldsymbol{n_2 = 0.025 \times 10^{-20}\, m^2/W}$. Inset: Image of the guided mode collected after the output objective lens.
Source: By the author

5.2.2 Cumulative regime

In Fig. 5.3 we can observe the Dispersive-Scan measurement in a type F Eagle Glass waveguide that was fabricated in the cumulative regime with the following parameters: 40 nJ, 5 MHz and 1 mm/s. The inset shows the guided mode image collected at the output of the waveguide. The input parameters used in the numerical model were: $E = 0.5\, nJ$, $d = 7.8\, \mu m$, $\lambda_0 = 785\, nm$, $\Delta\lambda = 25.10\, nm$, $L = 14.65\, mm$, resulting in an effective nonlinear refractive index of $n_2 = (2.9 \pm 0.9) \times 10^{-20} m^2/W$.

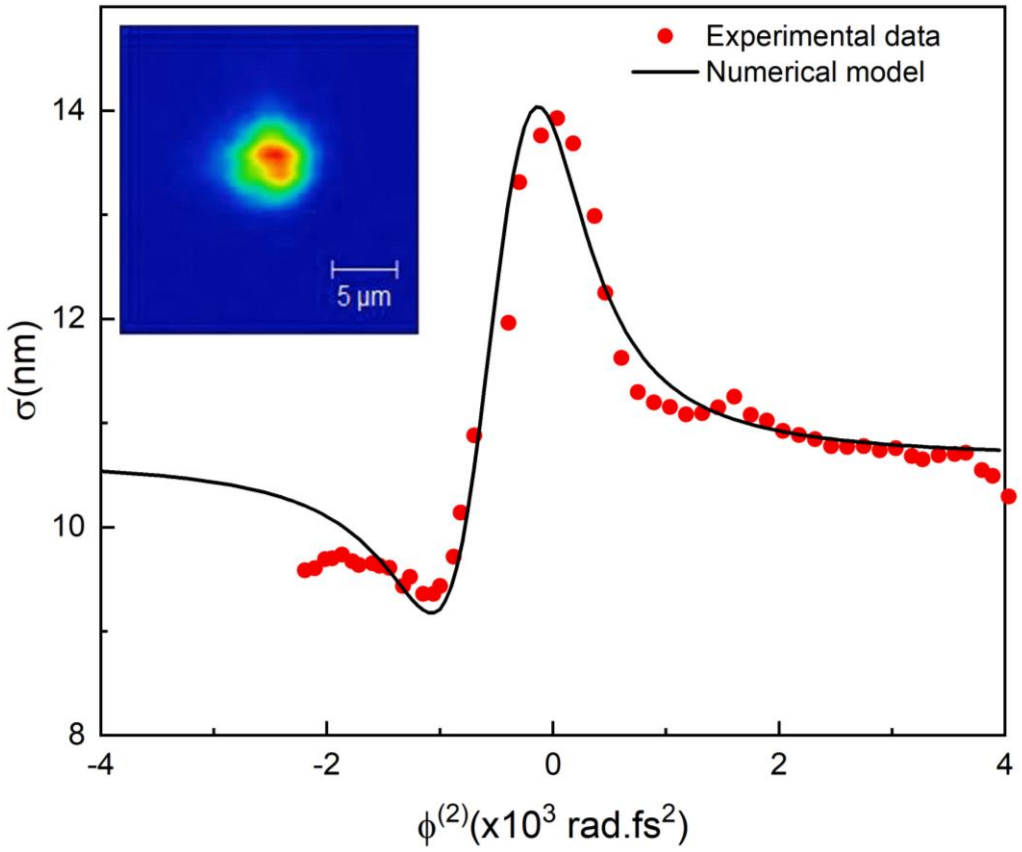

Figure 5.3 - D-scan measurement in a type F Eagle Glass waveguide fabricated in the cumulative regime (40 nJ, 1 mm/s, 5 MHz). The parameters used in the numerical model were: $\boldsymbol{E = 0.5\,nJ}$, $\boldsymbol{d = 7.8\,\mu m}$, $\boldsymbol{\lambda_0 = 785\,nm}$, $\boldsymbol{\Delta\lambda = 25.10\,nm}$, $\boldsymbol{L = 14.65\,mm}$ and $\boldsymbol{n_2 = 2.9 \times 10^{-20} m^2/W}$. Inset: Image of the guided mode collected after the output objective lens.
Source: By the author

5.3 Discussion

The nonlinear refractive index of bulk Eagle XG® Glass was characterized through the Z-scan technique[62] by Prof. Dr. Gustavo Foresto Brito de Almeida (UFU). Figure 5.4 presents a Z-scan measurement (red dots) in a 1 mm glass slide at 790 nm. The theoretical fitting (black line) results in a nonlinear refractive index of $(3.6 \pm 0.7) \times 10^{-20}\, m^2/W$. This value is in accordance to typical values for boro and aluminosilicates found in the literature.[123-124]

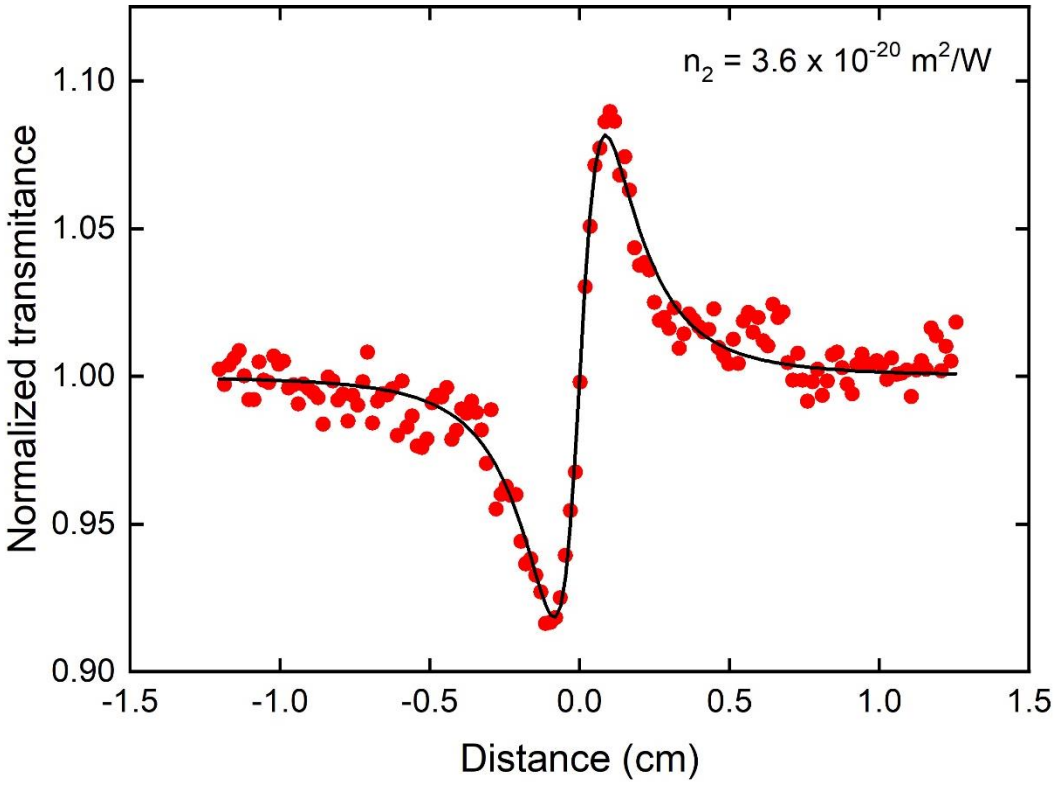

Figure 5.4 – Experimental (red dots) and theoretical (black line) curves of Z-scan measurement in bulk Eagle Glass performed at 790 nm.
Source: By the author

Comparing the n_2 values obtained for different fs-laser written waveguides and the value for the bulk material, we can conclude that there is a significant nonlinearity decrease in the case of the repetitive regime. For the type D Eagle Glass waveguides, fabricated with pulses of 250 nJ, the effective nonlinear refractive index is 45 times lower than the value for the bulk material. For the type E Eagle Glass waveguide, fabricated with higher pulse energy of 400 nJ, the effective nonlinear refractive index is reduced to less than 1% of the value for the pristine material. However, for waveguides fabricated in the cumulative regime, little to no difference is observed between the nonlinear refractive index value of the fs-laser written waveguide and the non-irradiated bulk material, especially if we consider the measurements error.

It is important to note that in both fabrication regimes, the pulse energy applied was always close to the zero-damage threshold.[125-126] This way, the big difference between the repetitive and cumulative fabrication regimes in the material nonlinearities could be explained by thermal effects, as well as the incubation effect[127–130] in fabrication with femtosecond laser pulses. This effect describes how

previous laser pulses influence the damage produced by the subsequent pulses. In most cases, the damage threshold decreases when the number of pulses per spot increases.[127,131]

The number of pulses per spot (N) in the fabricated waveguides can be calculated by the ratio between the total intensity of multiple pulses (I_{total}) at one spot and the intensity of a single pulse (I_{pulse}) centered at that spot. This ratio can be expressed as a Jacobi theta function ϑ_3 as follows[130]

$$N = \frac{I_{total/spot}}{I_{pulse/spot}} = \vartheta_3\left(0, e^{-2\left(\frac{v}{fw_0}\right)^2}\right), \tag{5.1}$$

where v is the writing speed, f is the laser repetition rate and w_0 is the focused beam waist. In the case of large superposition of pulses, achieved with low writing speed and high repetition rate, $\frac{v}{fw_0}$ is approximately zero, and the Jacobi theta function ϑ_3 can be simplified to

$$N = \sqrt{\frac{\pi}{2}}\left(\frac{fw_0}{v}\right). \tag{5.2}$$

The beam waist can be estimated by the Rayleigh Resolution Criterion[132] as follows

$$w_0 = 0.61\frac{\lambda}{NA}. \tag{5.3}$$

All of our waveguides were fabricated with a 40x objective lens of 0.65 NA, resulting in a beam waist of approximately 0.74 μm. This way, according to Eq. 5.2, the number of pulses per spot for the waveguides fabricated in the repetitive regime (types D and E), considering repetition rate of 1 kHz and speed of 100 μm/s, is around 9 pulses. On the other hand, for the waveguides fabricated in the cumulative regime (type F), with repetition rate of 5 MHz and speed of 1 mm/s, the number of pulses per spot is 4643.

The great difference between the number of pulses per spot, as well as the time interval between pulses, leads to very different fs-laser pulse interaction dynamics. According to the incubation effect, the accumulation of pulses in one spot

leads to the reduction of the fluence necessary to lead to macroscopic material modifications.[127] This happens because the first pulse to hit the matter creates point defects through multi-photon excitation. The defects introduce additional energy levels and excitation routes for the following pulses, lowering the fluence required for excitation.[127,133] The accumulation of point defects is what activates macroscopic damage. When high fluence is required in femtosecond laser microfabrication, as it is often the case in the repetitive regime, deep modifications in the glass matrix can be promoted, such as breakage of strong bonds and formation of O_2^- ions, rarefaction, formation of voids, and nanocracks.[134–137] When low fluence is used in fabrication with fs-laser pulses, soft material changes happen, and they are usually related to the glass electronic configuration and defect-assisted densification.[84,116] As heat accumulation takes place, when the time interval between pulses is shorter than the matrix thermal relaxation time, fs-laser fabrication benefits from thermal annealing and decreased thermal cycling, which creates smooth and crack-free structures.[43]

Si-O bond breaking and generation of non-bridging oxygen hole centers (NBOHCs) are the most easily induced defects in silica glass upon fs-laser irradiation.[116] In the same way, NBOHCs concentration can be easily reduced upon low power 488 nm continuous laser exposure[138] and thermal annealing.[139] They are poorly stable defects that can be completely erased in fs-laser exposed silica glass after thermal treatment at 300° C.[139] As discussed in Chapter 4, the presence of non-bridging oxygens (NBOs) is primarily responsible for third-order nonlinearities in silica-derived glasses.[117,140]

The dynamics of creation and annealing of NBOHCs can help us understand our Dispersive-Scan results, presented in Section 5.2. What we propose is that, when Eagle XG® Glass waveguides are fabricated in the repetitive regime, with just a few pulses per spot and high laser pulse fluence, Si-O bonds are broken and NBOHCs are created. Several other structural defects can also be induced, like the formation of voids and rarefaction, leaving the fabricated waveguide with a high concentration of NBOHCs and stress-related structural defects. This way, the great reduction of non-bridging oxygen bonds would explain the reduction of the nonlinear refractive index, just like in fs-laser irradiated Gorilla® Glass.[102] In the case of Eagle XG® Glass waveguides fabricated in the cumulative regime, the great number of pulses per spot, 2-3 orders of magnitude greater than in the repetitive regime, reduces the fluence required for fabrication, reducing the number of defects

generated. Furthermore, heat accumulation due to high repetition rate can work as a fs-laser induced thermal annealing treatment, giving enough energy to recombine Si-O bonds, reducing the number of NBOHCs defects and leaving only stronger fs-laser induced structural modifications, like silica-tetrahedra rings reconfiguration.[139] The reduction of NBOHCs defects restores the material nonlinear polarizability and could explain the effective nonlinear refractive index value in waveguides fabricated in the cumulative regime, which is very close to the value for the pristine bulk material.

5.4 Partial conclusions

We performed the third-order nonlinear characterization of fs-laser written Eagle XG® Glass waveguides through the Dispersive-Scan technique. The waveguides were fabricated in two different regimes according to the excitation laser repetition rate: repetitive (1 kHz) and cumulative (5 MHz). For the waveguides fabricated in the repetitive regime, we observed the reduction of the nonlinear refractive index when compared to the value for the bulk material. This reduction also depends on the writing beam pulse energy. For waveguides fabricated with pulses of 250 nJ, the measured n_2 is 45 times lower than the value for the bulk material, while for waveguides fabricated with pulses of 400 nJ, n_2 is 144 times lower. For waveguides fabricated in the cumulative regime, with pulses of 40 nJ, the nonlinear refractive index suffers little to no reduction when compared to the bulk value. The big difference between the measured nonlinearities in the two different regimes is potentially related to the generation and annealing of NBOHCs defects. In the repetitive regime, waveguides were fabricated with high fluence, greatly decreasing the number of NBOs, thus reducing the nonlinear polarizability. In the cumulative regime, lower fluence was used during fabrication and heat accumulation took place. NBOHCs defects can be easily erased through heat, restoring then the nonlinear optical properties.

6 CONCLUSIONS AND PERSPECTIVES

We realized the implementation of the Dispersive-Scan technique for the first time in our lab with the goal of studying the third-order nonlinear optical properties of femtosecond-laser written microstructures. We built the experimental apparatus and automated the data acquisition, developed the data post-processing method and the numerical simulations to adjust the experimental curves. Our numerical method, implemented in *LabView* with the add-on *Lab2 – A virtual femtosecond-laser lab* takes into account self-phase modulation, dispersion, guiding losses and nonlinear absorption. The D-scan technique was then used to characterize fs-laser written waveguides in Corning® Gorilla® and Eagle XG® Glass.

In Gorilla® Glass the nonlinear refractive index of two types of waveguides was characterized: type A, fabricated with pulses of 250 nJ, and type B, fabricated with pulses of 500 nJ. These waveguides were fabricated with a Ti:Sapphire laser at 780 nm, operating at 1 kHz, and a writing speed of 200 μm/s. Type A waveguides presented a nonlinear refractive index of $(0.9 \pm 0.3) \times 10^{-20}\, m^2/W$ at 785 nm, which is 3 times lower than the value for the bulk material: $(3.3 \pm 0.6) \times 10^{-20} m^2/W$. Type B waveguides, fabricated with higher pulse energy, presented n_2 of $(0.07 \pm 0{,}02) \times 10^{-20}\, m^2/W$, which is approximately 47 times lower than the value for the bulk material. This way, we can conclude that the fs-laser inscription process was responsible for reducing the nonlinear refractive index of the irradiated material, and this reduction depends on the writing parameters. Raman Spectroscopy measurements were performed in a type C waveguide, fabricated with even higher pulse energy of $5\,\mu J$, and a reduction in the amount of non-bridging oxygen atoms (NBOs) present in the irradiated matrix was observed. As NBOs are primarily responsible for the third-order nonlinearities in silica-derived glasses, the breakage of NBOs bonds and creation of non-bridging oxygen hole centers (NBOHCs) defects can explain the reduction of the nonlinear refractive index observed in our D-scan measurements.

In Eagle XG® Glass the nonlinear refractive index of waveguides fabricated in the repetitive and cumulative regimes was characterized, so to study the effect of the writing beam repetition rate in the material nonlinearities. In the repetitive regime, waveguides were fabricated with repetition rate of 1 kHz and writing speed of 100 μm/s. Type D waveguides were fabricated with pulse energy of 250 nJ and type E

with 400 nJ. D-scan characterization showed once again that the nonlinear refractive index of the fs-laser written waveguides was reduced when compared to the value of the bulk material, $(3.6 \pm 0.7) \times 10^{-20}\, m^2/W$. For the type D waveguide, n_2 is $(0.08 \pm 0.02) \times 10^{-20}\, m^2/W$, 45 times lower than the bulk value. For the type E waveguide, n_2 is $(0.025 \pm 0.007) \times 10^{-20}\, m^2/W$, 144 times lower. As in the Gorilla® Glass waveguides, the reduction in the nonlinear refractive index is greater when higher pulse energy is used in the writing process. In the cumulative regime, type F waveguides were fabricated with repetition rate of 5 MHz, writing speed of 1 mm/s and pulse energy of 40 nJ. Their nonlinear refractive index was determined to be $(2.9 \pm 0.9) \times 10^{-20} m^2/W$, meaning that little to no reduction in nonlinearities was observed in comparison to the bulk non-irradiated material. This phenomenon can be explained by a conjunction of two effects: the incubation effect and heat accumulation. The incubation effect leads to the decrease of the fluence required for fabrication when a greater number of pulses per spot is applied. In our case, 9 pulses per spot were used in the repetitive regime, while 4643 were used in the cumulative regime. This resulted in the decrease of writing fluence from 14 (type D) and 23 J/cm^2 (type E) in the repetitive regime to 2.3 J/cm^2 (type F) in the cumulative regime. Lower fluence means that less defects are generated in the glass matrix. As heat accumulation took place during fabrication of the type F waveguides, the NBOHCs defects generated could have been easily erased, and the Si-O non-bridging bonds restored, maintaining the optical nonlinearities of the irradiated material. Structural studies, like Raman Spectroscopy, can be performed in the future to better understand this process.

Our results shine light on the physical phenomena that take place during fs-laser writing, a process that is still yet to be completely understood, and how these phenomena affect the optical nonlinearities of the irradiated material. The clear dependence of the written waveguides n_2 with the writing parameters is something that needs to be taken into account when directing the technological application of these structures. For instance, waveguides with low third-order nonlinearities are interesting in passive telecomm applications, where nonlinear phenomena can be detrimental to the guided signal quality. On the other hand, for applications in active photonic devices, for frequency generation or optical switching, for example, it is important that the material nonlinearities are preserved.

In the future, we plan to apply the Dispersive-Scan technique to characterize the absorptive nonlinearities of polymer waveguides containing interesting doping materials, like high-nonlinear chromophores, nanoparticles, etc. In the past two years, we advanced a lot on the fabrication of these waveguides, first by two-photon polymerization in our setup at the Photonics Group (IFSC-USP) and then by the UV-assisted Soft Nanoimprint Lithography (UV-SNIL) technique at the Optical Nanomaterial Group in ETH Zurich, where the student realized an 11-month internship under the supervision of Prof. Dr. Rachel Grange. More information about the internship abroad can be found in Annex B.

REFERENCES

1 KELLER, U. Recent developments in compact ultrafast lasers. **Nature**, v. 424, n. 6950, p. 831–838, 2003.

2 REID, D. T. Ultrafast Lasers - technology and applications. **Journal of Microscopy**, v. 211, n. 1, p. 101, 2003.

3 KELLER, U. Ultrafast solid-state laser oscillators: a success story for the last 20 years with no end in sight. **Applied Physics B**, v. 100, n. 1, p. 15–28, 2010.

4 ZEWAIL, A. H. Laser femtochemistry. **Science**, v. 242, n. 4886, p. 1645–1653, 1988.

5 BOYD, R. W. **Nonlinear optics**. Boca Raton: CRC Press, 2008.

6 PHILLIPS, K. C. *et al*. Ultrafast laser processing of materials: a review. **Advances in Optics and Photonics**, v. 7, n. 4, p. 684, 2015.

7 SUGIOKA, K. Progress in ultrafast laser processing and future prospects. **Nanophotonics**, v. 6, n. 2, p. 393–413, 2017.

8 STRICKLAND, D.; MOUROU, G. Compression of amplified chirped optical pulses. **Optics Communications**, v. 56, n. 3, p. 219–221, 1985.

9 ZALEVSKY, Z.; ABDULHALIM, I. Fabrication aspects of integrated devices. *In*: ZALEVSKY, Z.; ABDULHALIM, I. (ed.). **Integrated nanophotonic devices**. Amsterdam: Elsevier, 2010. p. 99–111.

10 CHICHKOV, B. N. *et al*. Femtosecond, picosecond and nanosecond laser ablation of solids. **Applied Physics A**: materials science and processing, v. 63, n. 2, p. 109–115, 1996.

11 GATTASS, R. R.; MAZUR, E. Femtosecond laser micromachining in transparent materials. **Nature Photonics**, v. 2, n. 4, p. 219–225, 2008.

12 MARUO, S.; NAKAMURA, O.; KAWATA, S. Three-dimensional microfabrication with two-photon-absorbed photopolymerization. **Optics Letters**, v. 22, n. 2, p. 132–134, 1997.

13 KAWATA, S. *et al*. Finer features for functional microdevices. **Nature**, v. 412, n. 6848, p. 697–698, 2001.

14 YETISEN, A. K. *et al*. Art on the nanoscale and beyond. **Advanced Materials**, v. 28, n. 9, p. 1724–1742, 2016.

15 MAO, M. *et al*. The emerging frontiers and applications of high-resolution 3D printing. **Micromachines**, v. 8, n. 4, p. 113, 2017.

16 ZHOU, X.; HOU, Y.; LIN, J. A review on the processing accuracy of two-photon polymerization. **AIP Advances**, v. 5, n. 3, p. 030701, 2015.

17 EL-TAMER, A.; HINZE, U.; CHICHKOV, B. N. Two-photon polymerization in optics, microfluidics, and biomedicine. *In*: SUGIOKA, K. (ed.). **Handbook of laser micro- and nano-engineering**. Cham: Springer International Publishing, 2020. p. 1–44.

18 LIN, Y.; XU, J. Microstructures fabricated by two-photon polymerization and their remote manipulation techniques: toward 3D printing of micromachines. **Advanced Optical Materials**, v. 6, n. 8, p. 1701359, 2018.

19 NGUYEN, A. K.; NARAYAN, R. J. Two-photon polymerization for biological applications. **Materials Today**, v. 20, n. 6, p. 314–322, 2017.

20 WEI, H.; KRISHNASWAMY, S. Direct laser writing polymer micro-resonators for refractive index sensors. **IEEE Photonics Technology Letters**, v. 28, n. 24, p. 2819–2822, 2016.

21 SCHUMANN, M. *et al*. Hybrid 2D–3D optical devices for integrated optics by direct laser writing. **Light**: science & applications, v. 3, n. 6, p. e175–e175, 2014.

22 WU, Z.-L. *et al*. Polymer-based device fabrication and applications using direct laser writing technology. **Polymers**, v. 11, n. 3, p. 553, 2019.

23 GISSIBL, T. *et al*. Two-photon direct laser writing of ultracompact multi-lens objectives. **Nature Photonics**, v. 10, n. 8, p. 554–560, 2016.

24 JIMENEZ GORDILLO, O. A. *et al*. Plug-and-play fiber to waveguide connector. **Optics Express**, v. 27, n. 15, p. 20305, 2019.

25 DEUBEL, M. *et al*. Direct laser writing of three-dimensional photonic-crystal templates for telecommunications. **Nature Materials**, v. 3, n. 7, p. 444–447, 2004.

26 GROSSMANN, T. *et al*. Direct laser writing for active and passive high-Q polymer microdisks on silicon. **Optics Express**, v. 19, n. 12, p. 11451, 2011.

27 TOMAZIO, N. B.; DE BONI, L.; MENDONCA, C. R. Low threshold Rhodamine-doped whispering gallery mode microlasers fabricated by direct laser writing. **Scientific Reports**, v. 7, n. 1, p. 8559, 2017.

28 HENRIQUE, F. R.; MENDONCA, C. R. Local excitation and collection in polymeric fluorescent microstructures. **Optical Materials**, v. 54, p. 176–180, 2016. DOI: 10.1016/j.optmat.2016.02.020.

29 PENG, Y. *et al*. 3D photoluminescent nanostructures containing quantum dots fabricated by two-photon polymerization: influence of quantum dots on the spatial resolution of laser writing. **Advanced Materials Technologies**, v. 4, n. 2, p. 1800522, 2019.

30 USHIBA, S. *et al*. 3D microfabrication of single-wall carbon nanotube/polymer composites by two-photon polymerization lithography. **Carbon**, v. 59, p. 283–288, 2013. DOI: 10.1016/j.carbon.2013.03.020

31 TOMAZIO, N. B. *et al*. Mode cleaning in graphene oxide-doped polymeric

whispering gallery mode microresonators. **Journal of Materials Chemistry C**, v. 8, n. 28, p. 9707–9713, 2020.

32 SUN, H. B. *et al*. Two-photon photopolymerization and diagnosis of three-dimensional microstructures containing fluorescent dyes. **Applied Physics Letters**, v. 79, n. 10, p. 1411–1413, 2001.

33 MENDONCA, C. R. *et al*. Reversible birefringence in microstructures fabricated by two-photon absorption polymerization. **Journal of Applied Physics**, v. 102, n. 1, p. 013109, 2007.

34 RICHARDSON, K.; KROL, D.; HIRAO, K. Glasses for photonic applications. **International Journal of Applied Glass Science**, v. 1, n. 1, p. 74–86, 2010.

35 WOOD, R. M. Glasses for photonics. **Optics and Lasers in Engineering**, v. 33, n. 5, p. 383–384, 2000.

36 SHELBY, J. E.; KOHLI, J. T. Rare- earth aluminosilicate glasses. **Journal of the American Ceramic Society**, v. 73, n. 1, p. 39–42, 1990.

37 GY, R. Ion exchange for glass strengthening. **Materials Science and Engineering B**, v. 149, n. 2, p. 159–165, 2008.

38 EHRT, D. Photoluminescence in glasses and glass ceramics. **IOP Conference Series**: materials science and engineering, v. 2, n. 1, p. 012001, 2009.

39 DE OLIVEIRA, M. *et al*. Structure-property relations in fluorophosphate glasses: An integrated spectroscopic strategy. **Journal of Physical Chemistry C**, v. 121, n. 5, p. 2968–2986, 2017.

40 CHEN, Q. *et al*. Faraday rotation influence factors in tellurite-based glass and fibers. **Applied Physics A**: materials science and processing, v. 120, n. 3, p. 1001–1010, 2015.

41 ASOBE, M. Nonlinear optical properties of chalcogenide glass fibers and their application to all-optical switching. **Optical Fiber Technology**, v. 3, n. 2, p. 142–148, 1997.

42 HARBOLD, J. M. *et al*. Highly nonlinear As–S–Se glasses for all-optical switching. **Optics Letters**, v. 27, n. 2, p. 119, 2002.

43 OSELLAME, R.; CERULLO, G.; RAMPONI, R. **Femtosecond laser micromachining**. Berlin, Heidelberg: Springer, 2012. (Topics in applied physics, v. 123)

44 LAPOINTE, J. *et al*. Making smart phones smarter with photonics. **Optics Express**, v. 22, n. 13, p. 15473, 2014.

45 CHEN, W.-J. *et al*. Broadband directional couplers fabricated in bulk glass with high repetition rate femtosecond laser pulses. **Optics Express**, v. 16, n. 15, p. 11470, 2008.

46 CORRIELLI, G. *et al*. Symmetric polarization-insensitive directional couplers fabricated by femtosecond laser writing. **Optics Express**, v. 26, n. 12, p. 15101, 2018.

47 CRESPI, A. *et al*. Three-dimensional Mach-Zehnder interferometer in a microfluidic chip for spatially-resolved label-free detection. **Lab on a Chip**, v. 10, n. 9, p. 1167–1173, 2010.

48 AMORIM, V. A. *et al*. Mach-Zehnder interferometer-based evanescent refractometer inscribed at the surface of eagle 2000 by femtosecond laser writing. **IEEE Sensors Journal**, v. 21, n. 2, p. 1603–1608, 2021.

49 EATON, S. M. *et al*. Spectral loss characterization of femtosecond laser written waveguides in glass with application to demultiplexing of 1300 and 1550 nm wavelengths. **Journal of Lightwave Technology**, v. 27, n. 9, p. 1079–1085, 2009.

50 HAQUE, M.; HERMAN, P. R. Chemical-assisted femtosecond laser writing of optical resonator arrays. **Laser and Photonics Reviews**, v. 9, n. 6, p. 656–665, 2015.

51 LEVY, S.; KLEBANOV, M.; ZADOK, A. High-Q ring resonators directly written in As_2S_3 chalcogenide glass films. **Photonics Research**, v. 3, n. 3, p. 63, 2015.

52 MARSHALL, G. D. *et al*. Point-by-point written fiber-Bragg gratings and their application in complex grating designs. **Optics Express**, v. 18, n. 19, p. 19844, 2010.

53 DONKO, A. *et al*. Point-by-point femtosecond laser micro-processing of independent core-specific fiber Bragg gratings in a multi-core fiber. **Optics Express**, v. 26, n. 2, p. 2039, 2018.

54 TACCHEO, S. *et al*. Er:Yb-doped waveguide laser fabricated by femtosecond laser pulses. **Optics Letters**, v. 29, n. 22, p. 2626, 2004.

55 AMS, M. *et al*. Ultrafast laser written active devices. **Laser and Photonics Reviews**, v. 3, n. 6, p. 535–544, 2009.

56 MEANY, T. *et al*. Laser written circuits for quantum photonics. **Laser and Photonics Reviews**, v. 9, n. 4, p. 363–384, 2015.

57 SUGIOKA, K. *et al*. Femtosecond laser 3D micromachining: a powerful tool for the fabrication of microfluidic, optofluidic, and electrofluidic devices based on glass. **Lab on a Chip**, v. 14, n. 18, p. 3447–3458, 2014.

58 LAPOINTE, J. *et al*. Toward the integration of optical sensors in smartphone screens using femtosecond laser writing. **Optics Letters**, v. 40, n. 23, p. 5654, 2015.

59 LIFANTE, G. **Integrated photonics:** fundamentals. Chichester, UK: John Wiley & Sons, 2003.

60 CHAN, J. W. *et al*. Structural changes in fused silica after exposure to focused femtosecond laser pulses. **Optics Letters**, v. 26, n. 21, p. 1726, 2001.

61 LAPOINTE, J. *et al*. Control and enhancement of photo-induced refractive index modifications in fused silica. **OSA Continuum**, v. 3, n. 10, p. 2851, 2020.

62 SHEIK-BAHAE, M. *et al*. Sensitive measurement of optical nonlinearities using a single beam. **IEEE Journal of Quantum Electronics**, v. 26, n. 4, p. 760–769, 1990.

63 MINOSHIMA, K.; TAIJI, M.; KOBAYASHI, T. Femtosecond time-resolved interferometry for the determination of complex nonlinear susceptibility. **Optics Letters**, v. 16, n. 21, p. 1683, 1991.

64 LAGASSE, M. J. *et al*. Femtosecond all-optical switching in AlGaAs waveguides using a time division interferometer. **Applied Physics Letters**, v. 54, n. 21, p. 2068–2070, 1989.

65 MONERIE, M.; DURTESTE, Y. Direct interferometric measurement of nonlinear refractive index of optical fibres by crossphase modulation. **Electronics Letters**, v. 23, n. 18, p. 961–963, 1987.

66 LOURADOUR, F. *et al*. Dispersive-scan measurement of the fast component of the third-order nonlinearity of bulk materials and waveguides. **Optics Letters**, v. 24, n. 19, p. 1361, 1999.

67 LOPEZ-LAGO, E. *et al*. Characterization of the fast component of the complex third-order nonlinearity and time response of bulk materials and waveguides. **Journal of the Optical Society of America B**, v. 18, n. 8, p. 1166, 2001.

68 FONSECA, E. J. S.; GOUVEIA, E. A.; HICKMANN, J. M. Time analogue of the z-scan technique suitable to waveguides. **European Physical Journal D**, v. 17, n. 1, p. 75–78, 2001.

69 DEMETRIOU, G. *et al*. Nonlinear refractive index of ultrafast laser inscribed waveguides in gallium lanthanum sulphide. **Applied Optics**, v. 56, n. 19, p. 5407, 2017.

70 DU, Q. *et al*. Chip-scale broadband spectroscopic chemical sensing using an integrated supercontinuum source in a chalcogenide glass waveguide. **Photonics Research**, v. 6, n. 6, p. 506, 2018.

71 GAETA, A. L.; LIPSON, M.; KIPPENBERG, T. J. Photonic-chip-based frequency combs. **Nature Photonics**, v. 13, n. 3, p. 158–169, 2019.

72 MAIMAN, T. H. Stimulated optical radiation in Ruby. **Nature**, v. 187, n. 4736, p. 493–494, 1960.

73 FRANKEN, P. A. *et al*. Generation of optical harmonics. **Physical Review Letters**, v. 7, n. 4, p. 118–119, 1961.

74 KERR, J. LIV. A new relation between electricity and light: dielectrified media birefringent (Second paper). **The London, Edinburgh, and Dublin Philosophical Magazine and Journal of Science**, v. 50, n. 333, p. 446–458, 1875.

75 KERR, J. XL. A new relation between electricity and light: dielectrified media

birefringent. **The London, Edinburgh, and Dublin Philosophical Magazine and Journal of Science**, v. 50, n. 332, p. 337–348, 1875.

76 GÖPPERT- MAYER, M. Über elementarakte mit zwei quantensprüngen. **Annalen der Physik**, v. 401, n. 3, p. 273–294, 1931.

77 KAISER, W.; GARRETT, C. G. B. Two-photon excitation in CaF2: Eu2+. **Physical Review Letters**, v. 7, n. 6, p. 229–231, 1961.

78 SALEH, B. E. A.; TEICH, M. C. **Fundamentals of photonics**. New York: John Wiley & Sons, 1991. (Wiley series in pure and applied optics, v. 39)

79 SCHMIDT, B. *et al.* **LAB2-A virtual femtosecond laser lab**. 2005. Available from: http://www.lab2.de. Accessible at: 6 Apr. 2021.

80 TREBINO, R. **Frequency-resolved optical gating**: the measurement of ultrashort laser pulses. Boston: Springer, 2000.

81 SWAMP OPTICS. **Pulse compression tutorial**. Available from: http://www.swampoptics.com/assets/tutorial-pulse-compressor-2015.pdf. Accessible at: 6 Apr. 2021.

82 WEINER, A. M. Ultrafast optical pulse shaping: a tutorial review. **Optics Communications**, v. 284, n. 15, p. 3669-3692, 2011.

83 AGRAWAL, G. P. **Nonlinear fiber optics**. San Diego: Academic Press, 2019.

84 TAN, C. Z. Determination of refractive index of silica glass for infrared wavelengths by IR spectroscopy. **Journal of Non-Crystalline Solids**, v. 223, n. 1–2, p. 158–163, 1998.

85 MILAM, D. Review and assessment of measured values of the nonlinear refractive-index coefficient of fused silica. **Applied Optics**, v. 37, n. 3, p. 546, 1998.

86 LI, H. *et al*. Optical absorption in graphene integrated on silicon waveguides. **Applied Physics Letters**, v. 101, n. 11, p. 111110, 10 set. 2012.

87 SANTOS, S. N. C. *et al*. Fabrication of waveguides by fs-laser micromachining in Dy3+/Eu3+ doped barium borate glass with broad emission in the visible spectrum. **Optics Communications**, v. 427, p. 33–36, 2018.

88 MIURA, H. *et al*. High thermal stability 40 GHz electro-optic polymer modulators. **Optics Express**, v. 25, n. 23, p. 28643, 2017.

89 JIANG, L. *et al*. A photochromic dye doped polymeric Mach-Zehnder interferometer for UV light detection. **Journal of Materials Chemistry C**, v. 7, n. 21, p. 6257–6265, 2019.

90 FOROUTAN, S. *et al*. All-optical switching in metal nanoparticles plasmonic waveguide using EIT phenomenon. **Optik**, v. 132, p. 291–298, 2017. DOI: 10.1016/j.ijleo.2016.12.051.

91 ALMEIDA, J. M. P. **Nanoparticles in oxide and chalcogenide glasses: optical nonlinearities and waveguide fabrication by femtosecond laser pulses**. 2015. Tese (Doutorado em Desenvolvimento, Caracterização e Aplicação de Materiais) - Escola de Engenharia de São Carlos, Universidade de São Paulo, São Carlos. 2015.

92 MAYERHÖFER, T. G.; POPP, J. Beyond Beer's law: revisiting the Lorentz-Lorenz equation. **ChemPhysChem**, v. 21, n. 12, p. 1218–1223, 2020.

93 SMITH, M.; ROLAND, D. Understanding differences between OTDR and cut-back attenuation measurements in multimode graded index fiber. *In*: ANNUAL MEETING IEEE LASERS AND ELECTRO-OPTICS SOCIETY, 9., 1996, Boston. **Proceedings** [...]. Boston: IEEE, 1996.

94 REGENER, R.; SOHLER, W. Loss in low-finesse Ti:LiNbO3 optical waveguide resonators. **Applied Physics B**: photophysics and laser chemistry, v. 36, n. 3, p. 143–147, 1985.

95 SERNA, S.; DUBREUIL, N. Bi-directional top-hat D-Scan: single beam accurate characterization of nonlinear waveguides. **Optics Letters**, v. 42, n. 16, p. 3072, 2017.

96 RUZIN, S.; AARON, H. **1P vs 2P fluorescence imaging**. Available from: http://microscopy.berkeley.edu/courses/tlm/2P/index.html. Accessible at: 9 May 2021.

97 HUANG, Y. L. *et al*. Femtosecond Z-scan measurement of GaN. **Applied Physics Letters**, v. 75, n. 22, p. 3524–3526, 1999.

98 XU, X. *et al*. Observation of third-order nonlinearities in graphene oxide film at telecommunication wavelengths. **Scientific Reports**, v. 7, n. 1, p. 9646, 2017.

99 BALL, P. Concrete mixing for gorillas. **Nature Materials**, v. 14, n. 5, p. 472–472, 2015.

100 CORNING. **Corning ® Gorilla ® Glass**: more than a decade of innovation in device glasses for consumer electronics. Available from: https://www.corning.com/microsites/csm/gorillaglass/CGG_Timeline/Gorilla_Glass_Timeline.pdf. Accessible at: 9 May 2021.

101 ALMEIDA, G. F. B. **Femtosecond laser writing of nonlinear waveguides in Gorilla glass and L-threonine organic crystals**. 2018. Tese (Doutorado em Física Básica) - Instituto de Física de São Carlos, Universidade de São Paulo, São Carlos. 2018.

102 HENRIQUE, F. R. *et al*. Nonlinear characterization of fs-laser written Gorilla Glass waveguides. **Optical Materials Express**, v. 8, n. 8, p. 2222, 2018.

103 ALMEIDA, G. F. B. *et al*. Third-order optical nonlinearities in bulk and fs-laser inscribed waveguides in strengthened alkali aluminosilcate glass. **Laser Physics**, v. 28, n. 1, p. 015401, 2018.

104 BLÖMER, D. *et al*. Nonlinear refractive index of fs-laser-written waveguides in fused silica. **Optics Express**, v. 14, n. 6, p. 2151, 2006.

105 ROYON, A. *et al*. Evolution of the linear and nonlinear optical properties of femtosecond laser exposed fused silica. **Journal of the Optical Society of America B**, v. 26, n. 11, p. 2077, 2009.

106 YADAV, A. K.; SINGH, P. A review of the structures of oxide glasses by Raman spectroscopy. **RSC Advances**, v. 5, n. 83, p. 67583–67609, 2015.

107 BRAWER, S. A.; WHITE, W. B. Raman spectroscopic investigation of the structure of silicate glasses (II). Soda-alkaline earth-alumina ternary and quaternary glasses. **Journal of Non-Crystalline Solids**, v. 23, n. 2, p. 261–278, 1977.

108 MCKEOWN, D. A.; GALEENER, F. L.; BROWN, G. E. Raman studies of Al coordination in silica-rich sodium aluminosilicate glasses and some related minerals. **Journal of Non-Crystalline Solids**, v. 68, n. 2–3, p. 361–378, 1984.

109 TERAKADO, N. *et al*. CO2 laser-induced weakening in chemically strengthened glass: improvement in processability and its visualization by Raman mapping. **Ceramics International**, v. 44, n. 3, p. 2843–2846, 2018.

110 NEWLANDS, K. C.; MACPHEE, D. E. The reactivity of aluminosilicate glasses in cements–effects of Ca content on dissolution characteristics and surface precipitation. **Advances in Applied Ceramics**, v. 116, n. 4, p. 216–224, 2017.

111 MUNIZ, R. F. *et al*. In situ structural analysis of calcium aluminosilicate glasses under high pressure. **Journal of Physics**: condensed matter, v. 28, n. 31, p. 315402, 10 ago. 2016.

112 BRESSEL, L. *et al*. Observation of O_2 inside voids formed in GeO_2 glass by tightly-focused fs-laser pulses. **Optical Materials Express**, v. 1, n. 6, p. 1150, 2011.

113 MATSON, D. W.; SHARMA, S. K.; PHILPOTTS, J. A. The structure of high-silica alkali-silicate glasses. a Raman spectroscopic investigation. **Journal of Non-Crystalline Solids**, v. 58, n. 2–3, p. 323–352, 1983.

114 HIGBY, P. L.; SHELBY, J. E.; CONDRATE, R. A. Raman spectra of alkali galliosilicate glasses of the series 20R2O-xGa2O3-(80-x)SiO2. **Journal of Non-Crystalline Solids**, v. 84, n. 1–3, p. 93–99, 1986.

115 WINDISCH, C.; RISEN, W. M. Comparative Raman study of mixed alkali and similar ion-exchanged glasses. **Journal of Non-Crystalline Solids**, v. 44, n. 2–3, p. 345–364, 1981.

116 MISHCHIK, K. *et al*. Ultrafast laser induced electronic and structural modifications in bulk fused silica. **Journal of Applied Physics**, v. 114, n. 13, p. 133502, 2013.

117 BOLING, N. L.; GLASS, A. J.; OWYOUNG, A. Empirical relationships for predicting nonlinear refractive index changes in optical solids. **IEEE Journal of Quantum Electronics**, v. 14, n. 8, p. 601–608, 1978.

118 CORNING. **Corning® EAGLE XG® Glass substrates**: innovation timeline. Available from:

https://www.corning.com/media/worldwide/cdt/documents/Corning_EXG_Timeline_2020.pdf. Accessible at: 9 May 2021.

119 CRESPI, A.; OSELLAME, R.; BRAGHERI, F. Femtosecond-laser-written optofluidics in alumino-borosilicate glass. **Optical Materials**: X, v. 4, n. 10, p. 100042, 2019.

120 CRESPI, A. *et al*. Integrated multimode interferometers with arbitrary designs for photonic boson sampling. **Nature Photonics**, v. 7, n. 7, p. 545–549, 2013.

121 ALMEIDA, J. M. P. *et al*. Nonlinear optical properties and femtosecond laser micromachining of special glasses. **Journal of the Brazilian Chemical Society**, v. 26, n. 12, p. 2418–2429, 2015.

122 EATON, S. M. *et al*. Heat accumulation effects in femtosecond laser-written waveguides with variable repetition rate. **Optics Express**, v. 13, n. 12, p. 4708, 2005.

123 GREHN, M. et al. Nonlinear absorption and refraction of binary and ternary alkaline and alkaline earth silicate glasses. **Optical Materials Express**, v. 3, n. 12, p. 2132, 2013.

124 WEBER, M. J.; MILAM, D.; SMITH, W. L. Nonlinear refractive index of glasses and crystals. **Optical Engineering**, v. 17, n. 5, p. 175463, 1978.

125 LIU, J. M. Simple technique for measurements of pulsed Gaussian-beam spot sizes. **Optics Letters**, v. 7, n. 5, p. 196, 1982.

126 MARTIN, S. *et al*. Spot-size dependence of the ablation threshold in dielectrics for femtosecond laser pulses. **Applied Physics A**: materials science and processing, v. 77, n. 7, p. 883–884, 2003.

127 ASHKENASI, D. *et al*. Surface damage threshold and structuring of dielectrics using femtosecond laser pulses: the role of incubation. **Applied Surface Science**, v. 150, n. 1, p. 101–106, 1999.

128 DI NISO, F. *et al*. Role of heat accumulation on the incubation effect in multi-shot laser ablation of stainless steel at high repetition rates. **Optics Express**, v. 22, n. 10, p. 12200, 2014.

129 MACHADO, L. M. *et al*. D-Scan measurement of ablation threshold incubation effects for ultrashort laser pulses. **Optics Express**, v. 20, n. 4, p. 4114, 2012.

130 ALMEIDA, G. F. B. et al. Incubation effect during laser micromachining of GaN films with femtosecond pulses. **Journal of Materials Science**: materials in electronics, v. 30, n. 18, p. 16821–16826, 2019.

131 OOSTERBEEK, R. N. *et al*. Effects of dopant type and concentration on the femtosecond laser ablation threshold and incubation behaviour of silicon. **Applied Physics A**, v. 122, n. 4, p. 449, 2016.

132 MURPHY, D. B.; DAVIDSON, M. W. **Fundamentals of light microscopy and**

electronic imaging. 2nd ed. Hoboken: John Wiley & Sons, 2012.

133 SUN, Z.; LENZNER, M.; RUDOLPH, W. Generic incubation law for laser damage and ablation thresholds. **Journal of Applied Physics**, v. 117, n. 7, p. 073102, 2015.

134 GLEZER, E. N.; MAZUR, E. Ultrafast-laser driven micro-explosions in transparent materials. **Applied Physics Letters**, v. 71, n. 7, p. 882–884, 1997.

135 MERMILLOD-BLONDIN, A. *et al*. Dynamics of femtosecond laser induced voidlike structures in fused silica. **Applied Physics Letters**, v. 94, n. 4, p. 041911, 2009.

136 TAYLOR, R.; HNATOVSKY, C.; SIMOVA, E. Applications of femtosecond laser induced self-organized planar nanocracks inside fused silica glass. **Laser and Photonics Reviews**, v. 2, n. 1–2, p. 26–46, 2008.

137 TAN, D. *et al*. Femtosecond laser induced phenomena in transparent solid materials: fundamentals and applications. **Progress in Materials Science**, v. 76, p. 154–228, 2016.

138 CHAN, J. W. *et al*. Modification of the fused silica glass network associated with waveguide fabrication using femtosecond laser pulses. **Applied Physics A**: materials science and processing, v. 76, n. 3, p. 367–372, 2003.

139 WITCHER, J. J. *et al*. Thermal annealing of femtosecond laser written structures in silica glass. **Optical Materials Express**, v. 3, n. 4, p. 502, 2013.

140 NASU, H. *et al*. Non-resonant-type third-order optical non-linearity of alkali silicate and alkali aluminosilicate glasses - contribution of individual chemical species in the glasses to χ(3). **Journal of Non-Crystalline Solids**, v. 182, n. 3, p. 321–327, 1995.

ANNEX A – List of publications and conference presentations

- **Part of this thesis was published in the following paper:**

***Henrique, Franciele R.**; Brito De Almeida, Gustavo F.; Martins, Renato J.; Rosa, Ramon G. T.; Siqueira, Jonathas P.; De Andrade, Marcelo B.; Mendonça, Cleber R.* Nonlinear characterization of fs-laser written Gorilla Glass waveguides. **Optical Materials Express**, v. 8, p. 2222, 2018.

- **Complementary publications:**

Tomazio, Nathália B.; Paula, Kelly T.; ***Henrique, Franciele R.**; Andrade, Marcelo B.; Roselló-Mechó, Xavier; Delgado-Pinar, Martina; Andrés, Miguel V.; Mendonca, Cleber R.* Mode cleaning in graphene oxide-doped polymeric whispering gallery mode microresonators. **Journal of Materials Chemistry C**, v. 8, p. 9707-9713, 2020.

***Henrique, Franciele R.**; Tomazio, Nathália B.; Rosa, Ramon G. T.; De Souza, Adélcio M.; D'almeida, Camila P.; Sciuti, Lucas F.; Garcia, Marlon R.; De Boni, Leonardo.* Light at first sight: A program of activities to teach Optics using colors. **Revista Brasileira De Ensino De Física** (Online), v. 41, p. e20180223, 2019.

Avila, Oriana I.; Almeida, Juliana M. P.; ***Henrique, Franciele R.**; Fonseca, Ruben D.; Almeida, Gustavo F. B.; Balogh, Débora T.; Mendonça, Cleber R.* Femtosecond-laser direct writing for spatially localized synthesis of PPV. **Journal of Materials Chemistry C**, v. 5, p. 3579-3584, 2017.

***Henrique, Franciele R.**; Mendonca, Cleber R. .* Local excitation and collection in polymeric fluorescent microstructures. **Optical Materials** (Amsterdam. Print), v. 54, p. 176-180, 2016.

- **Selected presentations in international conferences:**

***Henrique, Franciele R.**; Almeida, Gustavo F. B.; Martins, Renato J.; Rosa, Ramon G. T.; Siqueira, Jonathas P.; De Andrade, Marcelo B.; Mendonca, Cleber R.* Dispersive-scan characterization of the nonlinear refractive index of fs-laser written Gorilla Glass
Waveguides. At **1st Photonics Online Meetup**, 2020. (online poster)

Mendonça, Cleber R.; ***Henrique, Franciele**; Almeida, Gustavo; Martins, Renato; Rosa, Ramon; Siqueira, Jonathas; De Andrade, Marcelo.* Third-order nonlinear optical characterization of fs-laser micromachined waveguides in Gorilla Glass. At **SPIE Photonics West**, 2019, San Francisco, California, USA. (oral presentation)

***Henrique, Franciele R.**; Almeida, Gustavo F. B.; Martins, Renato J.; Rosa, Ramon G. T.; Siqueira, Jonathas P.; De Andrade, Marcelo B.; Mendonca, Cleber R.* Nonlinear Features of Femtosecond Laser Written Waveguides in Gorilla® Glass. At **2018 Advanced Photonics Congress** (The Optical Society), 2018, Zürich, Switzerland. (poster)

***Henrique, Franciele R.**; Almeida, Gustavo F. B.; Siqueira, Jonathas P.; Martins, Renato J.; Mendonca, Cleber R.* Nonlinear Optical Characterization of Gorilla® Glass Waveguides. At **Frontiers in Optics / Laser Science 2017** (The Optical Society), 2017, Washington, D.C.; USA. (poster)

***Henrique, Franciele R.**; Almeida, Gustavo F. B.; Mendonca, Cleber R.* Dispersive-scan nonlinear characterization of Gorilla® Glass waveguides. At **10th ICNP - International Conference on Nanophotonics, 2017**, Recife, PE, Brazil. (poster)

ANNEX B – Research internship abroad at ETH Zurich, Switzerland

2019-2020

(11 months) Project title: Electro-optic devices based on polymeric microstructures

Supervisor: Prof. Dr. Rachel Grange

Funded by: The São Paulo Research Foundation (FAPESP) and the Optical Nanomaterial Group (ETH Zurich)

Electro-optic (EO) modulators are key devices for photonic applications, because they can be used to encode signals in optics communications, for frequency generation, Q-switch in laser cavities, etc. With the advent of integrated photonics, EO devices based on waveguides have gained attention. Due to their ease of processing in the micro and nanoscale, polymers are interesting platforms for the fabrication of EO devices based on waveguides. Furthermore, high nonlinear molecules can be easily incorporated into the polymeric matrix, allowing for tailoring the device's EO properties. This way, in this project, we proposed the design, fabrication, and characterization of EO devices based on polymeric microstructures doped with the EO chromophore Disperse Red 13 (DR13). We also proposed the merging of these structures' EO properties with the high-quality guiding properties of fs-laser written waveguides in special glasses, thus producing hybrid polymer-glass devices.

First, we worked on the characterization of fs-laser written waveguides in Eagle® Glass that were fabricated in the Photonics Group (IFSC-USP). We were able to observe Fabry-Perot resonances in the cavity formed between the input and output facets of the waveguides. These resonances were used to determine the refractive index and the guiding losses of the waveguides. Since these waveguides were fabricated close to the surface of the glass, the resonances were also used to test the waveguide's ability to sense refractive index changes on the surface of the glass slide.

We also worked on the fabrication of polymeric waveguides containing the EO chromophore Disperse Red 13 (DR13) by two-photon polymerization. This was initially started in our homemade setup at the Photonics Group (IFSC-USP) and continued at the ETH Zurich facilities with a commercial equipment from *Nanoscrib*e.

Due to the challenges to fabricate long waveguides with the direct laser writing technique, we changed our approach and were able to fabricate polymeric waveguides on the centimeter scale with the UV-assisted soft nanoimprint lithography technique. In this approach, first a silicon master mold was fabricated by direct laser writing followed by dry-etching. From the silicon master mold, countless PDMS negative molds could be fabricated. The polymer waveguides were then fabricated by pressing the PDMS negative mold on top of a polymer film that was spin-coated on a glass substrate. UV irradiation was used to cure the polymer, so that the PDMS mold could be removed, leaving only the polymer waveguides on the substrate. This way, we were able to fabricate polymer waveguide circuits containing Mach-Zender interferometers and microresonators. Further advances are still necessary to improve the fabrication of these devices and also to characterize their EO properties.

At last, we worked on the fabrication and characterization of flat polymeric devices containing DR13, like diffraction gratings and arrays of holes. The devices were also fabricated by the UV-assisted soft nanoimprint technique. Their transmission spectra were characterize to evaluate the resonances of the fabricated structures. We also built an experiment to study the all-optical switching properties of DR13 and its effect on the resonances of the fabricated structures.